SEPTEMBER 1965
VOLUME XXVI
NUMBER 3

RCA REVIEW

PRINTED IN U.S.A.

RCA REVIEW, published quarterly in March, June, September, and December by RCA Laboratories, Radio Corporation of America, Princeton, New Jersey 08540. Entered as second class matter July 3, 1950 under the Act of March 3, 1879. Second-class postage paid at Princeton, New Jersey, and at additional mailing offices. Subscription price in the United States and Canada: one year $2.00, two years $3.50, three years $4.50; in other countries, one year $2.40, two years $4.30, three years $5.70. Single copies up to five years old $1.00. For copies more than five years old, contact Walter J. Johnson, Inc., 111 Fifth Ave., New York, N. Y. 10003.

RCA REVIEW

a technical journal

Published quarterly by
RCA LABORATORIES
in cooperation with all subsidiaries and divisions of
RADIO CORPORATION OF AMERICA

VOLUME XXVI SEPTEMBER 1965 NUMBER 3

CONTENTS

RCA REVIEW is regularly abstracted and indexed by *Abstracts of Photographic Science and Engineering Literature, Applied Science and Technology Index, Bulletin Signalétique des Télécommunications, Chemical Abstracts, Electronic and Radio Engineer, Mathematical Reviews,* and *Science Abstracts* (I.E.E.-Brit.).

RCA REVIEW

PUSH-PULL SATURATED CORE TUNNEL DIODE INVERTERS*

BY

R. FERYSZKA AND P. GARDNER

RCA Electronic Components and Devices
Somerville, N. J.

Summary—*Previous work on tunnel diode inverters for use with direct energy conversion sources such as thermionic generators indicated that the push–pull saturated square-hysteresis-loop (Marzolf) tunnel-diode inverter held the most promise for achieving high efficiency and power output with good power-to-weight ratio.*

A theory of the operation of this type of inverter has been developed. This theory predicts the performance of the inverter for varying input voltage and load from the I-V *characteristics of the tunnel diodes and transformer parameters, and shows that the diode figure of merit previously believed to be the limiting efficiency of such inverters can be exceeded by suitable design of the inverter.*

Second-order effects such as nonperfect squareness of the core-material hysteresis loop are also discussed, and their effect on inverter performance indicated.

Performance parameters of this type of inverter with outputs to 220 watts are presented, and unique operation features are discussed. Design and fabrication techniques are also briefly discussed.

INTRODUCTION

TUNNEL-DIODE inverter circuits and their application to low-voltage power sources have been explored by H. F. Storm and D. P. Shattuck,[1] F. G. Gevert, S. Wang, and R. U. Broze,[2] J. M.

* The work presented in this paper was sponsored by the United States Air Force, Air Force Aero Propulsion Laboratory, Aerospace Power Division, Wright Patterson Air Force Base, and was directed by H. Briggs, Captain USAF, project officer.

[1] H. F. Storm and D. P. Shattuck, "Tunnel Diode D-C Power Converter," *Trans. A.I.E.E.*, Vol. 80, p. 347, July 1961.

[2] F. G. Gevert, S. Wang, and R. U. Broze, "Heat to A.C. Conversion Using Thermoelectric Generators and Tunnel Diodes," *Solid-State Electronics*, Vol. 3, p. 100, Sept. 1961.

ings are in the same direction and the currents flow in opposite directions, no magnetizing occurs.

Assuming the current in loop I starts increasing at time t, with the core still unsaturated, a voltage equilibrium exists;

$$V_b - e_{T_1} - e_x = 0. \tag{2}$$

When the current reaches the value $i = I_v + I_m$, the core is saturated, and $e_x = N(d\phi/dt) \times 10^{-8} = 0$, since no further change in flux is possible. Since e_x is now zero, the tunnel-diode voltage must increase rapidly until the peak point is reached and the diode switches to the forward voltage. Since the core is still saturated, e_{T_1} and i drop rapidly until $i_1 = I_v + I_m$. At that point the core begins to unsaturate and a voltage e_x appears across the primary. The equilibrium now becomes

$$V_b + e_x - e_{T_1} = 0. \tag{3}$$

The current continues to decrease slowly until the valley point is reached. At this point e_x is again zero, and the diode switches to the low-voltage state.

It has been assumed that during a half cycle, e_x is constant. If Equations (2) and (3) are to hold, then e_{T_1} and e_{T_2} must also be constant. These assumptions are only valid when I_m is small compared to I_p. In practice, e_{T_2} varies over a wide range for small changes in current, leading to distorted waveshapes.

The region where the diode's operating point changes slowly between I_v and $I_v + I_m$ is defined as the "dwell" region. The switching cycle described above is illustrated in Figure 2.

In a push–pull circuit, both diodes operate simultaneously, i.e., when the first diode is in a low-voltage state (at I_v) with i_1 increasing, the second diode is at a high-voltage state (at $I_v + I_m$) with i_2 decreasing.

The time relationships for i_1, i_2, ϕ_1, ϕ_2, and I are shown in Figure 3. The currents, i_1 and i_2, are shifted by $T/2$ (Figure 3a) where T is the period of oscillation. The total current supplied by the power supply is constant and equal to $I_m + 2I_v$ (Figure 3b). The fluxes ϕ_1 and ϕ_2 are in phase with their appropriate magnetizing currents i_1 and i_2 (Figure 3c).

Although the fluxes are out of phase by $T/2$, the induced voltages, e_x, in both primary halves are in phase, since $d\phi/dt$ is positive for the first loop and negative for the second loop (Figure 3d).

It should be noted that this analysis is valid for only one specific

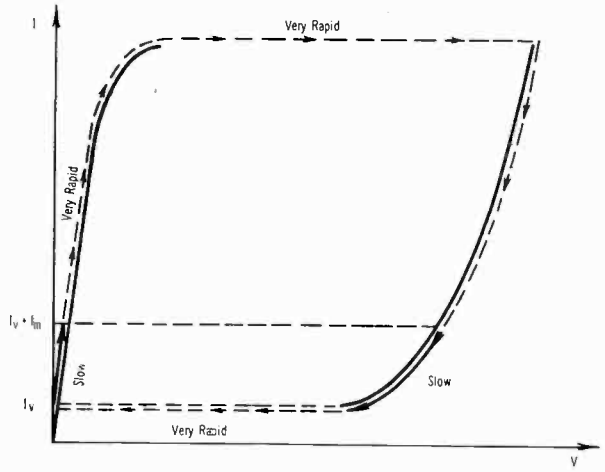

Fig. 2—Tunnel-diode characteristic showing switching path and dwell regions for unloaded condition.

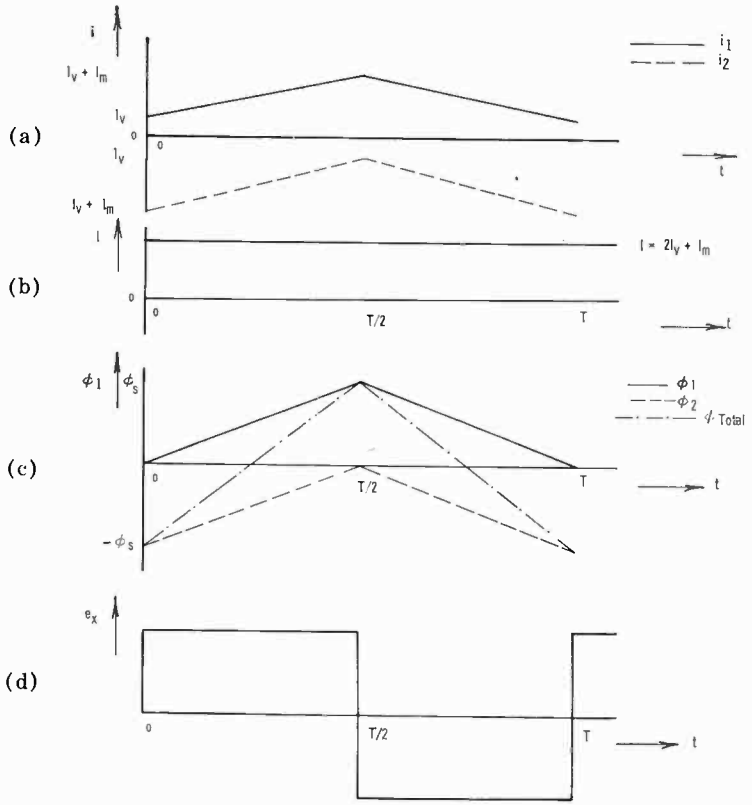

Fig. 3—Time relations for i_1, i_2, I, ϕ_1, ϕ_2, ϕ_{total}, and e_x under no-load conditions.

Thus, during a cycle, the d-c current I supplied by the power supply is $i_1 + i_2$.

$$I = nI_L + 2I_v + I_m. \tag{4}$$

Thus, for a given load, the current drawn by the inverter is constant.

It can be seen from Figure 6 that the maximum load current obtainable while still maintaining core saturation is

$$nI_{L(\max)} = I_p - I_v - I_m, \tag{5}$$

and the current drawn from the power supply is

$$\begin{aligned} I_{\max} &= I_p - I_v - I_m + 2I_v + I_m \\ &= I_p + I_v. \end{aligned} \tag{6}$$

Again, this analysis holds only for a particular bias voltage.

Having described the basic mode of operation of the inverter under no-load and loaded conditions, a more general analysis of the operation of this type of inverter can now be carried out.

Analysis of Push–Pull Saturated Core Inverter Operation

General Case with Inverter Loaded

a. Bias Voltage

It has been assumed that the bias voltage is such that the dwell and equilibria conditions previously described hold. However, in practice the input voltage will vary, and thus it is important to consider the effect of varying bias voltage.

During half a cycle, the following equilibria must hold

$$\begin{aligned} &\text{1st diode:} && V_b - e_{T_1} - e_x = 0, \\ &\text{2nd diode:} && V_b - e_{T_2} + e_x = 0. \end{aligned}$$

We make the assumption that I_m is small and that e_x is constant. Therefore,

$$V_b = \frac{1}{2}(e_{T_2} + e_{T_1}). \tag{7}$$

It can be seen from Equation (7) that for a given input voltage, V_b,

dwell points must be established to satisfy the equation, and that there is a minimum bias voltage for operation. As $e_{T_1(\min)} \cong 0$ and $e_{T_2(\min)} = V_v$, the minimum input voltage possible is $V_{v/2}$.

However, the minimum dwell points are, for the loaded inverter,

$$\text{1st diode:} \quad nI_L + I_v \rightarrow nI_L + I_v + I_m, \tag{8}$$

$$\text{2nd diode:} \quad I_v + I_m \rightarrow I_v, \tag{9}$$

and

$$I_{IN} = nI_L + 2I_v + I_m. \tag{10}$$

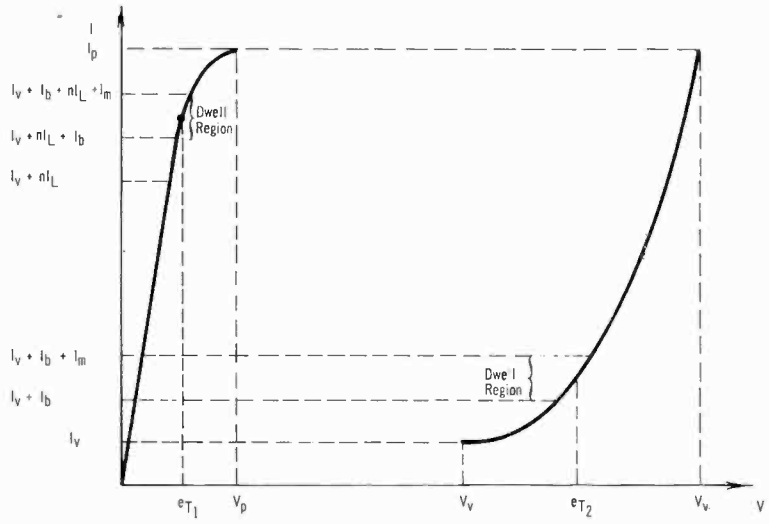

Fig. 7—Tunnel-diode characteristic showing dwell region currents and voltages for loaded condition.

This condition, where minimum current is drawn for a given load, is defined as "threshold" operation, and will be satisfied only for a particular input voltage, V_b. As the diode voltages e_{T_1} and e_{T_2} increase with increasing current, this value of V_b for threshold will also be the minimum input voltage at which the inverter will operate under given conditions of load. Also, the value of V_b for threshold operation will be greater at full load than at zero load.

Thus, in the general case, the dwell points for half a cycle will be, as shown in Figure 7,

$$\text{1st diode:} \quad nI_L + I_v + I_b \rightarrow nI_L + I_v + I_b + I_m,$$

$$\text{2nd diode:} \quad I_v + I_b + I_m \rightarrow I_v + I_b. \tag{11}$$

where I_b is some additional d-c current depending on the bias voltage, V_b. These dwell points are reversed in the second half cycle.

In order to compute the required input voltage, V_b, an expression for the I-V characteristic of the diodes is required. In general,

$$V_b = \frac{1}{2I_m}\left[\int_{I_v+I_b}^{I_v+I_b+I_m} e_2(i_2)\,di + \int_{I_v+I_b+nI_L}^{I_v+I_b+nI_L+I_m} e_1(i_1)\,di\right]. \tag{12}$$

To determine the voltages e_1 and e_2, $i_1 = f_1(e_1)$ and $i_2 = f_2(e_2)$ are required. For the tunneling region of a tunnel diode, Karlovsky[8] derived the expression

$$I = A'''(e_1 + e_2 - g_V)^2. \tag{13}$$

As e_1 is only required from 0 to V_p, Equation (13) suggests that a simple square function may be used.

The forward region of the tunnel diode is essentially the normal diode injection region (for good I_p/I_v ratio diodes, because the excess current component of I_v is then small), and thus follows the normal exponential function. Again, as e_2 is only required over a small range, a square law seems reasonable.

The relations for e_{T_1} and e_{T_2} given by Equations (14) and (15) are reasonable approximations to the I-V characteristics of both Ge and GaAs tunnel diodes over the required ranges as shown in Figures 8 and 9.

$$e_{T_1} = V_p\left[1 - \sqrt{1 - \frac{i}{I_p}}\right], \tag{14}$$

$$e_{T_2} = V_v + (V_f - V_v)\left[\sqrt{\frac{i - I_v}{\Delta I}} + \frac{1}{3\Delta I}\sqrt{(i - I_v)(I_p - i)}\right], \tag{15}$$

where $\Delta I = I_p - I_v$ and V_f = forward voltage. Note that Equation (15) gives slightly lower voltages for the forward region, leading to pessimistic results in later calculations.

Substituting these expressions in Equation (12) and integrating

[8] J. Karlovsky, "Simple Method for Calculating the Tunneling Current of an Esaki Diode," *Phys. Rev.*, Vol. 127, p. 419, July 15, 1962.

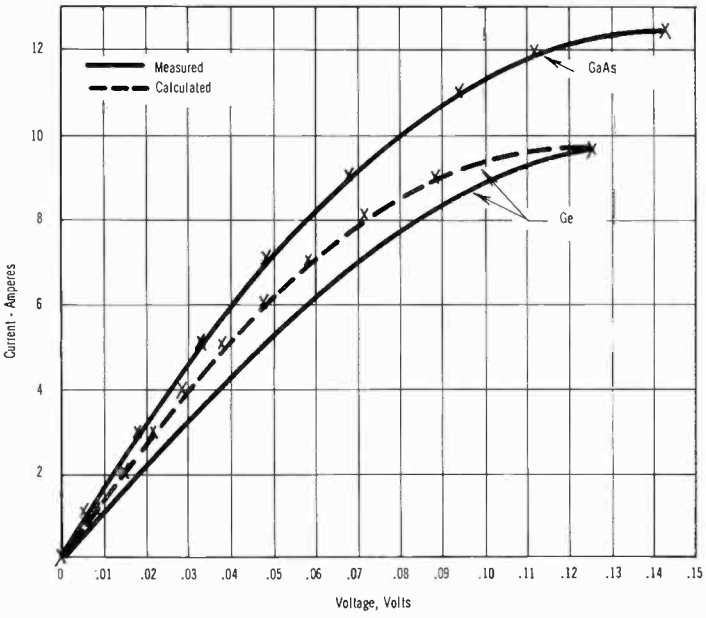

Fig. 8—Comparison between measured and calculated *I-V* characteristics of the tunneling region of gallium arsenide and germanium tunnel diodes.

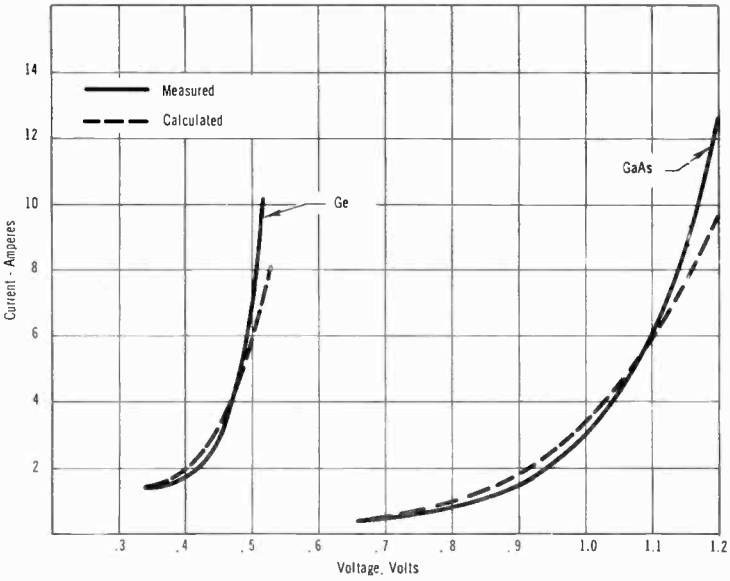

Fig. 9—Comparison between measured and calculated *I-V* characteristics of the forward region of gallium arsenide and germanium tunnel diodes.

gives the input voltage for given dwell points. However, to simplify the results, an approximation will be made by taking the mean diode voltages at the extremes of the dwell region (see Figure 7), i.e., taking the diode voltages at the currents given in Equation (11) and averaging.

Hence,

$$V_b = \frac{1}{4}\left\{ 2(V_v + V_p) + \frac{V_f - V_v}{\sqrt{\Delta I}}\left[\sqrt{I_b + I_m} + \sqrt{I_b}\right] + \right.$$

$$\frac{V_f - V_v}{3\Delta I}\left[\sqrt{(I_b + I_m)(\Delta I - I_b - I_m)} + \sqrt{(I_b)(\Delta I - I_b)}\right] -$$

$$\left.\frac{V_p}{\sqrt{I_p}}\left[\sqrt{\Delta I - nI_L - I_b} + \sqrt{\Delta I - nI_L - I_b - I_m}\right]\right\}. \qquad (16)$$

Equation (16) gives the input voltage, V_b, required for operation at a given load and given dwell points. With the exception of I_m and I_b, all the terms in Equation (16) can be obtained from the diode characteristics.

The magnetizing current, I_m, required to saturate the transformer core may be calculated from the core parameters and the number of primary turns

$$I_m = \frac{B_s}{\mu_s}\frac{1}{0.4\pi N}, \qquad (17)$$

where B_s = saturation flux density in gauss,

μ_s = permeability at saturation in gauss per oersted,

l = mean magnetic path length in centimeters,

N = one half the number of primary turns.

b. Output Voltage

Having established the required input voltage, the output voltage can be calculated using Equation (2). The exciting voltage $e_x = V_b - e_{T_1}$. Hence, the r-m-s voltage across each half of the transformer primary, V_T, is given by

$$V_T = V_b - e_{T_1}, \qquad (18)$$

since e_x is a square wave. Substituting in Equation (14) gives

$$V_T = V_b - V_p + \frac{V_p}{2\sqrt{I_p}}\left(\sqrt{\Delta I - nI_L - I_b} + \sqrt{\Delta I - nI_L - I_b - I_m}\right) \tag{19}$$

Equation (19) gives the r-m-s voltage across each half of the primary as a function of the load current. Using Equations (16) and (19), this voltage may be computed for any load and any input voltage.

Having calculated the r-m-s voltage across each half of the primary, the output voltage, operating frequency, power output and inversion efficiency of the inverter may be calculated.

The r-m-s output voltage is the product of the r-m-s voltage across each half of the primary and the ratio, n, of the secondary turns to half the primary turns. Therefore

$$V_{out} = nV_T. \tag{20}$$

c. Operating Frequency

It is known that

$$N\frac{d\phi}{dt} \times 10^{-8} = e_{rms}.$$

As the core is driven from $-\phi_s$ to $+\phi_s$ during half a cycle (see Figure 3c),

$$N\frac{2\phi_s}{T/2} \times 10^{-8} = V_T,$$

where T is the period of oscillation. Therefore,

$$f = \frac{V_T}{4\phi_s N} \times 10^8 \text{ cycles per second.}$$

Since $\phi = B_s A$, the operating frequency is given by

$$f = \frac{V_T}{4ANB_s} \times 10^8 \text{ cycles per second.} \tag{21}$$

d. Output Power

The output power is the product of the output current and voltage

$$P_{\text{out}} = nV_T I_L. \tag{22}$$

e. Inversion Efficiency

The inversion efficiency, η, is given by

$$\eta = \frac{P_{\text{out}}}{P_{\text{in}}}.$$

The input current is the sum of the diode currents during a full cycle. Therefore,

$$I_{\text{in}} = nI_L + I_m + 2I_v + 2I_b, \tag{23}$$

$$P_{\text{in}} = V_b\,(nI_L + I_m + 2I_v + 2I_b), \tag{24}$$

and

$$P_{\text{out}} = V_T nI_L. \tag{25}$$

Therefore

$$\eta = \frac{V_T nI_L}{V_b(nI_L + I_m + 2I_v + 2I_b)} \times 100 \text{ percent}. \tag{26}$$

A summary of the equations predicting the performance of saturated square hysteresis loop core, push–pull tunnel-diode inverters is given in Table I.

Special Cases

a. Threshold Operation

As can be seen from Equation (16), the input voltage required for threshold operation (i.e., $I_b = 0$) increases from zero load to full load. Since the output voltage from the power source will decrease with increased load, it is most important to consider V_b at full load.

If the input voltage is lower than that required for threshold operation, then one of two possibilities occur. One is that the inverter will cease to oscillate in the push–pull mode, reverting to inphase oscillation with zero output. A second possibility is that the inverter may operate in some other mode than that of push–pull saturated core inverters.

b. Maximum Load Current

The maximum load current that can be drawn from the inverter is

$$nI_{L(\max)} = \Delta I - I_m - I_b, \tag{27}$$

and hence it varies with bias voltage, decreasing as the bias voltage is increased. The output voltage, nV_T, increases with increasing bias

Table I—Analytic Expressions Predicting the Performance of Saturated Square Hysteresis Loop Core, Push-Pull Tunnel Diode DC to AC Inverter

Bias Voltage	$V_b = \frac{1}{4}\left\{ 2(V_v + V_p) + \frac{V_f - V_v}{\Delta I}\left[\sqrt{I_b + I_m} + \sqrt{I_b} \right] + \frac{V_f - V_v}{3\Delta I}\left[\sqrt{(I_b + I_m)(\Delta I - I_b - I_m)} + \sqrt{I_b(\Delta I + I_b)} \right] - \frac{V_p}{I_p}\left[\sqrt{\Delta I - nI_L - I_b} + \sqrt{\Delta I - nI_L - I_b - I_m} \right] \right\}$	(16)
Output Voltage	$V_T = V_b - V_p + \frac{V_p}{2\sqrt{I_p}}\left(\sqrt{\Delta I - nI_L - I_b} + \sqrt{\Delta I - nI_L - I_b - I_m} \right)$	(19)
Frequency	$f = \frac{V_T}{4ANB_s} \times 10^8$	(21)
Input Current	$I_{in} = nI_L + I_m + 2I_v + 2I_b$	(23)
Input Power	$P_{in} = V_b[nI_L + I_m + 2I_v + 2I_b]$	(24)
Output Power	$P_{out} = nV_TI_L$	(25)
Inversion Efficiency	$\eta = \frac{nV_TI_L}{V_b[nI_L + I_m + 2I_v + 2I_b]} \times 100$	(26)

voltage. Hence, the power output should peak at some input voltage where the increase in nV_T is greater than the reduction in $nI_{L(\max)}$. The peak efficiency, however, will occur at some combination of load and bias voltage not necessarily the same as that for maximum power output.

c. Overload Condition

If the maximum load current defined by Equation (27) is exceeded, the diode supplying the load current will switch to the high state. This is because the diode current can only increase to I_p, at which time $di/dt = 0$, and e_x becomes zero, so that the voltage equilibrium is disturbed and the diodes switch.

Thus, under overload conditions, the switching of the diodes is no longer controlled by the saturation characteristics of the transformer, and normal inverter operation ceases. The d-c input current will reach a maximum value of $I_p + I_v$, and cannot exceed this level if the diodes are oscillating. Hence, in the tunnel-diode inverter, no external overload or short-circuit protection is required.

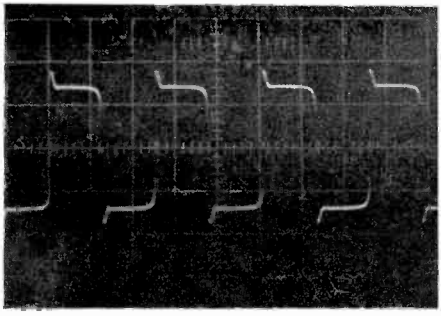

Fig. 10—Output waveform of a saturated-core push-pull tunnel-diode inverter—no-load condition.

Tunnel-Diode Inverter Performance

Several tunnel diode inverters ranging in output from 3 watts to 200 watts were fabricated and tested. The low-power inverters were operated from a low impedance, low-voltage regulated power supply, while the high-power units were tested with a homopolar generator as the power source. The power output was determined by measuring the r-m-s voltage across a known load resistance, and computing the power using the relation $P_{out} = V_{rms}^2/R_L$. Input current and voltage were measured using calibrated low-resistance shunts and voltmeters, and operating frequency was measured with a frequency counter.

Output Wave Shape

From Figures 3 and 5, it can be seen that the predicted waveform, under all load conditions, is a square wave. Figure 10 is an oscillogram of the waveshape of an unloaded inverter taken at the secondary ter-

minals. Notice that it is a good square wave, but that there is a spike on the leading edge. This spike is the overvoltage due to the tunnel-diode current rising rapidly from the dwell region ($I_v + I_m$ at no load) to I_p before switching to the forward region of its characteristic.

It would, therefore, be expected that as the inverter is loaded, the amplitude of the spike would be reduced, since the dwell region approaches I_p, and that the spike would disappear at full load conditions.

Figure 11 shows an oscillogram of an inverter under full load. Notice that the wave shape is still square, and that there is no spike on the leading edge.

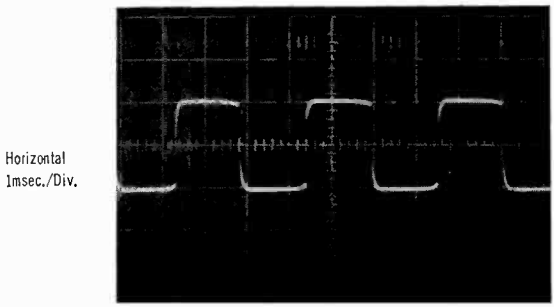

Fig. 11—Output waveform of a saturated-core push-pull tunnel-diode inverter—full-load condition.

Inversion Efficiency, Operating Frequency, and Input Current

Using Equations (16), (19), (21), and (22), inversion efficiency, operating frequency, power output and input current were computed for transformer No. 5B using 12-ampere GaAs diodes.

Figure 12 compares the variation of inversion efficiency, operating frequency, and input current, all computed for a given input voltage. Measured values are taken at the same input voltage and at power levels from 0 to 3 watts.

Comparison between the computed and measured performance shows good agreement. The curves are in excellent agreement, indicating the validity of the analysis. The discrepancy in operating frequency is easily within the errors in the specifications for saturation flux density and cross-sectional area of the core; furthermore, since the number of primary turns is small (3 per half), it is difficult to be precise. For example, a value of $B_s = 6800$ gauss was assumed, while the manufacturer's data shows that B_s may vary between 6600 and 8200 gauss.

It should be noted that in the computations, the transformer losses

are not taken into account. It would, therefore, be expected that the computed efficiency would be somewhat greater than the measured efficiency. However, test results (see Figure 12) indicate that at full

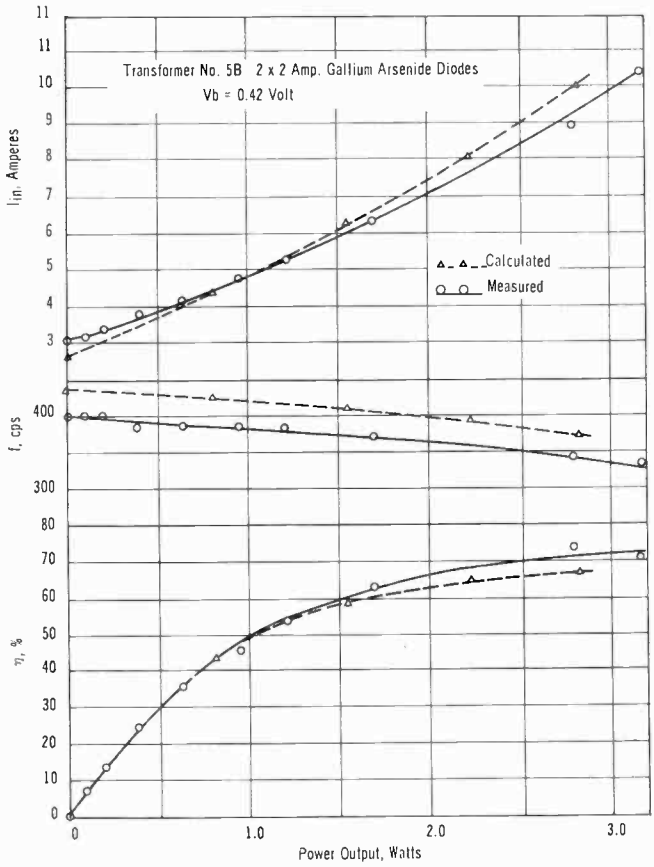

Fig. 12—Comparison between calculated and measured variation of efficiency, frequency and input current with load.

load the efficiency is somewhat greater than predicted. This can be explained as follows. As the load increases, the bias current, I_b, for a given bias voltage decreases, and as a result the high-voltage-state diode dwells closer to the valley region. As can be seen in Figure 9, the diode characteristic in this region is flatter than that calculated from Equation (15) and hence E_{T_2}, and thus V_T, are greater than the calculated values, leading to greater output power.

Figures 13(a) and 13(b) compare the variation of inversion efficiency, operating frequency and input current, computed at two input voltages, with measured values taken at the same two voltages at a power level of 40 watts.

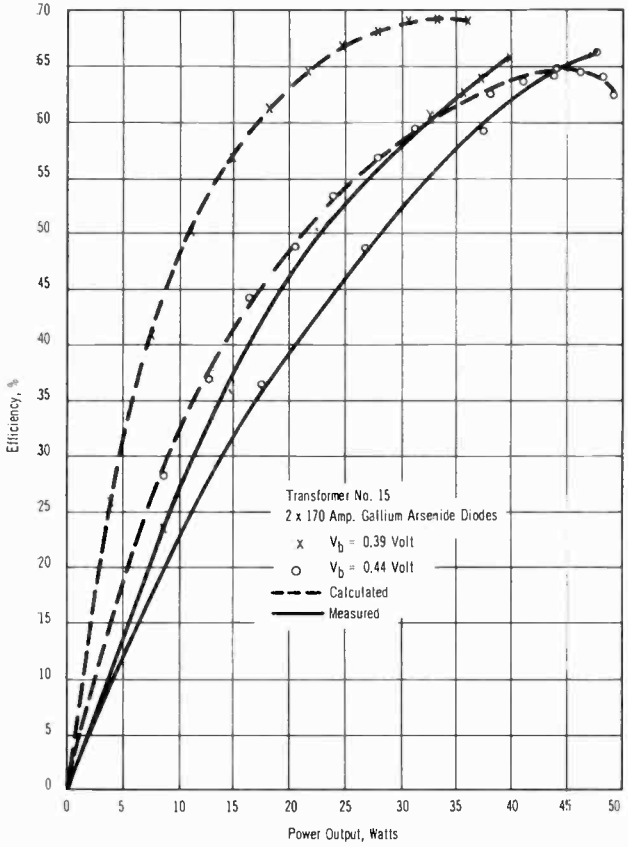

Fig. 13(a)—Comparison between calculated and measured variation of efficiency.

Notice that at this higher power level, the discrepancy between computed and measured efficiency and input current are quite large at partial load conditions, but at full load good agreement exists. It should also be noted that at the higher input voltages, the discrepancies are smaller. The difference between measured and calculated frequency can easily be explained as before.

Table II lists the performance of tunnel inverters with power out-

puts of 3 watts to 200 watts. In all cases efficiencies greater than the figure of merit were achieved. It should be noted that pairs of diodes with the same figures of merit will not necessarily have the same effi-

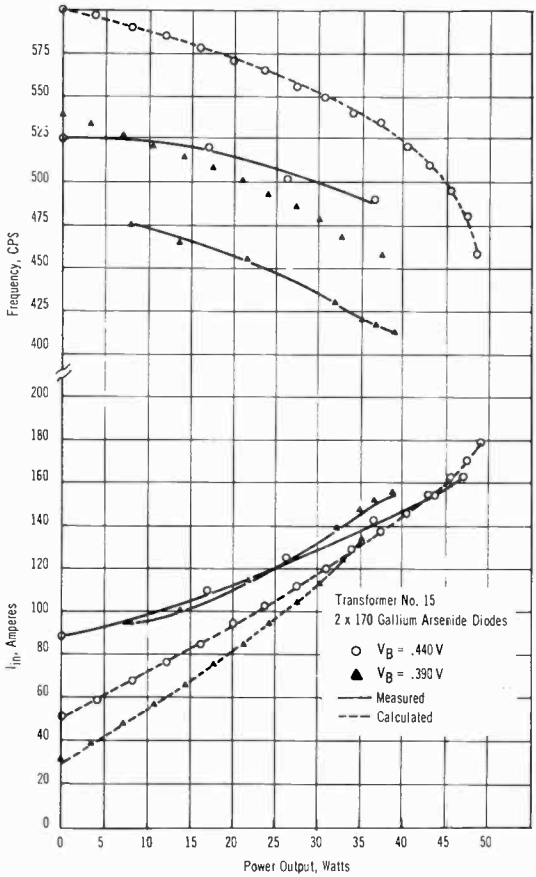

Fig. 13(b)—Comparison between calculated and measured variation of frequency and input current.

ciency in a circuit because of differences in the forward part of the *I-V* characteristic, which does not affect the figure of merit.

The discrepancy between measured and calculated efficiency and input current are due to second-order effects not significant at low power levels.

Second-Order Effects

As noted in the previous section, the major discrepancy between

predicted and measured inverter performance was observed when high-power inverters were operated at partial load. Under these conditions, the efficiency was much lower than predicted.

Investigation showed that the low efficiency was due to the input current being much greater than would be predicted at these partial-load conditions, the expected values being $I_m + 2I_v + 2I_b$ at open circuit and $I_m + 2I_v + 2I_b + nI_L$ when the inverter is loaded.

Further investigation revealed that under these no-load or partial-load conditions, the input current depended not only on I_m, I_v, and I_b, but also varied with the operating frequency, squareness of the core material hysteresis loop, circuit resistance, diode peak current, and magnetizing current. These effects are discussed in more detail below.

Table II—Comparison between Measured Efficiency and Diode Figure of Merit for Inverters of Various Power Levels

Diodes	Figure of Merit %	Power Output Watts	Measured Efficiency %	Frequency cps
12 amp	60	3	78	400
25 amp	61	6	79	400
170 amp	59	40	70	400
350 amp	55	80	68	400
600 amp	55	140	68	400
1000 amp	50	220	—	400

a. Effect of Hysteresis Squareness and Circuit Resistance

In the derivation of the theoretical expressions for efficiency, it was assumed that the total circuit resistance was zero and that the hysteresis loop of the core material used was perfectly square, i.e., $B_r/B_{(\max)} = 1$ where B_r is the remanence value of B. In practice, however, neither of these assumptions are correct, and at high power levels their effects are significant.

If the total circuit resistance, R_s, is not zero, but is smaller than the negative resistance of the tunnel diodes (a necessary condition for operation), then the voltage equilibrium equations become

$$\text{low-voltage-state diode:} \quad V_b - e_{T_1} - e_x - i_1 R_s = 0,$$

$$\text{high-voltage-state diode:} \quad V_b - e_{T_2} + e_x - i_2 R_s = 0.$$

When the core is saturated, $i_2 = I_v + I_b$, and since R_s is small, $i_2 R_s$

may be neglected. However, during switching i_1 changes from $I_v + I_b + I_m$ (assuming no load) to I_p. Also, if $B_r/B_{max} < 1$, $nd\phi/dt > 0$ after saturation, and a small voltage $e'_x (e'_x < e_x)$ will be developed as the low-voltage-state diode current increases toward I_p. The voltage equilibria are now:

$$\text{low-voltage-state diode:} \quad V_b - e_{T_1} - e'_x - i_1 R_s = 0,$$

$$\text{high-voltage-state diode:} \quad V_b - e_{T_2} + e_x = 0.$$

As e_{T_2} is much larger than V_b, and e'_x is small, the high-voltage-state diode will switch to a low-voltage state. However the low-voltage-state

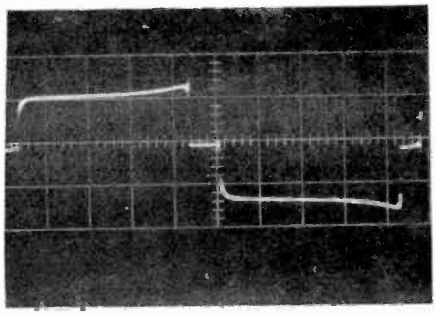

Fig. 14—Output wave shape showing step caused by poor squareness and high resistance.

diode will be delayed from switching, with the current increasing slowly to I_p, since e_x increases as dt decreases. Since $V_T = (e_{T_2} - e_{T_1})/2$, during this time $V_T = 0$, as e_{T_1} is small. Thus, poor squareness and high resistance prevent the diodes from switching simultaneously, leading to an input current greater than predicted.

As the squareness is improved, $d\phi/dt$ is reduced, and hence dt can decrease, i.e., the delay is lessened.

Figure 14 is an oscillogram of the output wave shape of the 40-watt inverter operating at partial load. The step can be clearly seen. At low power levels, these effects are very small. Figure 15 shows the variation of input current with input voltage under no-load conditions for a three-watt inverter. It can be seen that the measured and predicted values agree quite closely.

b. Effect of Operating Frequency

The delay caused by the poor squareness of the core-material hysteresis loop and circuit resistance is constant for a given core material

and primary circuit. Under these conditions, the operating frequency is determined by the core area alone. Thus, the lower the operating frequency, i.e., the greater the period of oscillation, the smaller the effect of the switching delay.

Figure 16 shows the variation of the input current with frequency and input voltage. It will be noted that the input current decreases

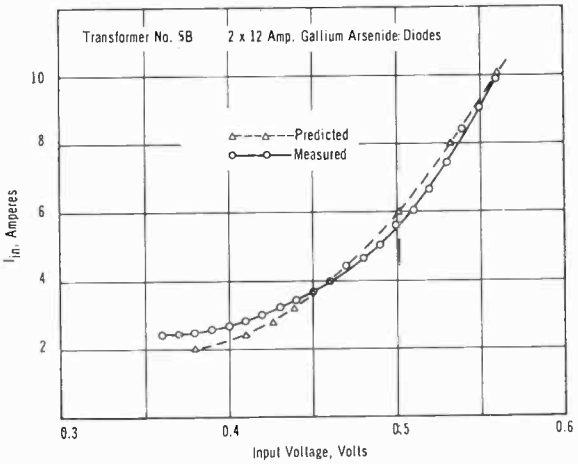

Fig. 15—Comparison between calculated and measured variation of input current with input voltage for open circuit.

with decreasing frequency to a minimum value at a given input voltage. This minimum occurs where $I_b = 0$.

c. Effect of I_p

For a given transformer (I_m, R_s, frequency, and squareness fixed) increasing peak current will increase the delay, and thus reduce the partial-load efficiency of the inverter.

d. Effect of I_m

For given core material and operating frequency, increasing I_m reduces the delay, since the current change in the diode is reduced.

Figure 17 shows the effect of increasing the magnetizing current, I_m. Three transformers were designed having I_m in the ratios 1:2:3, but the same operating frequency. It can be seen that for increasing I_m, the input current at no-load conditions decreases.

with frequency constant—no-load condition.

This effect is illustrated in Figure 19. Figure 19a shows the output just after switching on the motor, and Figure 19b shows the output with the motor at full speed.

This built-in short-circuit protection has the advantage of isolating the load from the supply, and by eliminating the need for external short

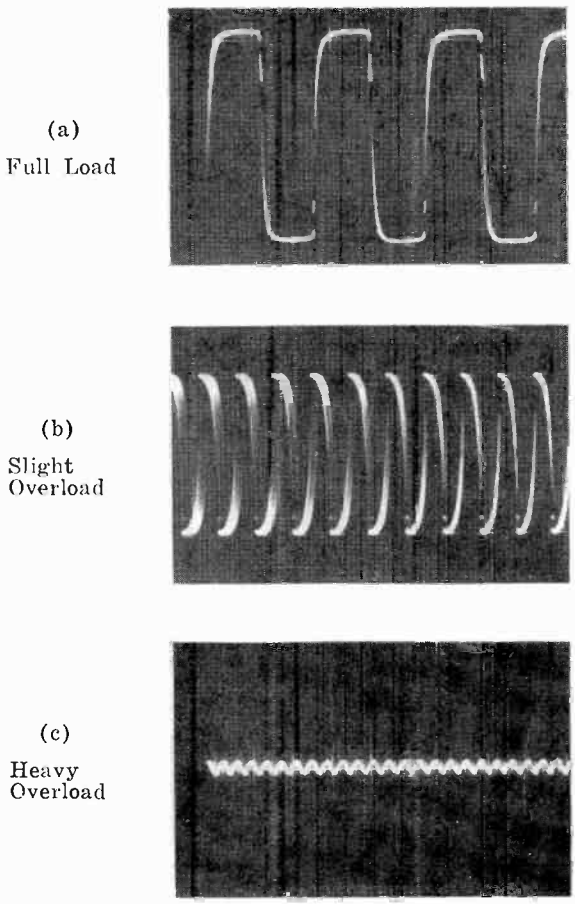

Fig. 18—Tunnel-diode inverter overload characteristic.

circuit protection, reduces the weight and complexity of the circuit. It also allows the inverter to be started under overload or short-circuit condition, with normal operation resuming after the overload is removed.

Operation at Elevated Temperatures

The major restriction on the operation of present tunnel-diode

inverters at elevated temperatures is the solder materials used in the diode fabrication. The dopant material and solders have relatively low melting points, limiting operation to about 100°C. These limitations may be overcome by replacing these solders with materials having

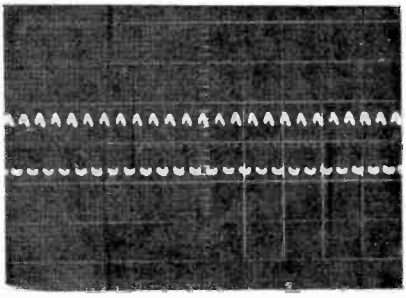

(a) Output waveform—motor switched on.

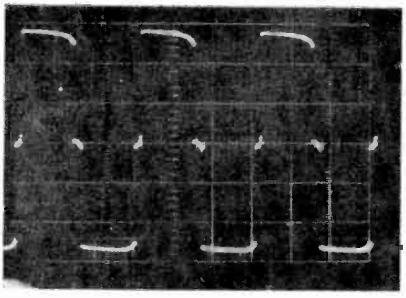

(b) Output waveshape—motor running at normal speed.

Fig. 19—Output waveshape of inverter showing effect of d-c motor starting load.

higher-temperature capability. However, such materials must be carefully investigated to obtain good electrical characteristics.

An analytic study was performed to determine the variation of efficiency with temperature, assuming the solution of the solder material limitation, and using the normal temperature coefficients of peak, valley, and forward voltages for tunnel diodes[9] (—0.1 mv/°C, —0.8 mv/°C and —1.1 mv/°C, respectively), and the usual variation of valley current with temperature.

[9] R. M. Minton and R. Glicksman, "Theoretical and Experimental Analysis of Germanium Tunnel Diode Characteristics," *Solid-State Electronics*, Vol. 7, p. 491, July 1964.

Figure 20 shows the variation of efficiency with temperature computed for diodes having a figure of merit of 69%. It will be noted that the efficiency remains at a high value over a wide range of temperatures, and is 66% at 200°C.

As the major effect of elevated temperatures is to lower the diode voltages, use of materials such as GaAs-GaP alloys with higher band gaps than GaAs could improve high-temperature performance, since the initial voltages would be higher.

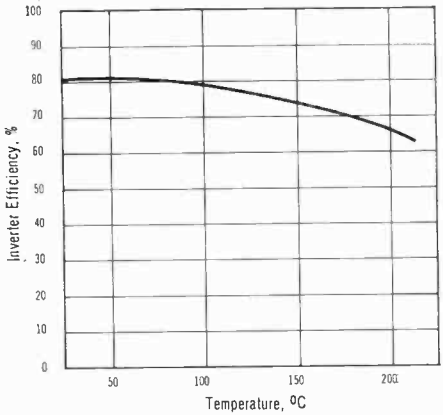

Fig. 20—Variation of inverter efficiency with operating temperature.

Operation with Thermionic Generator as a Power Source

The operation of tunnel-diode inverters with thermionic generators has previously been demonstrated[7] with an output of 20 watts being achieved. Further tests have demonstrated an output of 60 watts at 110 volts, again demonstrating the feasibility of obtaining useful power from thermionic-generator–tunnel-diode inverter systems.

Control of Frequency and Phase of Operation

The operating frequency of these inverters,

$$f = \frac{V_T}{4ANB_S} \times 10^8 \text{ cycles per second,} \tag{21}$$

changes with load as the diode dwell points, and hence V_T, changes with load. For applications where a constant operating frequency independent of load is required, or where both frequency and phase

of several inverters must have a given relationship, such as in a three-phase inverter, some form of control is required. As the tunnel diode is a two-terminal device, any control must be external to the diode.

Marzolf[10] described a circuit for using tunnel diodes in series, which was triggered by an external pulse generator. This idea was applied to the saturated-core, push–pull inverter to provide frequency and phase control of the inverter.

Although this circuit operates satisfactorily, it has the disadvantage of consuming relatively large powers and is critical in design. Therefore a simple circuit called the "Overload" circuit was developed.

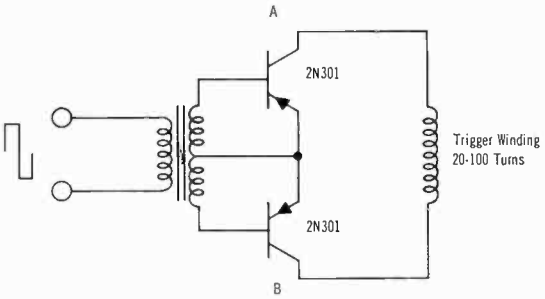

Fig. 21—Overload triggering circuit.

If an inverter is loaded such that the primary load current is greater than $\Delta I - I_b - I_m$, the transformer core can not be saturated, and a different mode of operation results. In this case, when V_p is reached, the diode must switch to the high-voltage state, even though the core is still unsaturated, as there can be no further current change, causing e_x to collapse and disturbing the voltage equilibria.

This effect is utilized for triggering by employing the simple circuit shown in Figure 21. Assume that the inverter is operating normally, and that at some time $T_{trig} = 0$, when point A is negative with respect to B, a trigger pulse is applied so that the base of transistor A is driven negative.

Under these conditions, transistor A conducts, and because transistor B is forward biased, this transistor also conducts. Thus, the trigger winding is short circuited, overloading the inverter and causing the tunnel diodes to switch to their opposite states. At this time, transistor A is forward biased, and remains conducting. However, transistor B is reverse biased, and has a positive base bias, and is turned off, unloading the trigger winding. Normal operation continues

[10] J. M. Marzolf, "Application of Tunnel Diode Static Inverter to Higher Input Voltages," U.S.N.R.L. Report No. 5802, June 1961.

be considered. This includes the case when a low operating frequency is required.

3) Ferrite cores, due to nonsquareness, low saturation flux density, and very low saturation permeability, are not suitable.

Shape of Core Material

In initial transformer studies, ring-type laminations were used because they provide a gapless core, and thus have the best saturation characteristics and the lowest losses. However, toroidal cores have the limitation of requiring either the use of sectional primary windings or flexible windings. As the d-c resistance of the primary must be kept in the low micro-ohm range for high-power inverters, toroidal cores become unattractive from fabrication considerations.

Thus, studies were made with transformers made with DU-type laminations, as this shape most nearly approached the gapless structure. Tests indicated performance similar to toroidal cores, and because of the ease of fabrication of primary windings, this shape was used for all high-power inverters.

Inverter Fabrication

The use of DU-type laminations allowed easy fabrication of very-low-resistance primary windings. The technique used was to mill a spiral cut in a thick-walled tube of appropriate dimensions, and then to braze the center tap and diode connections to the spiral. Figure 23 is a photograph of a completed primary winding.

The transformer is completed by assembling the laminations through both the primary and secondary windings, and then clamping the stack together. Figure 24 shows two views of a completed inverter with the tunnel diodes attached. The connections are made by bolting the transformer to the diodes and the diodes to a baseplate by insulated thru-bolts, so as not to short the diodes.

This type of construction allows simple fabrication and assembly with maximum flexibility in changing core material, secondaries, and diodes.

Computer Program

The hand computation of the performance of an inverter can be seen to be very time consuming because of the inter-relation of Equations (15) and (18).

Therefore, a computer program was written so that complete performance calculations could be performed quickly. The values of the diode and transformer parameters and the range of supply voltage and

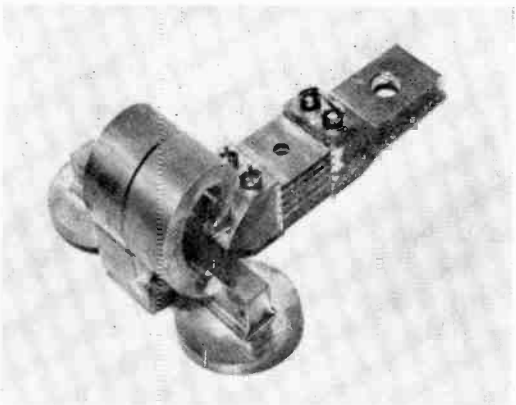

Fig. 23—Primary winding of a high-power inverter (200 watt).

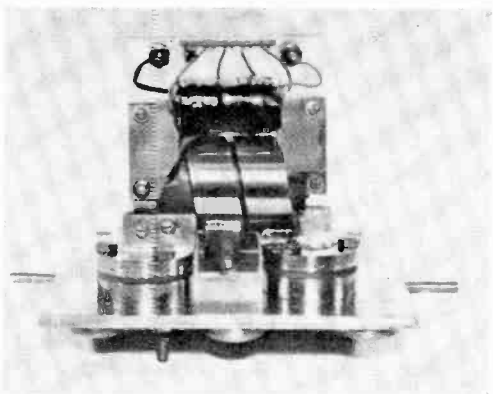

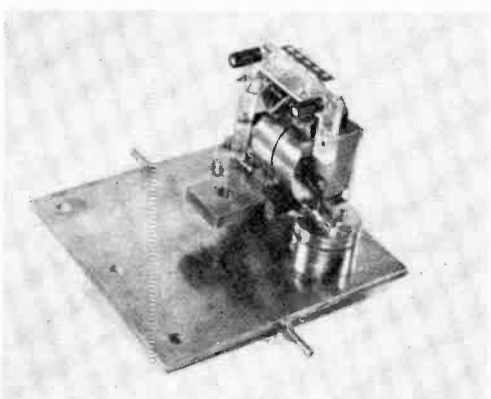

Fig. 24—Front and back views of a complete high-power inverter (200 watt).

load in question are supplied to the computer, and the performance expressions are solved using an interative approach to the V_b and I_b relation of Equation (15). By varying the value of V_b, a complete set of performance curves for this inverter can be calculated, or by changing transformer parameters, an optimum design may be achieved.

Conclusions

Detailed studies were performed on saturated-core push–pull inverters to determine their mode of operation and to optimize their design, particularly at high powers. A detailed theory of the operation of these inverters has been developed, including second-order effects such as core-material squareness factor and operating frequency, and equations have been derived that allow the design of and predict the performance of such inverters. These studies have shown that for saturated-core push–pull inverters, the previously accepted theory of operation is inadequate, and that efficiencies of 80 percent are attainable using tunnel diodes with figures of merit of 60 percent. It has been shown that the shape of the tunnel-diode characteristic and transformer design are the controlling elements in inverter efficiency. Thus, improvements in tunnel diodes from the use of materials such as GaAs-GaP alloy would provide efficiencies in excess of 80 percent and higher temperature capability.

Inverters with power outputs of up to 200 watts have been fabricated and tested, and guidelines for their design have been established. The tunnel diode inverter can also be operated at constant frequency with negligible loss in efficiency by external triggering. This feature also allows polyphase outputs, which was demonstrated with a three-phase inverter.

Because of its simplicity, high power to weight ratio, tolerance of overload and short-circuit conditions, high radiation resistance, and temperature capability, the tunnel-diode inverter is an attractive device for obtaining useable outputs with high efficiency from thermionic generators.

Acknowledgments

The authors gratefully acknowledge the contributions of R. Glicksman for his many helpful suggestions, and R. Buzzard, who programmed the equations for computer computation and who performed many of the tests. P. A. Hoss and L. Murray grew materials for the tunnel diodes, Mrs. E. Strouse fabricated the diodes, and P. Britt fabricated and tested the inverters. The authors are also indebted to B. J. Wilson, USNRL, and to M. Bell and A. Hom, who developed the homopolar generator used in testing the high-power inverters.

A SOLID-TO-SOLID DIFFUSION TECHNIQUE

By

J. Scott and J. Olmstead

RCA Electronic Components and Devices
Somerville, N. J.

Summary—*This paper describes a solid-to-solid diffusion technique that permits precise control over a large range of surface concentrations. The addition of a suitable dopant to an alkoxysilane results in a doped oxide film that is used as a diffusion source. The effects on the diffused-layer characteristics of impurity concentrations in the oxide, diffusion temperature, diffusion time, and diffusion ambient are presented. Methods of obtaining silicon dioxide layers by the pyrolytic decomposition of an alkoxysilane are also discussed.*

Application of this technique permits the simultaneous diffusion of n-type and p-type impurities without interaction, and still affords individual control of surface concentration of all areas. As a resu't, the number of high-temperature heat cycles required is reduced for many purposes, and greater flexibility in design is obtained. Because of the unique placement of the source, novel photolithographic techniques are possible.

This new diffusion technique provides ease of control and reproducibility. A comparison with conventional diffusion techniques is presented.

Introduction

THE CONTINUING increase in the number of diffusion techniques used to produce p-n junctions demonstrates the general dissatisfaction with the techniques available for the varying needs of the industry.[1] Examination shows that all these techniques are attempts to improve one of two basic systems. The first of these systems, generally referred to as the two-zone or carrier-gas process, has been described in detail by Frosch and Derick[2] (this work describes the diffusion system, together with the masking quality of silicon dioxide). The diffusion system consists of a furnace that contains two controllable heat zones. The impurity source is placed in the first zone, and the wafers to be diffused are placed in the second zone. A slightly oxidizing gas is then passed through the furnace and transports the vapor from the impurity in the first hot zone to the wafers in the second

[1] C. S. Fuller and C. J. Frosch, *Transistor Technology*, Vol. 3, Van Nostrand, New York, 1958; F. M. Smits, "Formation of Junction Structures by Solid-State Diffusion," *Proc. IRE*, Vol. 46, p. 1049, June 1958.

[2] C. J. Frosch and L. Derick, "Surface Protection and Selective Masking During Diffusion in Silicon," *Jour. Electrochem. Soc.*, Vol. 104, p. 547, Sept. 1957.

hot zone. The first hot zone controls the vapor pressure of the source and can be eliminated if the source used is sufficiently volatile at room temperature.

The second approach, which has been described by L. A. D'Asaro,[3] utilizes a closed box containing the wafers and the impurity source. The impurity is introduced from a solution of impurity oxide in silicon dioxide. When the box is heated to diffusion temperature, it fills with the vapors of the impurity. The silicon wafers then act as a "sink" for these impurities.

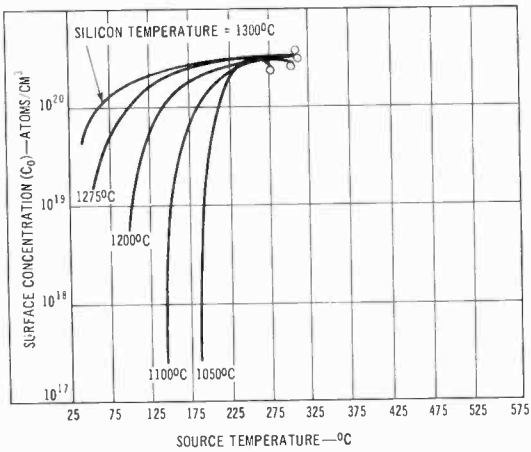

Fig. 1—Surface concentration as a function of source temperature for P_2O_5 two-zone diffusion system.

Both of these methods and their many variations have been applied with reasonable success for surface concentrations at or near the solid solubility of the impurity in the silicon at the diffusion temperature. For surface concentrations much below this value, however, these methods do not give reproducible results and become less controllable.

Figure 1 illustrates the problems encountered in attempting to achieve low surface concentrations. This figure shows surface concentration as a function of source temperature for a typical P_2O_5 two-zone diffusion system. It can be seen that control of source temperature is extremely difficult if a surface concentration less than about 10^{20} atoms per cubic centimeter is required.

The box method becomes troublesome because the whole system cannot approach a satisfactory near-equilibrium condition. (This is

[3] L. A. D'Asaro, "Diffusion and Oxide Masking in Silicon by the Box Method," *Solid-State Electronics*, Pergamon Press, 1960, Vol. 1, No. 1, pp. 3-12.

also true, but to a lesser extent, for the two-zone system.) In theory, the surface concentration is determined by the vapor pressure of the impurity source. The vapor pressure, in turn, is controlled by the temperature and, in the case of the box method, by dilution of the source. In practice, the walls of the box complicate the situation by becoming a secondary source, because the quartz box is a sink for the impurity. Near equilibrium can only be approached as the box becomes saturated with the impurity. Unfortunately, as the box approaches saturation, the surface concentration approaches the maximum solid solubility of the impurity in silicon at the diffusion temperature, i.e., the source effectively switches from the dilute mixture to the saturated walls of the container. Thus, the box method is acceptable only for high concentrations.

Because of these major difficulties, deposition and redistribution methods have been adopted to achieve values of surface concentration below the solid solubility. First, a short deposition step utilizing one of the above techniques is employed to saturate the surface with dopant. A drive-in step without the presence of the source is then used to redistribute the impurities and achieve the final depth and surface concentration. However, the fact that the redistribution is accomplished without the presence of a source changes the type of distribution from the complementary-error function to a modified Gaussian type. Furthermore, the control of depth and of surface concentration become interdependent, so that two steps are required and the process is thus less easily controlled. It is necessary to control two times and two temperatures, as well as the ambient, during drive-in. The latter is necessary because oxide is being regrown during the drive-in and a portion of the original impurity introduced in the deposition step is being consumed in the oxide.

The Solid-to-Solid Diffusion Technique

In an ideal arrangement for solid-state diffusion, the impurity partial pressure should remain constant and independent of diffusion time. Furthermore, the partial pressure should not be a strong function of temperature. Transport should be accomplished in such a manner that all areas of the wafer surface would be subject to equal impurity-flow densities. A close approximation of such an ideal arrangement would be to place an inert solid source containing the desired impurity in intimate contact with the silicon and diffuse from this solid at the same temperature.

The solid-to-solid diffusion process described employs an adaptation

of the technique described by E. L. Jordan[4] for the deposition of silicon dioxide films. Jordan describes the deposition of silicon dioxide by the pyrolytic decomposition of an alkoxysilane such as ethyl silicate. In the present process, simultaneous pyrolysis of a metal–organic compound containing the desired impurity is used to deposit an oxide containing this impurity on a silicon wafer.[5] Subsequent heating of the coated wafer results in diffusion of the impurity into the silicon. The surface concentration is then determined primarily by the concentration (impurity level) and diffusion coefficient of the impurity in the oxide. A single high-temperature diffusion step is employed to obtain this junction.

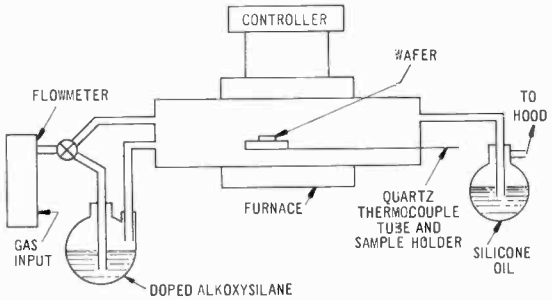

Fig. 2—Apparatus used for deposition of silicon dioxide films.

The concentration of impurity in the doped oxide depends on the partial pressure of the metal–organic compound during the deposition step. If the dopant is dissolved in the alkoxysilane, the partial pressure P_A of the dopant for an ideal system is given by

$$P_A = X_a P_a^0$$

where P_a^0 is the vapor pressure of the pure substance and X_a is the mole fraction of the dopant A. In a nonideal solution, the interaction of solute and solvent causes deviations from this relationship. In any case, there is a unique dependence of vapor pressure on the mole fraction, i.e., the proportion in the mixture determines the surface concentration.

Experimental Method

Figure 2 shows the apparatus used to accomplish the depositions. The carrier gas is saturated by passage through the bubbler containing

[4] E. L. Jordan, "A Diffusion Mask for Germanium," *Jour. Electrochem. Soc.*, Vol. 108, p. 478, May 1961.

[5] J. Scott and J. Olmstead, U. S. Patent 3,200,019.

the mixture of organo-oxysilane and the organic dopant. Pyrolysis of the gas in the hot zone of the furnace leads to the deposition of an impurity-containing silicon dioxide on the wafer. Because of the relatively low temperatures (approximately 750°C) and short times (approximately 10 minutes) involved, there is little or no diffusion into the silicon during the deposition step.

The diffusion is accomplished as described above and as shown in Figure 3. In step 1, the silicon wafer is cleaned and placed in the

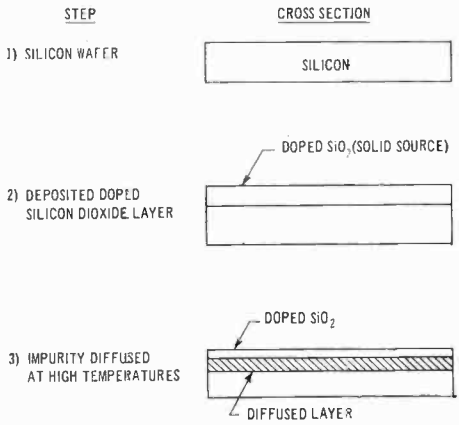

Fig. 3—Steps used in solid-to-solid diffusion process.

furnace. In step 2, the "doped" oxide is deposited. In step 3, the wafer is heated at the diffusion temperature for the desired time to obtain the required depth.

With this technique a wide variety of surface concentrations can be obtained easily once variables such as surface concentration as a function of impurity percentage in the bubbler have been established.

Experimental Data

The following data, which were generated for boron diffusion using trimethyl borate as the organic impurity, demonstrate the control available with this technique. Figure 4 shows the relationship between diffusion depth and the square root of time. This curve demonstrates the same time dependence observed with existing techniques.

Figure 5 shows surface concentration at various diffusion temperatures as a function of the percentage of trimethyl borate in the oxysilane solution for a 750°C, 10-minute deposition. It can be seen that the surface concentration can be controlled easily over two orders of

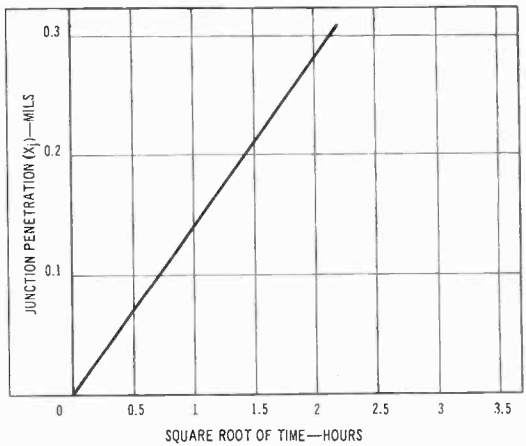

Fig. 4—Diffusion depth as a function of the square root of time for boron diffusion using trimethyl borate.

magnitude. Figure 6 shows the same type of data for a low-vapor-pressure organic tripropyl borate. The lower vapor pressure provides the advantage of a more constant mixture that does not deplete as easily.

Figure 7 shows surface concentration as a function of diffusion time. It can be seen that depletion occurs more rapidly with a diffusion source obtained by a one-minute deposition than with the thicker layer

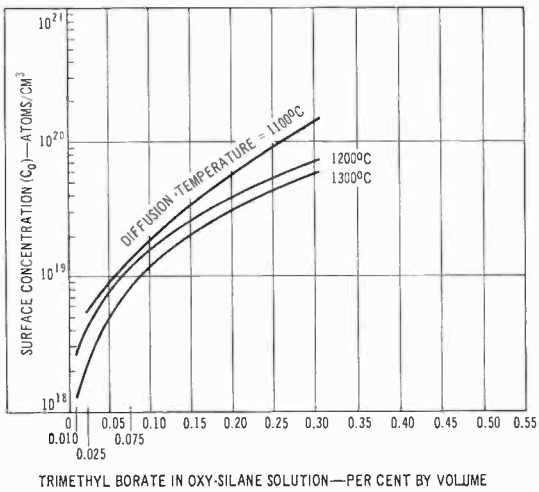

Fig. 5—Surface concentration as a function of solution concentration for three diffusion temperatures (750°C, 10-minute deposition).

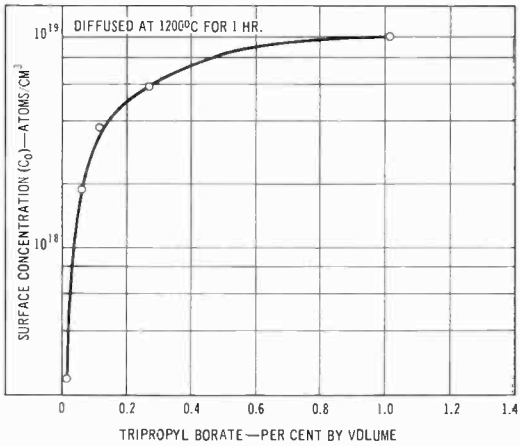

Fig. 6—Surface concentration as a function of solution concentration for low-vapor-pressure organic tripropyl borate.

of oxide obtained from a ten-minute deposition. The thicker oxide is a good approximation to an infinite source for the diffusion times indicated. The data shown in this figure and in Figure 4 support the assumption of a complementary-error-function type of impurity distribution. The curves of surface concentration as a function of time for three different diffusion temperatures in Figure 8 also demonstrate that the oxide source depletes very slowly with time and for most diffusions may be considered an infinite source.

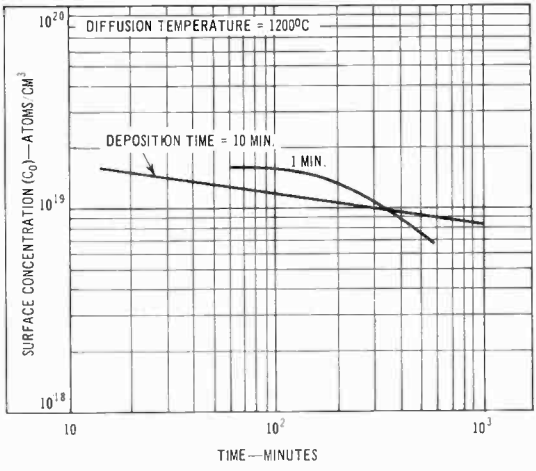

Fig. 7—Surface concentration as a function of diffusion time.

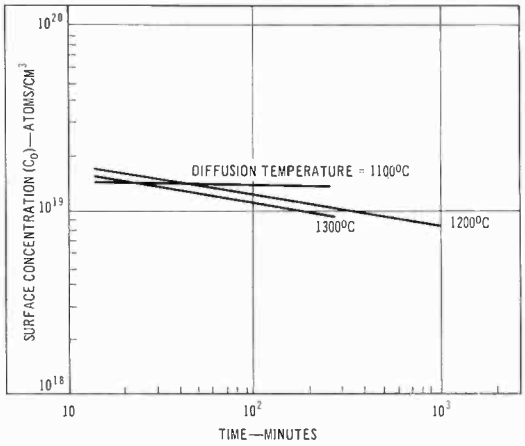

Fig. 8—Surface concentration as a function of diffusion time for three diffusion temperatures.

The middle curve of Figure 8 is replotted in Figure 9 for two types of diffusion ambient gas. The ambient gas can be used to obtain some further control of surface concentration. The differences in the diffusion process for different gases can be explained by the chemistry of the reduction of the impurity oxide. Most reported systems employ oxides of the impurities as the transporting species. These oxides must then be reduced to supply the silicon with the elemental impurity. This reduction occurs somewhere at the Si-SiO_2 interface.

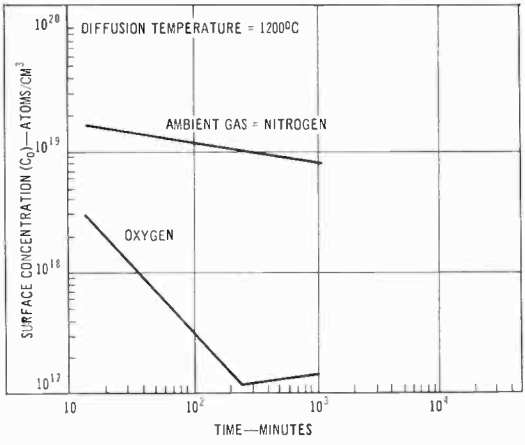

Fig. 9—Surface concentration as a function of diffusion time for two types of ambient gas.

If R represents a chemical impurity and RO its oxide, the reduction process proceeds as $2RO + Si \rightleftharpoons SiO_2 + 2R$. The dissociation reaction, $2RO \rightleftharpoons 2R + O_2$, is ruled out by a consideration of free-energy change for the reaction. While the first reaction is proceeding, the silicon also oxidizes by the reaction $Si + O_2 \rightleftharpoons SiO_2$.

If the oxygen concentration is decreased, the third reaction shifts to the left. The increase in concentration of silicon then shifts the first reaction to the right and thereby increases the concentration of the elemental impurity available for diffusion. In addition, as the concentration of oxygen in the ambient increases, oxide formation occurs at the interface of the doped oxide and the silicon, and the concentration at the surface is further reduced. Therefore, the ambient may have

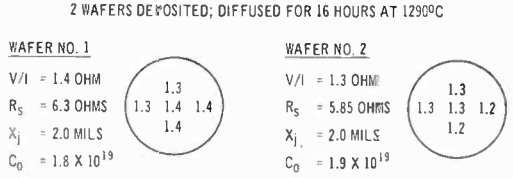

Fig. 10—Results obtained on two wafers prepared by new solid-to-solid diffusion technique.

control over both surface concentrations, C_0, and the concentration profiles obtained. Figure 10 illustrates the control of surface-conductivity parameters and reproducibility obtained utilizing this technique.

A system for n-type diffusions can be obtained in a similar manner by use of trimethyl phosphate in place of the trimethyl borate used for the p-type diffusion. As in the case of boron, the surface concentration is not a strong function of deposition time. A standard deposition time of 10 minutes and a temperature of 750°C were chosen for the following data.

Figure 11 shows surface concentration as a function of the percentage of trimethyl phosphate at temperatures of 1100, 1200, and 1300°C. These curves, which represent drive-in times of both 1 and 4 hours, show some dependence on time of diffusion. Figure 12 shows a slight dependence of surface concentration on diffusion temperature for various dilutions. Figure 13 shows that, as in the case of boron, an adjustment of the ambient gas produces a change in the surface concentration obtained.

The diffusion technique has one other major advantage in addition to the control of surface concentration and reproducibility. Placing

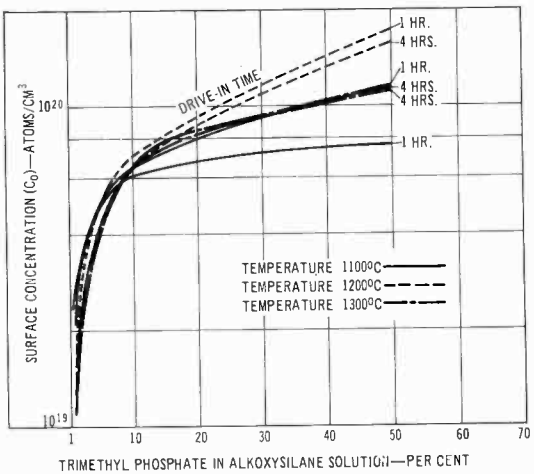

Fig. 11—Surface concentration as a function of solution concentration for n-type diffusions at three different temperatures.

the diffusion source directly on the surface of the semiconductor permits great versatility in selective solid-state diffusion. The versatility of the new system is best shown by a comparison with conventional diffusion methods. Figure 14 outlines the conventional sequence: growth of a silicon dioxide mask, etching of openings by photolithographic techniques, and then diffusion of impurities through the holes to form the p-n junction.

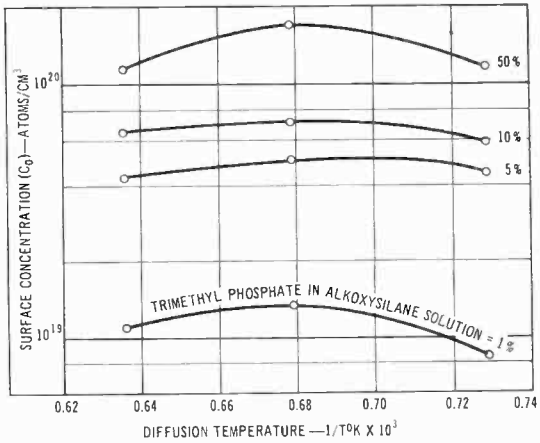

Fig. 12—Surface concentration as a function of diffusion temperature for various solution concentrations.

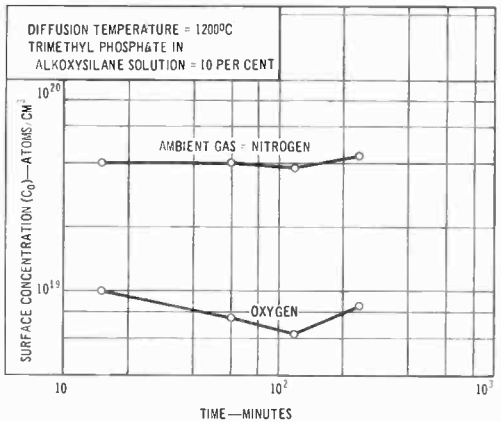

Fig. 13—Surface concentration as a function of diffusion time for two types of ambient gas.

In contrast, the use of a solid source provides a choice of sequences, as shown in Figure 15. The operation can be performed conventionally, or the procedure can be reversed so that the "solid source" is deposited over the wafer and then removed by photolithographic techniques from the areas where diffusion is not desired before the wafer is exposed to diffusion temperatures.

Because of this new flexibility, simultaneous diffusions of both p- and n-type impurities are possible. Simultaneous diffusions of p, p^+, n, n^+, and various other combinations have been carried out. Combination of this technique with existing diffusion methods makes possible

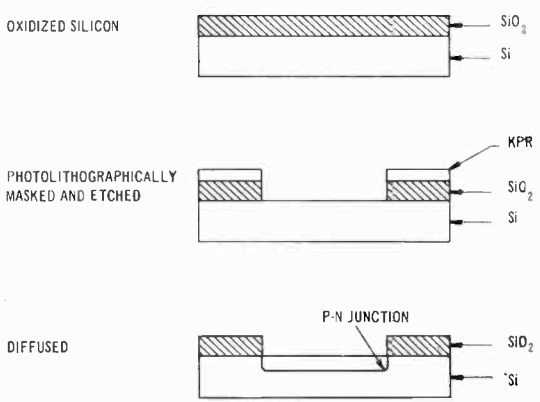

Fig. 14—Steps in conventional diffusion sequence.

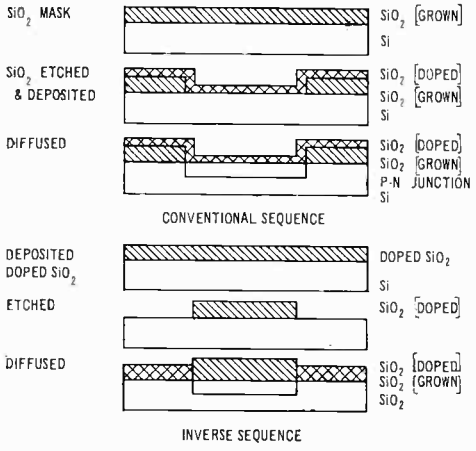

Fig. 15—Steps in solid-to-solid diffusion technique.

the fabrication of many complex structures that could not previously be made without the use of numerous high-temperature diffusions.

ACKNOWLEDGMENT

The authors wish to acknowledge the helpful suggestions and additional data supplied by W. J. Greig, J. A. Nava, and L. Krassner.

A CASSEGRAINIAN FEED FOR WIDE-BAND SATELLITE COMMUNICATIONS

By

P. Foldes, S. Komlos, N. K. Chitre, R. Schwerdtfeger, and T. Szirtes

RCA Victor Company, Ltd.,
Montreal, Canada

Summary—*Canada's first satellite communication ground station is located at Mill Village, Nova Scotia. The antenna is an 85-foot paraboloid with a new type of Cassegrainian feed system. The antenna covers a wide frequency range and has adjustable polarization, high efficiency, low noise temperature, and large power-handling capability. Automatic tracking in both direction and polarization is possible. The beam width of the feed is about the same in nearly all of the receiving frequency band (3700–4200 mc) and the transmitting band (5925–6425 mc). The antenna uses a multi-mode multi-horn source aperture that illuminates the hyperboloid–paraboloid reflector system with an optimum field distribution for both sum and difference modes. The low loss (about 0.25 db in the complete duplexer multi-mode coupler mode-filter system) and high quality of overall match (VSWR ≅ 1.25) is achieved by the use of high precision ridged waveguide elements. The main feature of the antenna is the precisely controlled primary pattern, which assures very low spillover radiation around the hyperboloid. As a consequence, the overall antenna efficiency is about —2 db in the receiver band, and about —3 db in the transmitter band.*

Introduction

In recent years, considerable effort has gone into the study of ground antennas for satellite communications systems. The basic problem is the provision of an antenna with autotrack capability and high gain/noise-temperature ratio at low cost. Since operation with several different satellite systems may be desirable, the antenna should be capable of operation over a wide frequency band and with various polarizations.

Analysis of existing and planned wide-band communication satellite systems indicates that the ground antenna should have a gain/system-noise-temperature ratio of at least 40 decibels for elevation angles of 5° or more (system noise is here expressed in decibels relative to 1°K). Because of inherent limitations on system noise temperature in the 4-gigacycle band, where the down-link frequency of presently planned satellite systems lies, an antenna gain of nearly 59 decibels for the received signal is required. Several approaches to the problem have been described in the literature.

The installation at Andover, Maine uses a horn reflector.[1,2] In other installations, the electrical advantages of the horn reflector have been combined with the structural simplicity of a symmetrical Cassegrainian arrangement.[3–5] In these installations, the horn reflector serves as the feed system, thereby assuring low spillover radiation. The possibility of still further structural simplification was shown by P. D. Potter[6] and P. A. Jensen,[7] who utilized higher order wave-guide modes in a relatively small source aperture in order to control the secondary pattern and obtain high gain/noise-temperature ratios. Foldes and Komlos[8] showed that optimum performance can be extended into difference modes and into a wide frequency band by using a multimode-multihorn source, resulting in an arrangement somewhat similar to Ricardi's 12-horn system.[9]

The present paper is a continuation of the work described in Reference (8). The design of the antenna was based on the following requirements:

(a) optimization of the performance-to-cost ratio for the overall antenna complex, where performance is characterized by the ratio of antenna gain to noise temperature;

(b) use of a minimum number of microwave component types;

(c) provision of large flexibility in operational modes, and coverage of wide frequency band in order to accommodate the feed for the possible change of frequency requirements;

(d) assurance of low circuit loss and difference mode minimum depth by the use of highly symmetrical waveguide cross sections;

(e) good aperture field distribution for the main reflector in the

---

[1] J. S. Cook and R. Lowell, "The Autotrack System," *Bell System Tech. Jour.*, Vol. 42, Part 2, p. 1283, July 1963.

[2] A. J. Giger, S. Pardee, Jr., and P. R. Wickliffe, Jr., "The Ground Transmitter and Receiver," *Bell System Tech. Jour.*, Vol. 42, Part 1, p. 1063, July 1963.

[3] C. E. Profera and A. F. Sciambi, "A High Efficiency Low-Noise Antenna Feed System," *IEEE PTGAP International Symposium on Space Communication*, Boulder, Colo., p. 83, July 1963.

[4] G. B. Von Trentini, "Erregersysteme für Cassegrain—Antennen," *Frequenz*, p. 491 (Sonderausgabe Bd 17/1963).

[5] S. P. Morgan, "Some Examples of Generalized Cassegrainian and Gregorian Antennas," *Trans. IEEE PTGAP*, Vol. AP-12, p. 685, Nov. 1964.

[6] P. D. Potter, "A New Horn Antenna with Suppressed Sidelobes and Equal Beamwidths," *Microwave Jour.*, Vol. 6, p. 71, June 1963.

[7] P. A. Jensen, "A Low-Noise Multimode Cassegrain Monopulse Feed with Polarization Diversity," *NEREM Record*, p. 94, 1963.

[8] P. Foldes and S. G. Komlos, "A New Multimode Monopulse Feed," *NEREM Record*, p. 100, 1963.

[9] L. J. Ricardi and L. Niro, "Design of a Twelve-Horn Monopulse Feed," *IRE International Convention Record*, Part 1, Vol. 9, p. 49, 1961.

receiver frequency band (3700–4200 mc) while maintaining at least −3 db efficiency in the transmitter (5925–6425 mc) frequency band (this requirement gives more importance to the receiving operation, which is the basic system limitation in any satellite communication ground station);

(f) provision of freedom for the field alignment of the feed relative to the main reflector;

(g) provision of both circular and orientable linear polarization (in changing the plane of polarization, movement or rotation of large elements is to be avoided).

Description of Overall System

Requirement (a) above virtually dictates the use of some form of Cassegrainian system. In this type of radio optics, the radiating source first illuminates a primary reflector, which in turn reflects the wave toward a secondary reflector. In the simplest form of Cassegrainian system, the radiating source aperture is small and the subreflector is in its far field. Then the subreflector is a symmetrical hyperboloid and the secondary reflector is a symmetrical paraboloid. Mechanical symmetry results in the simplest construction and minimum weight, and therefore was used as the basis of the antenna design. An 85-foot-diameter solid paraboloid with a focal distance of 36 feet and r-m-s surface tolerance (half-path-length error) of 0.040 inch is used for the main reflector. This type of paraboloid is relatively easily fabricated and has known mechanical characteristics. It represents a good compromise among weight/aperture-area ratio, rigidity, and weight of feed-support structure.

To illuminate such a relatively flat paraboloid with low spillover requires an illuminating aperture of 10 or more wavelengths. Therefore, an 8.5-foot-diameter hyperboloid subreflector with a focal distance of 18 feet is used. Such a subreflector is large enough to virtually eliminate spillover radiation around the edge of the paraboloid; the spillover radiation problem is thus transferred to the region around the edge of the subreflector.

The control of this spillover radiation and, more generally, the control of the illumination provided by the source system for the hyperboloid, is the central problem of any Cassegrainian antenna and is discussed later in more detail. The control of the illumination is dependent on proper field distribution in the source aperture. The purpose of the source system is to provide this distribution at its aperture where the guided wave (in the source) is launched into a freely propagating wave.

Figure 1 is a simplified block diagram of the radiating source system when it is operated in a linearly polarized mode that may be oriented in any plane. In principle, this system is relatively simple and, with the exception of the mode filter, does not contain any radically new elements. The transmitter (Tx) terminal (WR-159) accepts high power (up to 10 kilowatts CW) in the 5925 to 6425 megacycle band.

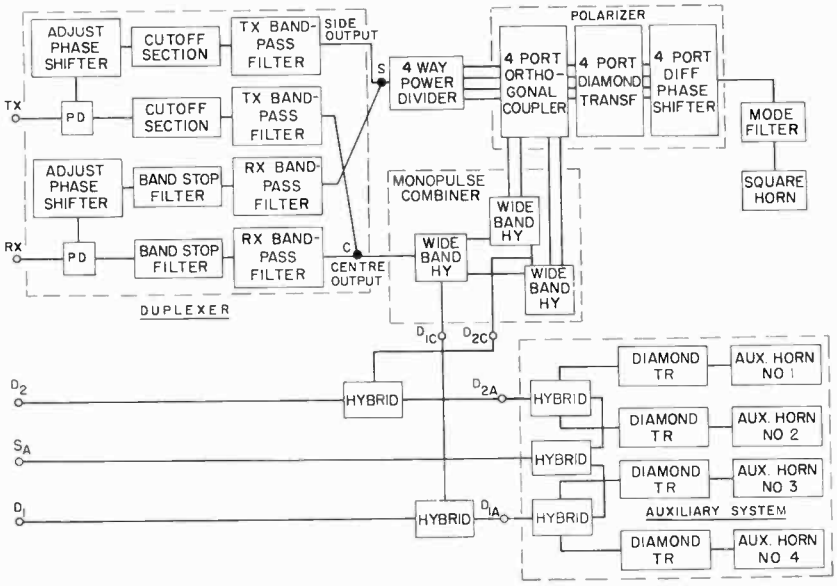

Fig. 1—Block diagram of feed system.

This power is divided into two equal parts. Each half of the power travels through a cutoff section and a band-pass filter that provide more than 125 db attenuation below 4200 megacycles and have less than 0.13 db attenuation for the Tx frequencies. In addition to these filters, the arm connected to the side output of the source system has an adjustable phase shifter using a short-slot hybrid with noncontacting plungers. The outputs of the Tx band-pass filters are connected to the receiver (Rx) bandpass filters at the junctions (S) and (C), which form the duplexing points, with negligible junction effects. Beyond these junction points, both the center and side-arm powers of the transmitter are divided into four equal parts by the use of identical wide-band hybrids. (The four-way power division is necessary to introduce monopulse tracking capability for the 3700 to 4200 megacycle receiving band). After these manipulations, the center and side-

arm powers are recombined in a four-port orthogonal coupler that has four square-waveguide outputs. Each of these cross sections support the TE_{10} and TE_{01} modes corresponding to the center and side outputs of the system. Each of these modes is decomposed in the following symmetrical diamond transformers and converted into a left and right circularly polarized wave by the 90° differential phase shifter that terminates the four-port circuit. Up to the output of this phase shifter, the system can be considered as a wideband four-horn system that radiates linear polarization where the plane of polarization can be oriented by the adjustable phase shifter. If the power divider following the Tx terminal is left out and the Tx terminal is directly connected to the center or side arm of the duplexer, then the system becomes left or right circularly polarized.

The waveguides between the four-port orthogonal coupler and terminals C and S have rectangular, double-ridged cross sections. These assure low loss in the Rx frequency band and the suppression of higher order modes at Tx frequencies. The wide-band folded hybrids have a Gaussian side-wall taper that results in the unique feature of better than —38 db reflection coefficient for the sum terminal and —46 db isolation for the difference terminal. The difference-mode terminal is matched only for Rx frequencies.

The waveguide cross sections between the orthogonal coupler and differential phase shifter (polarizer assembly) are square with ridge loading on each side. The orthogonal coupler is a wide-band version of a component described elsewhere.[10] The differential phase shifter is a waveguide section loaded by 11 irises that have a binomially tapered penetration. All the above-mentioned components have individual reflection coefficients of —37 db or better in the Rx and Tx frequency bands.

The four-port polarizer launches four individual TE_{10} modes into the mode filter, which is an oversized square-waveguide section with various loading elements. The mode filter has two basic purposes: (1) to match the four-port circuit to the multimode horn and (2) to produce a symmetrically tapered field distribution in the aperture of this horn. It should be emphasized that the matching conditions must be simultaneously fulfilled for the communication (sum) and tracking (difference) modes in their corresponding frequency bands. Furthermore, the matching elements must not destroy the axial ratio and main to cross-polarized difference-mode ratio. Additionally, the pattern-

[10] S. G. Komlos, P. Foldes, and K. Jasinski, "Feed System for Clockwise and Counterclockwise Circular Polarization," *Trans. IRE PGAP*, Vol. AP-9, p. 577, Nov. 1961.

shaping elements must work in such a way that the width of the pattern in the Tx band is about equal to that of the Rx band, although the Tx band is 60% higher in frequency. With the exception of some basic theoretical considerations regarding the cross section and length of the mode-filter section, the details of this element were determined by cut and try procedures. The end result was an oversized square-waveguide cross section capable of supporting the TE_{10}, $TE_{11} + TM_{11}$, TE_{20}, $TE_{21} + TM_{21}$, and TE_{30} modes. This waveguide, approximately 2λ long, has a series of crosses at the input end for matching the sum and difference modes and a series of posts at the output end for pattern shaping. The mode filter is followed by a square horn that has about a 5λ aperture size in the transmitting band.

The operation of the system for the received frequencies is basically identical to that for the Tx operation, except that the direction of propagation is opposite and that band-stop filters are used in the receive arm of the duplexer instead of the cutoff waveguide sections of the transmit arm.

The difference-mode operation of the system is somewhat unconventional, mainly because it combines two independent monopulse systems. One monopulse system is realized in the center multimode system and is obtained through the three wide-band hybrids of the monopulse combiner. This system is quite effective, even though the difference-mode aperture is only 1/2 the optimum value.[11] This limitation is removed by the addition of the auxiliary system, which is a standard four-horn monopulse system consisting of four circularly polarized rectangular horns located symmetrically around the multimode square center horn. The horns are diagonally fed, and circular polarization is achieved by the selection of horn length and aperture aspect ratio. The auxiliary and center systems together assure an optimum difference mode, i.e., they provide a spillover efficiency almost as good as for the communication mode, and thus provide good protection against ground reflections at low elevation angles. The combined difference modes (D_1 and D_2) also have the advantage of lower cross coupling than that which exists in the center monopulse system alone, and nearly constant difference-mode slopes with varying attitudes of incoming linear polarization.

Figure 2 is a photograph of the complete radiating source system prior to its installation into the feed-positioning mechanism and feed-housing cone. Figure 3 shows the hyperboloid subreflector positioning mechanism.

[11] P. W. Hannan and P. A. Loth, "A Monopulse Antenna Having Independent Optimization of the Sum and Difference Modes," *IRE International Convention Record*, Part 1, Vol. 9, p. 57, 1961.

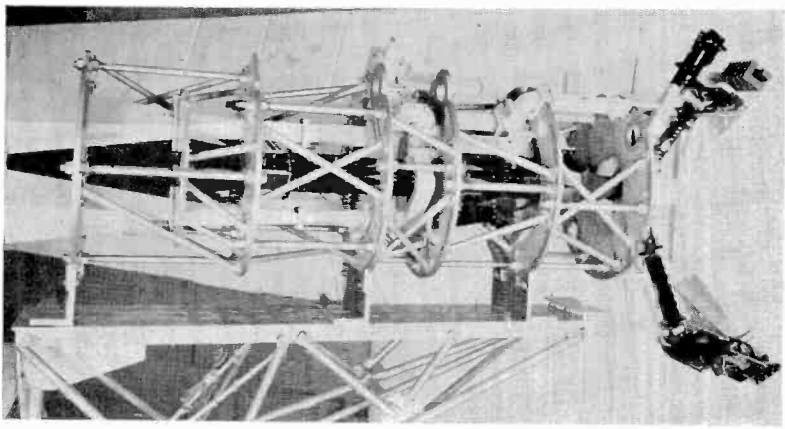

Fig. 2—Photograph of complete feed system.

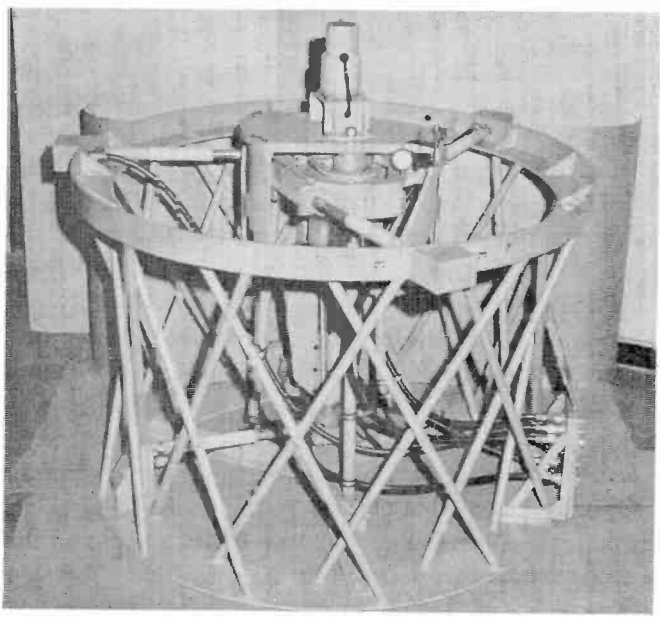

Fig. 3—Photograph of hyperboloid adjusting and mounting mechanism.

Mode-Filter Design

Electromagnetically, the most interesting component in the radiating source is the mode filter. Ideally it is a device that provides a transition between the four incident TE_{10} modes and the desired complex mode distribution in the aperture of the multimode horn. In principle, the field in the aperture of the multimode horn can be synthesized by the proper selection of the phase between the incident elementary TE_{10} modes and the geometry of the mode filter. Although it is not suggested that this complicated synthesis problem was solved or even completely understood during the present project, a description of the behavior of this element can be given.

The four-port to one-port transition in its basic, uncompensated form is a very effective mode generator, supplying a large number of modes. Even if the single-port (oversized) square-waveguide section is in cutoff for the $m + n \geq 3$ modes, some of these modes reach the horn, because a relatively short mode filter is required for wideband operation. This attenuation cannot be increased by the reduction of mode-filter cross section because the impedance-matching problem becomes unmanageable.

For sum-mode performance, the TE_{10}, TE_{21}, and TE_{30} modes are the most important. These will be abbreviated as α, δ, and ξ modes, respectively. The pattern of the combined $\alpha + (A \angle \phi)\delta$ mode differs primarily in the E plane from the pattern of the pure α mode, while the pattern of the $\alpha + (B \angle \phi)\xi$ mode differs mostly in the H plane. In the above expressions, A and B are the amplitude ratios, while ϕ is the phase difference between the modes in the aperture of the horn. Table I gives the sidelobe level, κ, in db and the 9-db width of the main beam (9 db was found to be the optimum edge illumination for the hyperboloid) in relative units for various amplitude ratios and mode phase differences. According to the table, an E-plane beam width to H-plane beam width ratio of 0.72 and E-plane side-lobe level of 13.2 db (with $A = B = 0$) can be improved to a beam-width ratio of 0.9 and E-plane side-lobe level of 19 db with $A = 0.6$, $B = 0.2$, and $20° \leq \phi \leq 60°$. As the propagation velocities of the δ and ξ modes are very close, it seems to be possible to keep these two modes nearly in phase. Then, the major problem is the adjustment of A and B and the phasing of the α mode relative to δ and ξ in the operational frequency band.

The adjustment of A, B, and ϕ is relatively easy experimentally when the frequency band is narrow (about 6 to 8%) and side-lobe level requirement is only 20 db. Double-frequency-band operation is somewhat more difficult, but still manageable when the VSWR require-

ment is not very stringent. However, it is quite difficult to obtain high-quality patterns and match in double the frequency band.

Figure 4 indicates the geometry of some of the most successful mode-filter configurations. Each of these arrangements has special

Table I—Pattern Characteristics of the $\alpha + (A \angle \phi)\delta$ and $\alpha + (B \angle \phi)\xi$ Modes

$\alpha + (A \angle \phi)\delta$	E plane							
A \ $\phi°$	0		20		40		60	
	κ (decibels)	θ_{9db}	κ (decibels)	θ_{9db}	κ (decibels)	θ_{9db}	κ (decibels)	θ_{9db}
0	13.2	.72						
.2	17.3	.78	16.8	.78	15.6	.78	14.5	.76
.4	23.5	.84	21.2	.82	17.2	.84	14.0	.79
.6	28.6	.90	25.5	.92	21.6	.92	19.0	.89
.8	37.5	1.06	37.5	1.06	21.2	1.08	18.0	1.20
$\alpha + (B \angle \phi)\xi$	H plane							
B \ $\phi°$	0		20		40		60	
	κ (decibels)	θ_{9db}	κ (decibels)	θ_{9db}	κ (decibels)	θ_{9db}	κ (decibels)	θ_{9db}
0	23.0	.99						
.2	27.0	1.04	27.5	1.02	25.6	1.00	24.0	1.00
.4	36.0	1.10	35.5	1.08	33.5	1.04	32.0	1.02
.6	40	1.18	38.6	1.18	34.0	1.14	31.1	1.10
.8	40	1.40	38.5	1.25	33.0	1.23	30.2	1.16

features that are advantageous for certain applications. The arrangement shown in Figure 4(a) results in very high quality patterns in about 10% frequency band by the fine adjustment of the coupling holes between the four individual waveguides. However, the matching of this coupling system requires additional posts or irises.

The cross arrangement, Figure 4(b), is quite good for double-frequency-band operation, and has the advantage that cross separation controls the match and pattern of the Tx band, while the posts con-

veniently shape the Rx pattern. The stepped transition of the arrangement in Figure 4(c) is a convenient way to balance the δ and ξ modes, and thus improve impedance behavior at the high-frequency end. It also has been a good matching characteristic for the difference modes. Finally, in the arrangement in Figure 4(d) (which was used in the present installation) a choke is connected parallel with the 4-port to 1-port transition as a means of obtaining a very high quality wide-band match.

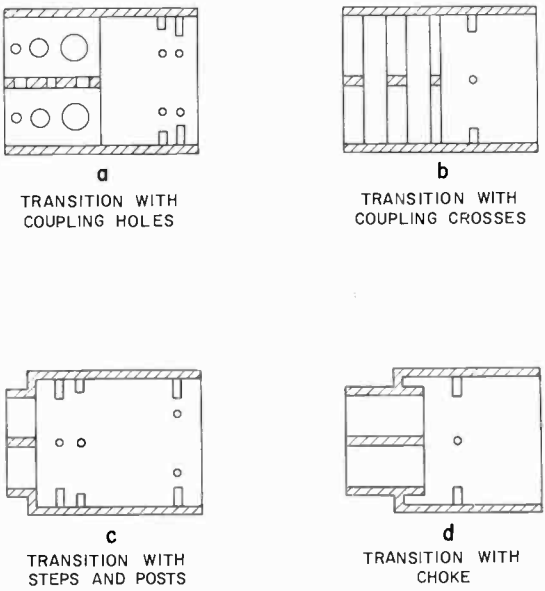

Fig. 4—Various forms of mode filters.

Figure 5 shows the average 9-db beamwidth ($\theta_{9\text{dbav}}$), average first side-lobe level (κ_{av}) and beam-width ratio $\theta_{9\text{dbE}}/\theta_{9\text{dbH}}$ with the arrangement in Figure 4(b) in double-frequency-band operation. For comparison, the figure shows the same characteristics for an identical-size square horn excited by pure TE_{10} mode. It can be seen, that the multimode horn has less elipticity in the main-beam cross section and lower side-lobe level. Both of these features improve the gain/noise-temperature of the overall antenna system.

The posts indicated in some of the mode-filter configurations are very convenient elements in shaping the sum-mode pattern, but they tend to increase the cross-polarized component in the difference modes. On that basis their penetration was restricted to assure at least 10-db cross coupling between the two difference channels.

High-Power Low-Loss Duplexer

Another special area of the feed system where some new components had to be developed is the duplexer. The primary function of the duplexer is to permit the use of a single antenna for simultaneous transmission at +70 dbm cw in the 6175 to 6425 megacycle band (F_{tb}) and reception of a —100 dbm signal in the 3960 to 4200 megacycle band (F_{rb}). The secondary function is to provide the selection of right or left circular polarization, or a linear polarization with any orientation.

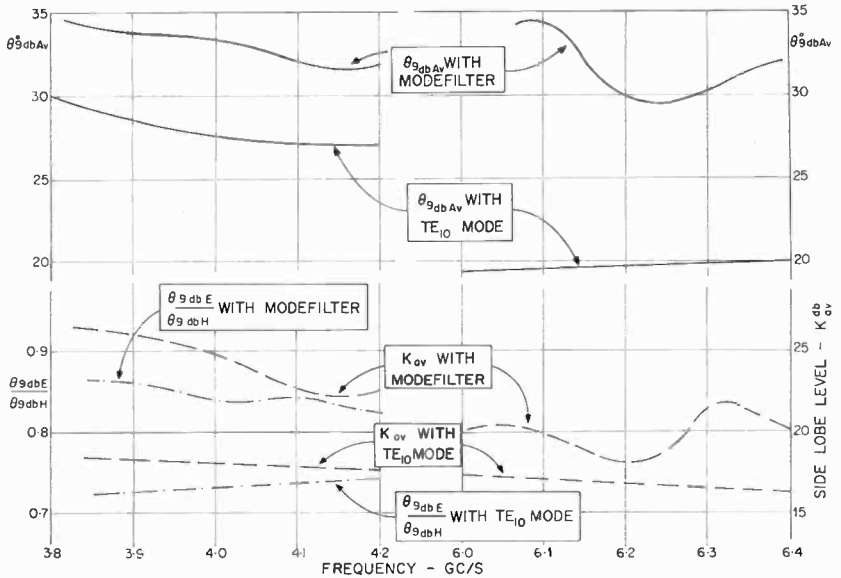

Fig. 5—Main characteristics of the source pattern for TE_{10} mode and for modes achieved by mode filter.

The indicated frequency bands are determined by the duplexer filters and could be shifted by substituting differently tuned filters. Figure 6 shows the assembly drawing of the duplexer, where the symbols Rx, Tx, and A indicate the receiver, transmitter, and antenna terminals, respectively. The receiver arm contains a band-pass filter for the receiver channel and a band-stop filter to provide extra isolation at the transmit frequency. Both of these filters are designed in a single ridged waveguide (SR175), and a transformer is provided to match this arm to the standard WR229 waveguide. The transmitter arm consists of a band-pass filter for the transmitter channel and a cutoff section to enhance the isolation in the receiver channel.

Since an extremely low noise temperature is required in the receiver band, the receive arm must provide a very low loss path for the received

signals so as to limit the duplexer's contribution to the system noise temperature. On the other hand, due to the extremely large difference (>170 db) in the levels of the transmitted and received signals, the duplexer must provide isolation between the Tx and Rx terminals greater than 185 db at the transmitter frequency and 100 db elsewhere, so as to limit the deterioration of receiver noise caused by interfering signals. Under these conditions the design must result in minimum noise for the receiver, whether it comes from thermal or intermodulation sources.

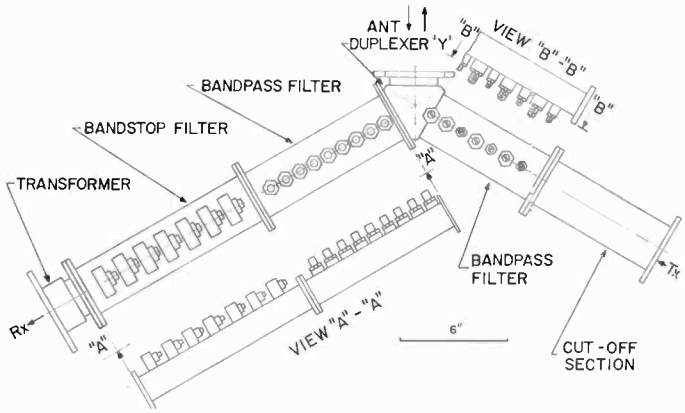

Fig. 6—Assembly drawing of duplexer.

Electromagnetically, the design must provide the largest possible slope for the transfer curve between the Rx and Tx terminals and between the highest receive and lowest transmit frequencies. A standard band-pass filter by itself cannot be expected to provide the largest ratio of isolation to pass-band loss, since it tends to have fairly large losses in the pass band and spurious responses at about 1.5 times the pass-band frequency. A band-stop filter alone would not be able to handle the high transmitter power (voltage limitation in the first cavity) and would provide isolation over only a narrow band. The optimum arrangement was found to be a band-pass filter providing more than 85 db isolation throughout the 5925 to 6425 megacycle transmit band and a band-stop filter to enhance this by another 100 db over a 70-megacycle band centered on the transmitter frequency. The total isolation of the filter combination is more than 100 db over the whole 500-megacycle transmit frequency band. For application where additional isolation is provided between the low-noise front and the mixer of the main receiver, this isolation is adequate for the whole

transmitter band. When such isolation is not provided, the band-stop filter must be changed whenever the transmit frequency is changed.

The total receiver channel loss in the duplexer is kept below 0.14 db, the major contributor being the band-pass filter (≈0.09 db) with the band-stop filter (≈0.04 db), the transformer, and the Y junction contributing the remainder. This represents a noise-temperature contribution of about 9.5°K. When the band-stop filter is removed, the noise-temperature contribution drops to 6.5°K.

In the transmitter arm of the duplexer, 125 db isolation is provided between the transmitter and receiver for the 4-gigacycle spurious signals originating in the high-power amplifier. The loss in the transmitter band is kept to a minimum (0.1 db) to prevent overheating of the duplexer due to absorption of the transmitter power.

A band-pass filter was included in the transmitter arm because it provides the possibility of tuning out reflections in the duplexer Y, more isolation at 4 gigacycles for a given pass-band loss, smaller physical size, and a certain amount of protection against the modulation products on the high-frequency side of the transmitter frequency band. It also provides an extremely well-defined short circuit at the receiver frequency. However, to provide 125 db isolation, a six- or seven-cavity design would have been needed; the compromise arrived at to reduce the complexity consists of a three-cavity band-pass filter contributing about 65 db isolation and a cutoff section adding another 60 db.

Duplexer Y

The duplexer Y is a symmetrical shunt junction that accepts a double-ridged waveguide (DR175) on the antenna port and has built-in transformers to single ridged waveguide (SR175) on the receiver arm and to rectangular waveguide (WR175) on the transmitter arm. The Tx band-pass filter is soldered to the Y, while the Rx band-pass filter is attached by a flange.

Transmitter Band-Pass Filter

The Tx band-pass filter is a three-cavity direct-coupled design in which TM_{01}-mode cylindrical cavities are used to minimize transmission loss in the transmit band and reflection loss in the receive band. The cross section of the filter is made up of three intersecting circles; the dimensions of the diameters and the spacings of the centers of the circles are such as to give proper response. The edges at the aperture have a 0.062-inch radius to give good high-voltage breakdown properties. Tuning screws, used only for fine adjustment of the match, have very small penetrations, thus increasing the voltage-handling

capability to nearly that of the undisturbed waveguide. In fact, power handling is limited by the heat production, and practical experience shows that no cooling fins are required for CW transmitter power output up to 10 kilowatts.

The Cutoff Section

The cutoff section is a six-inch length of special-cross-section rectangular waveguide (WR120) with transformers added on both ends. The width of the guide is chosen to maximize the ratio of isolation in the receive band to insertion loss in the transmit band in the TE_{10} mode. The height of the guide is the maximum permissible that will still prevent TE_{01}-mode propagation below 6425 megacycles. Two-step transformers adapt to WR175 on the Tx band-pass filter side and to WR159 on the output side. The transformers and cutoff waveguide are built in one piece.

The Receiver Band-Pass Filter

This unit is of the direct-coupled design in a single-ridged waveguide (SR175). The waveguide is optimized to provide minimum loss in the receive band without propagating the TE_{20} mode in the transmit band. The coupling posts are capacitive in the pass band and provide high isolation in the transmit band, where they are almost series resonant. The elements have no sharp corners, thus reducing the possibility of arcing at high power. Because the attenuation at transmit frequencies is more than 15 db per cavity, only the first cavity at the Y junction handles appreciable power.

Band-Stop Filter

The design consists of seven external cavities coupled to an SR175 waveguide through slots on the top wall, with the length of the slots controlling the stop-band width. The equal-cavity design gives a frequency response characterized by the Tchebychev functions of the second kind, i.e., maximum isolation for a given number of sections. The coupling lengths between cavities are approximately $3/4\ \lambda_g$ at f_T and are adjusted to give a reflection minimum in the receive band. Final matching in the receive band is achieved by small adjustments of tuning screws below each slot.

The maximum isolation of these filters is more than 135 db, too great to permit tuning and measurement on any conventional microwave bench. A special high-isolation swept-frequency setup has been developed for this purpose to plot isolations up to 135 db.

Twin Duplexer

In the actual twin-duplexer system, two of the above-described

duplexers are connected in parallel on two arms of the Rx band and Tx band power-divider hybrids. In this arrangement the arm connected to the side system of the feed contains the adjustable phase shifter, while a phase-compensating section is inserted into the other arm. When the phase shifter is in the center position, the phase-compensating section assures 0° (vertical) polarization at midfrequency. In this phase-shifter position, the polarization attitude may differ by ±3° from the vertical at the limits of the frequency band. When the phase shifter is at its end positions, the polarization is ±90° at midfrequency and is within 6° relative to this at band limits. Attitude error can be reduced by a more refined phase-compensating section, but this was not required for the present application. The attitude error was taken into account by calibration accurate to ±0.2°.

Table II—Cone Structure Characteristics

Overall Length	218 inches
Diameter at Base	96.1 inches
Diameter at Top	51.4 inches
Included Angle	11° 42′ 28″
Weight of Skin	1520 lbs.
Total Weight (including equipment)	4500 lbs.
Maximum Lateral Deflection at the Tip	0.025 inch
Lowest Natural Frequency Under Full Load (calculated)	50 cps

Mechanical Considerations

The feed system is made up of three somewhat independent subsystems, namely the microwave circuit, the feed cone, and the hyperboloid.

The microwave circuit consists of the radiating source and the duplexer. These units are supported by independent frames and can be readily separated for maintenance.

The main function of the cone, which is fabricated of 3/16-inch welded aluminum sheets, is to house and support the feed frame assembly and its positioning mechanism. The cone also houses parametric amplifiers, monopulse receivers, tunnel-diode amplifiers, downconverters, preamplifiers, noise-measuring equipment, and the like. In addition it can accommodate two men for maintenance or testing of equipment. A 1600 cfm blower changes the air in the cone every 10 minutes. Physical characteristics of the cone are shown in Table II.

The feed-horn assembly is so mounted that it may be adjusted ±2.5 inches in a direction perpendicular to its axis, ±7 inches parallel to its axis, and the axis may be tilted ±3°. These adjustments are used to ensure that the axis and phase center of the horn assembly coincide with the axis and focus of the paraboloidal dish, respectively.

The second major unit in the Cassegrainian feed is the subreflector assembly. The hyperboloid reflector has a five-degree freedom of movement. It can be moved along and rotated about two mutually perpendicular axes, both parallel to the aperture plane, and it can also be moved along the axis of the subreflector. The principle of operation

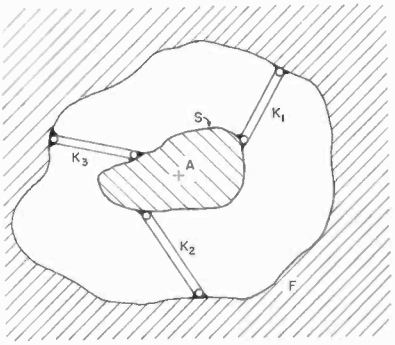

Fig. 7—Principle of hyperboloid adjusting mechanism.

can be described by the use of Figure 7 where the point A represents the axis of the subreflector, which is perpendicular to the plane of the drawing, S. By suitable adjustment of the bar lengths, K_1, K_2, and K_3, any desired lateral and angular position of the subreflector may be obtained. Figure 8 is a sketch of the most important parts of the mechanism. A reversible electric motor provides the axial motion of the hyperboloid.

Measuring Techniques

The successful development of a feed system, which is relatively complicated in fine details, depends to a very large degree on the measuring techniques used. It is beyond the scope of the present paper to give a full description of these techniques, but some of the more interesting ones are mentioned briefly.

Reflection Coefficient

The swept-frequency method is used for the measurement of reflection coefficient of the wide-band components. The necessarily wide-band

hybrid used as a directional coupler is a slightly modified version of the hybrid used in the monopulse combiner. This hybrid has better than —40 db isolation and better than —20 db reflection coefficient in the 3700 to 6425 megacycle frequency band for all terminals. For the measurement of reflection coefficient of the mode filter, the complete multimode coupler (monopulse combiner–polarizer assembly) was utilized. This was possible because the multimode coupler in itself was

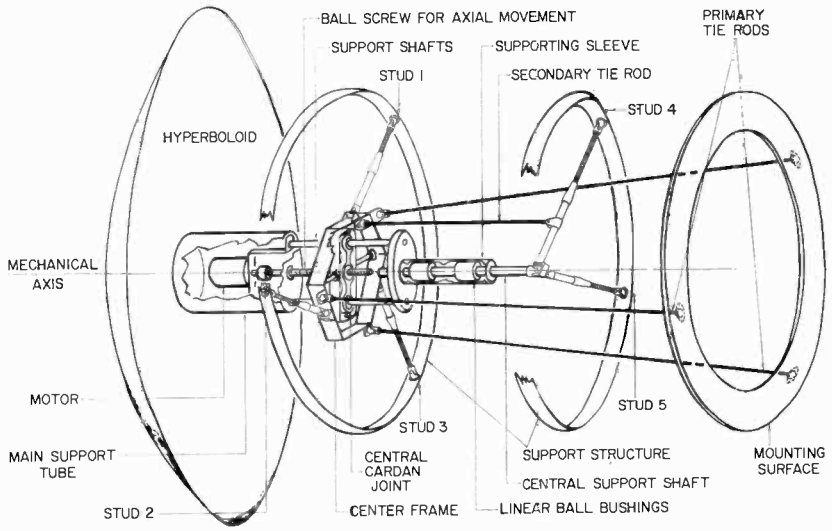

Fig. 8—Hyperboloid adjusting mechanism.

very well matched (input reflection coefficient better than —28 db when terminated by a four-port dummy load instead of the mode filter). Under the same loading conditions, the isolation between C and S or between D_{1C} and D_{2C} (see Figure 1) are all better than —35 db, and the axial ratio in the phase shifter is 1 db or better. When the multimode coupler is terminated by the mode-filter–horn assembly, the coupling between C and S measures the reflection coefficient of the mode filter for the sum mode, while the coupling between D_{1C} and D_{2C} indicates the reflection coefficient of the mode filter for the difference modes.

High-Isolation Measurements

In the development of high-rejection filters, it was necessary to monitor the transfer function of these components over a wide frequency band with a wide dynamic range. About 500-megacycle swept-frequency range and 140-db dynamic range was achieved by the use

of a circuit in which two sweep generators were locked together with 70-megacycle i-f frequency separation. The signal of one sweep generator was amplified by a 15-watt traveling-wave tube, while the other generator was used as the local oscillator at the receiving end, which has a 30-megacycle-wide i-f strip. Under these conditions the transfer curve of filters can be displayed on an oscilloscope, and tuning over the full frequency and dynamic range of interest is possible.

Low-Loss Measurements

For measurement of low transmission loss values, either dual channel Weinschel[12] equipment or a somewhat modified classical short-circuit technique[13] was used. Both of these techniques resulted in loss-measuring accuracies better than ±0.02 db. To measure such low loss figures, particular attention had to be paid to the waveguide flanges. Generally, lapped joints were used with a flatness of better than 100 microinches and surface roughness of about 8 to 10 microinches. Whenever practical, similar roughness values were maintained on the inside of the waveguide components. All the components were silver plated and the plating was protected by a thin layer of gold. As surface roughness was only about 1/3 of the skin depth, the theoretical conductivity value of a smooth silver surface was nearly realized.

The dual-channel loss-measuring equipment is ideal in the case of an essentially two-terminal component (such as a band-pass filter). However, for multiple-terminal circuits such as hybrids, the short-circuit method is more practical. A special arrangement had to be used for the loss determination of the polarizer, which requires a circularly polarized detector or short-circuit network. This component was measured by connecting two identical polarizers back to back and then terminating the whole assembly by a short circuit. Such an assembly behaves as a linearly polarized component and the measured loss is twice that of one polarizer.

Radiation Characteristics

The feed system was tested in an anechoic chamber 30 feet in length and about 20 feet in cross section. Wall reflections were below —40 db. The antenna was placed on a turntable, which made possible the rotation of the feed about its phase center. In most instances the feed was used as a receiving antenna. Two independent test signals were intro-

---

[12] "Dual Channel Insertion Loss Test Set," Weinschel Engineering Application Note No. 4, 1962.

[13] *Handbook of Microwave Measurements*, edited by M. Sucher and J. Fox, Chapters VI and VII, Vol. 1, Polytechnic Press, New York, 1963.

duced to probe the radiation pattern of the system under test. The main test horn was placed on a mount that permitted remote adjustment of its distance from the feed and of its polarization. This test horn was set at a distance of 18 feet (focal distance of hyperboloid) from the phase center of the feed and was directed along the axis of the chamber. An auxiliary test horn was also placed at the same distance but offset by about 4 feet in the 45° plane relative to the vertical. With this arrangement, the two test horns are approximately in the direction of the D_{1C} and D_{2C} difference-mode maximums when the turntable is rotated toward the auxiliary test horn by about 12° relative to the axis of the chamber. The main test horn is then connected to No. 1 sweep generator and the auxiliary horn to No. 2 sweep generator, both sweeping in the same frequency band. The feed is terminated by four identical detectors at the S, C, D_{1C}, and D_{2C} terminals. The No. 1 sweep generator is synchronized with two dual-beam oscilloscopes. The four detectors are connected to the four available channels of these oscilloscopes, which then show the signals received by the center-sum, side-sum, and two difference-mode terminals.

Under these conditions D_{1C} gives the horizontal difference-mode signal (main polarized) and D_{2C} gives the cross-polarized horizontal difference-mode signal (which ideally should be zero). The No. 2 sweep generator is synchronized to a third oscilloscope that is also connected to the detectors at D_{1C} and D_{2C}. When the turntable is rotated to $\theta = 12°$, this oscilloscope indicates the vertical difference-mode signal at $\theta = 12°$, but D_{1C} now corresponds to the cross-polarized signal and D_{2C} is the main polarized signal.

With this setup, virtually all the pattern characteristics can be monitored simultaneously, on a swept-frequency basis, while adjustments are made on the feed. With $\theta = 0°$ turntable position and continuously rotating main test horn, the oscilloscope pictures reveal the axial ratio and equality of the S and C sum-mode levels and the null depth (symmetry) of the difference modes for all frequencies and incoming polarizations of interest. With $\theta = 12°$ turntable position, where the difference-mode maximums of the center system are located, the axial ratio of the difference modes and the level difference between main and cross-polarized difference signals can be seen. At $\theta = 15°$, which corresponds to the edge of the hyperboloid, both the edge tapering and the axial ratio of the sum modes at that angle can be monitored. This direction of the sum modes corresponds to about —9 db edge tapering. If the axial ratio is within 2 db for the whole 0 to —9 db portion of the sum-mode beam, then two conditions are simultaneously fulfilled: (1) the main beam is nearly axially symmetrical and (2) the

side-lobe levels are about 18 db or better for any pattern cut or any incoming polarization. Finally, it was found that the smoothness of the received sum or difference signals (versus frequency) particularly at $\theta = 15°$, is a very good measure of the impedance match.

The only radiation characteristics that cannot be monitored by the above-described display are the phase patterns. For the measurement of these patterns, two separate homodyne[14] bridges were assembled, one for the 4-gigacycle and one for the 6-gigacycle band. Phase-measuring accuracy was about 1°.

For permanent recording of any of the radiation characteristics, discrete frequencies and continuously varying angles were used.

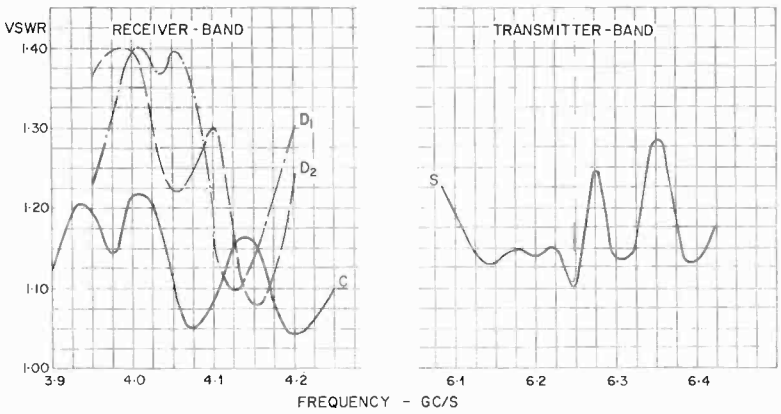

Fig. 9—Measured VSWR of the communication and difference channels (see Figure 1).

Experimental Results

Figure 9 shows the input VSWR measured at the communication and difference channel inputs. It can be seen that the reflection coefficients are generally —20 db or better. It was found that relatively high-quality matching was necessary in order to maintain the proper amplitude and phase relationships between higher order modes in the multimode horn, to keep the internal losses of the feed low, and to maintain good axial ratio for the sum as well as difference modes in the radiation pattern. Figure 10 shows the isolation characteristics of the duplexer. The actual isolation between the Rx and Tx terminals is about 25 to 30 db higher for the circularly polarized operation modes due to the additional isolation available in the orthogonal coupler.

[14] F. L. Vernon, Jr., "Application of the Microwave Homodyne," *Trans. IRE PGAP*, Vol. AP-4, p. 110, Nov. 1952.

Table III summarizes the loss values in the individual circuit elements. All values were determined by calculation as well as by measurements; the values given in Table III are measured values, except in the case of the mode filters and horn, where the measurement of loss was not possible. Although there were some minor discrepancies between the calculated and measured loss values for the individual components, these discrepancies averaged out, and the overall measured loss was within 0.02 db of the calculated value. It is significant to note the very low losses, in spite of the complexity of the overall circuit.

Table III—Summary of Loss Measurements and Equivalent Noise Temperature in the Rx Frequency Band

Frequency (megacycles)	3900	3950	4000	4050	4100	4150	4200	Average
Individual Circuit Element Loss (db)								
Power-divider hybrid	.018	.014	.014	.014	.014	.014	.014	
Adj. phase-shifter	.015	.013	.010	.010	.009	.009	.009	
Center-system duplexer #1	.062	.089	.076	.082	.087	.101	.114	
Side-system duplexer #2	.063	.090	.091	.087	.098	.103	.110	
Monopulse combiner	.053	.059	.047	.046	.045	.047	.046	
Side-system 4-way power divider	.090	.082	.077	.073	.085	.094	.083	
Polarizer (based on one channel)	.090	.080	.075	.069	.066	.078	.082	
Mode filter and horn (calculated)	.014	.013	.013	.012	.012	.011	.011	
System Loss, 185-db Isolation (db)								
Center-system	.252	.268	.235	.233	.233	.260	.276	
Side-system	.290	.292	.280	.265	.286	.311	.311	
Average	.271	.280	.253	.249	.260	.285	.293	
Circular polarization (center-system)	.219	.241	.211	.209	.208	.237	.253	.225
Linear polarization	.271	.280	.253	.249	.260	.285	.293	.270
System Loss, 85-db Isolation (db)								
Center-system	.232	.238	.205	.203	.203	.230	.246	
Side-system	.260	.262	.250	.235	.256	.281	.281	
Average	.241	.250	.223	.219	.230	.255	.263	
Circular polarization (center-system)	.189	.211	.181	.179	.178	.207	.223	.195
Linear polarization	.241	.250	.223	.219	.230	.255	.263	.240
Noise Temperature (°K), 185-db Isolation								
Circular polarization	13.9	15.4	13.4	13.2	13.2	15.1	16.1	14.3
Linear polarization	17.3	17.9	16.1	15.9	16.6	18.2	18.7	17.2
Noise Temperature (°K), 85-db Isolation								
Circular polarization	11.9	13.4	11.4	11.3	11.3	13.1	14.2	12.3
Linear polarization	15.4	15.9	14.2	13.9	14.6	16.3	16.8	15.3

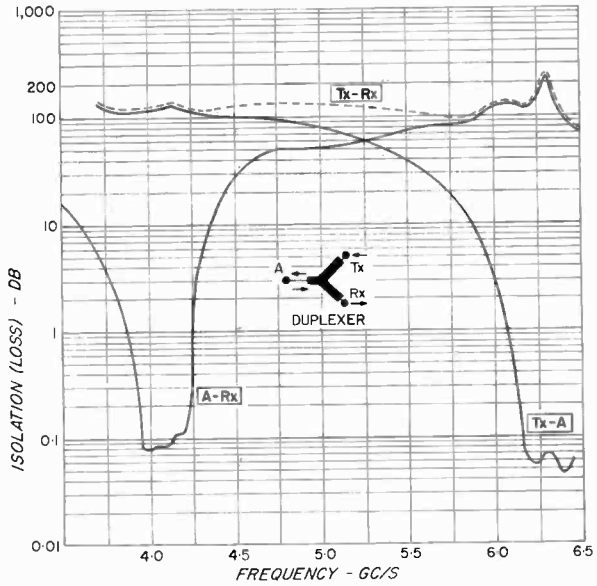

Fig. 10—Isolation (loss) between different terminals of high-power low-loss duplexer.

This indicates the importance of very high surface finish and high-quality impedance matching for low-noise applications.

Figure 11 shows the axial ratio versus frequency for the different radiation modes. The axial ratio for the sum mode is given along the

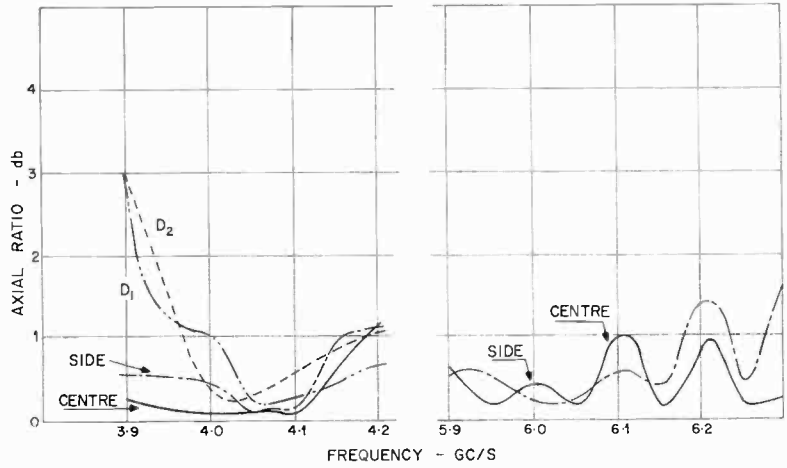

Fig. 11—Measured axial ratios (center and side sum at $\theta = 0°$ and differences at $\theta = 6°$ azimuth angle).

axis of the feed system, while that for the *resultant* difference modes is in the direction of the principal maximum (about $\theta = 6°$). It should be noted that these axial ratios are not the same as the axial ratios in the secondary pattern; however, they are closely related to them. The

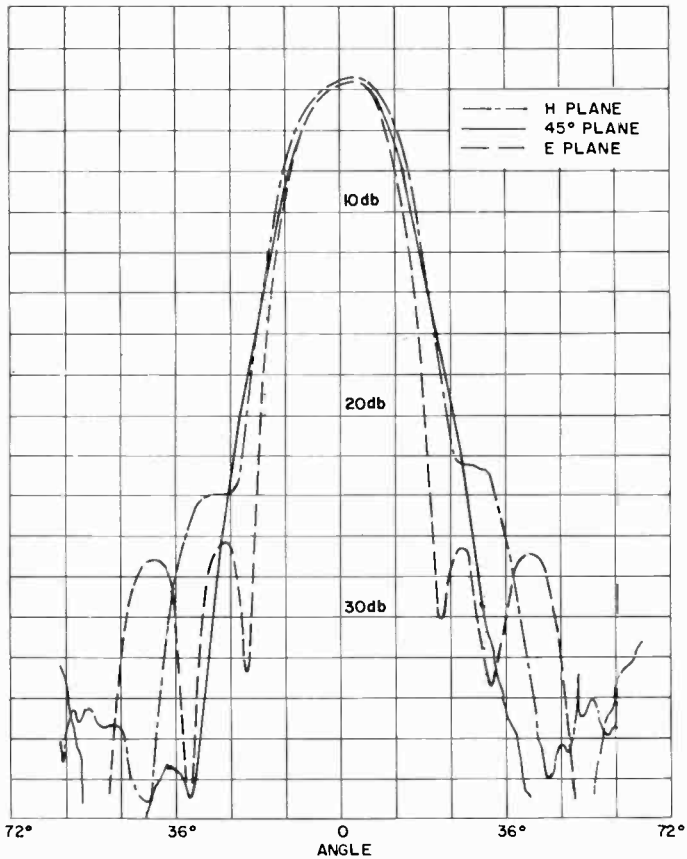

Fig. 12—Measured sum mode patterns in receiver band; $f = 4$ gigacycles, center system.

true secondary axial ratios can be determined from the complete polarization distribution of the primary patterns.

Figures 12, 13, and 14 show the communication receive (sum) pattern, the tracking receive (difference) pattern, and the communication transmit (sum) pattern. The pattern "cuts" were taken in the 0°, 45° and 90° planes. Note the very high degree of axial symmetry and

low side lobes of the receive patterns and the still optimum beam shape of the transmit patterns in spite of the 60% higher frequencies. Another important radiation feature of the feed is the nearly optimum beam width of the resultant difference-mode pattern as compared to the sum mode.

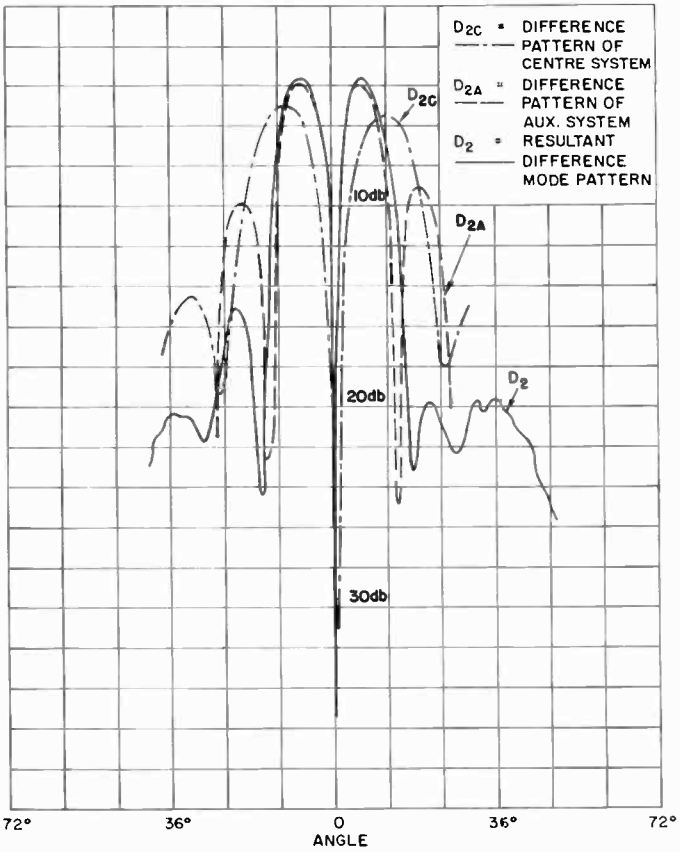

Fig. 13—Measured difference mode patterns; $f = 4$ gigacycles, 45° plane.

Figure 15 shows the effect of phase errors in the sum-mode pattern as a function of frequency. The data actually displayed is an equivalent r-m-s surface tolerance caused by the nonperfection of the source pattern. The equivalent r-m-s error was determined from three plane cuts of the phase patterns. It is interesting to note that the phase center itself is closer to the throat of the horn than for a basic mode horn, but has very small variation with the orientation of the horn or with

frequency. It was found that the phase center (P in Figure 15) was 6 ± 1 inches behind the 10-inch horn aperture for both the Rx and Tx frequency bands. The constancy of phase center position is related to the axial symmetry and frequency independence of the main-beam

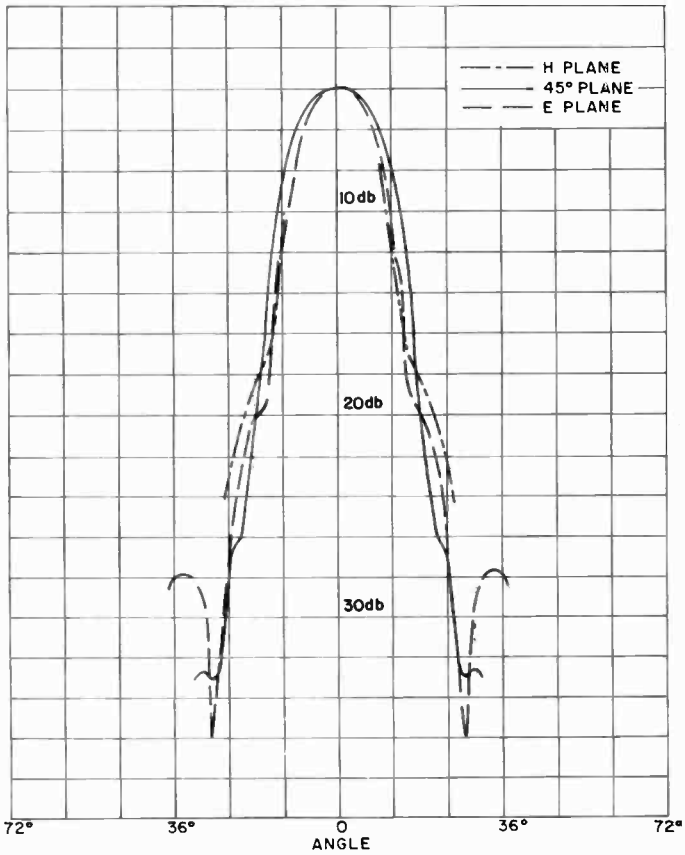

Fig. 14—Measured sum mode pattern in transmit band; $f = 6.2$ gigacycles, side system.

shape. The result is very significant, because it means a sharply defined point source and makes possible optimum focusing of the source relative to the hyperboloid in wide frequency band. Figure 16 indicates another important phase characteristic of the feed, namely the relative phase shifts at the various output terminals as a function of the attitude of incoming polarization. Generally, the phase between a signal at C and D_{1C} or D_{2C} varies slightly with changing input polarizations. This

change offsets the optimum alignment of the monopulse receiver, which operates on a phase–amplitude basis. It can be seen that for the combined overall system, in which the phase errors in the center and auxiliary system are averaged, the maximum differential phase error is less than ±5°, which is well within the tolerable practical limit. The graph also shows that the phase of the signals at C and S vary in the

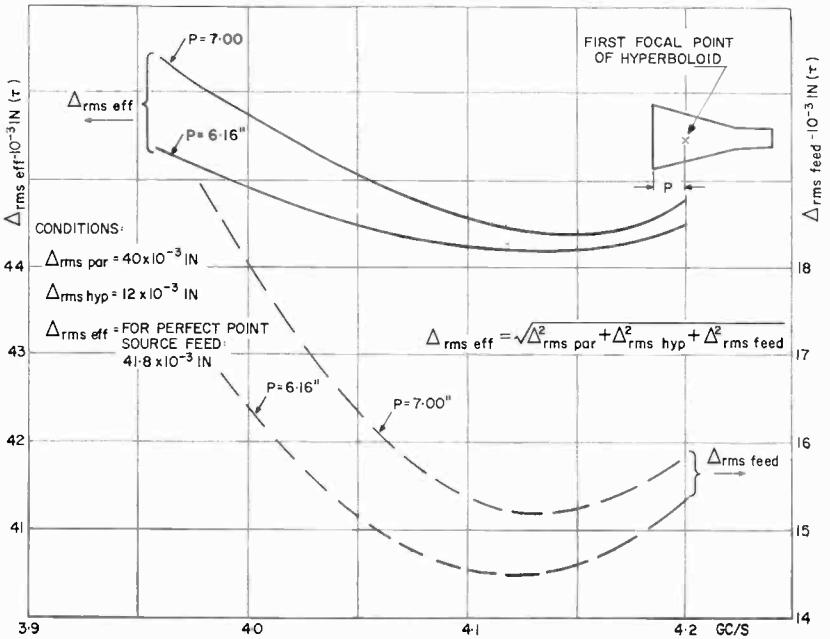

Fig. 15—Effective "surface tolerance" versus frequency.

opposite direction with a high degree of linearity. The symmetry and linearity of these curves are additional measures of the quality of circular polarization in the system, because for ideal circular polarization the curves become symmetrical straight lines. Note that D_{2C} difference signal should have zero amplitude in an ideal system if the feed is rotated in the plane of the D_{1C} signal; in practice, it has a finite value and opposite sense of polarization to the useful difference signal D_{1C}.

Calculated Secondary Characteristics

It is generally accepted that the secondary characteristics (gain and noise temperature) of a microwave optics system can be deter-

mined to a fair degree of accuracy by calculations based on a sufficient amount of primary (feed) pattern characteristics. The secondary radiation characteristics of large, complex antenna systems are quite difficult to measure directly, and the accuracy of such measurements

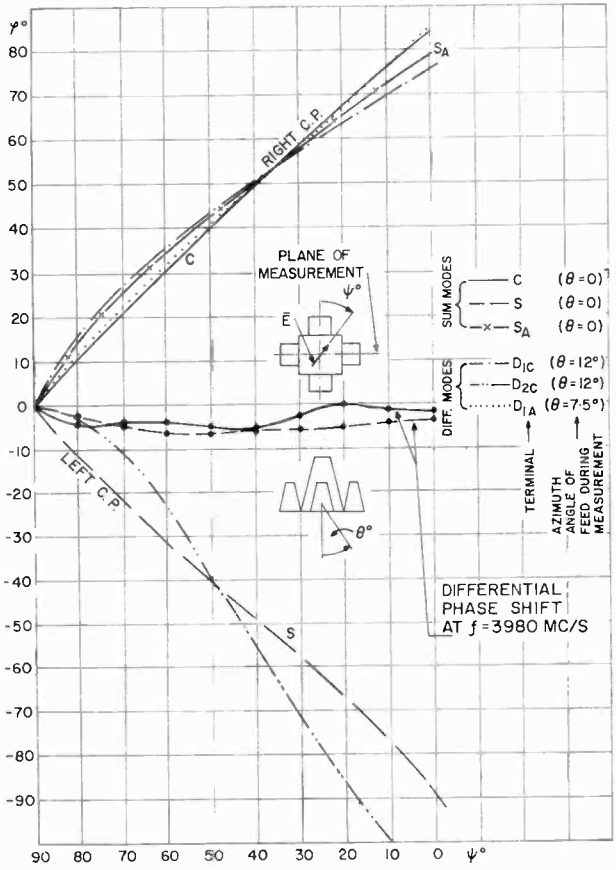

Fig. 16—Relative phase shift versus polarization angle for the different output terminals.

in many instances does not exceed the accuracy available from prediction based on primary characteristics.

In this section only two calculated characteristics of the secondary pattern are included, namely, the antenna efficiency (gain) as a function of frequency (see Table IV) and the noise temperature as a function of elevation angle (Figure 17).

The antenna efficiency is the most general and important characteristic of the antenna, and is defined as follows: *the antenna efficiency η for the B terminal is the magnitude of the transfer function between the basic waveguide mode in aperture B and the unipolarized plane wave with constant amplitude and zero phase in aperture C.* Here, aperture C is defined as a circular aperture with a nominal diameter

Table IV—Summary of Efficiency Factors and Gain of the Antenna (db)

Frequency (gigacycles)	$-\eta_R$	$-\eta_L$	$-\eta_{SH}$	$-\eta_{SP}$	$-\eta_M$	$-\eta_A$	$-\eta_{PF}$	$-\eta_{PR}$	$-\eta_B$	$-\eta$	G
3.8	.100	.400	.993	.116	.172	.302	.052	.048	.153	2.336	57.92
3.9	.040	.243	.880	.100	.052	.287	.063	.058	.153	1.876	58.61
4.0	.040	.242	.768	.084	.031	.266	.074	.071	.153	1.729	58.98
4.1	.021	.240	.757	.068	.058	.306	.095	.090	.153	1.788	59.13
4.2	.040	.256	.639	.052	.101	.370	.119	.112	.153	1.842	59.28
										Av = 1.869	58.82
5.9	.100	.320	1.656	.100	.237	.405	.125	.140	.158	3.241	60.85
6.0	.020	.320	1.333	.040	.424	.317	.136	.145	.158	2.893	61.24
6.1	.020	.314	.797	.025	.611	.887	.215	.150	.158	3.178	61.19
6.2	.020	.320	.622	.020	.828	1.005	.275	.155	.158	3.403	61.15
6.3	.060	.326	.557	.015	.611	.983	.330	.160	.158	3.201	61.46
6.4	.042	.360	.745	.020	.612	1.075	.380	.165	.158	3.556	61.23
										Av = 3.286	61.15

Note: The above figures are calculated for the linearly polarized operational mode, with an average orientation of polarization. For circular polarization the resultant gain is practically identical. The accuracy of gain figure for the receiver frequency band is better than .25 db; for the transmitter frequency band, it is better than .35 db. $\eta_{SH} + \eta_{SP} = \eta_S$, where η_{SH} and η_{SP} are the efficiencies corresponding to spillover radiation around the hyperboloid and paraboloid reflectors, respectively.

of 85 feet. This aperture is perpendicular to the axis of the ideal boresight direction and the antenna and is centrally positioned in the focal plane of the paraboloid. The above definition of C includes the effect of the various blockages, as well as losses in the waveguide circuit. It is assumed that aperture C is in free space, i.e., no effects of the radome, ground, building, etc., are included.

The terminal B can be either a sum or difference mode input terminal.

Only the efficiency of the communication channel is considered here. The restriction of unipolarization in aperture C is not substantial, because any elliptically polarized incoming wave can be expressed in terms of linearly polarized orthogonal components.

The accurate expression for η is fairly complicated, but, for most practical purposes, the following approximation is adequate:

$$\eta = \eta_R \eta_L \eta_S \eta_M \eta_A \eta_P \eta_B,$$

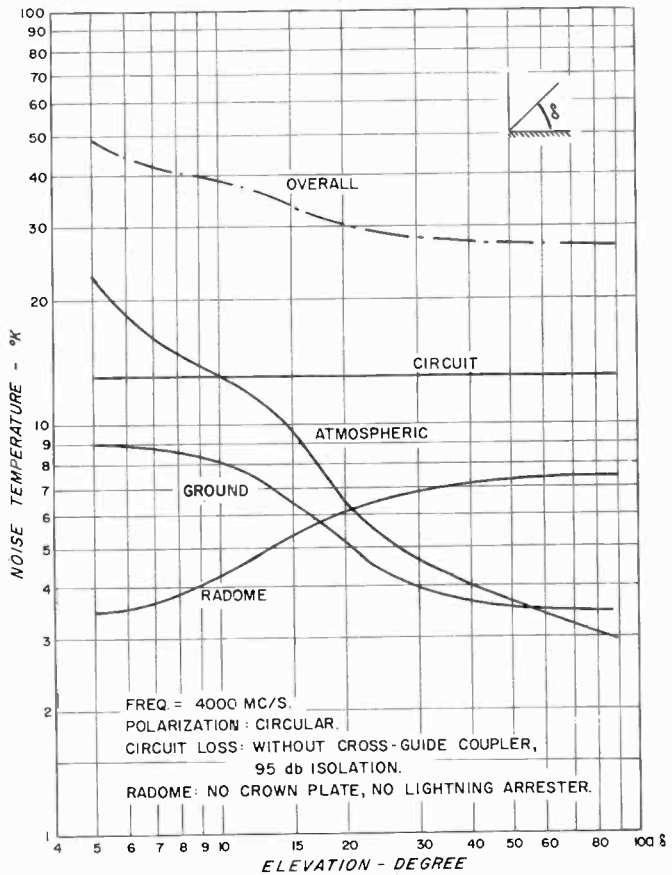

Fig. 17—Noise temperature of the antenna versus elevation angles (components and overall system).

where η_R is the reflection loss at the terminal B,

η_L is the insertion loss between terminal B and C,

η_S is the spillover efficiency, defined as the ratio of the main polarized power intercepted by the paraboloid to the main polarized power in the aperture of the source, assuming a perfectly transparent hyperboloid and supporting quadrupod,

η_M is the main polarized power efficiency, defined as the ratio of main polarized power radiated by aperture C relative to the total power radiated by the same aperture,

η_A is the amplitude (or illumination taper) efficiency, which takes into account the nonuniform-field amplitude distribution of the antenna in the plane C,

η_P is the phase-distribution efficiency, which takes into account the nonuniform-field phase distribution of the antenna in plane C,

η_B is the blockage factor, which takes into account the incomplete utilization of the aperture C.

These factors are determined by a method that utilizes the measured source patterns, loss, and isolation data. The details of this method were worked out by two of the authors (Foldes and Komlos). Table IV gives the individual contributory efficiencies and the overall efficiency in —db, i.e., the given db figure must be deducted from the theoretical gain figure of an ideal antenna with identical aperture size. Because of the multimode properties of the feed system, the η_S and η_A efficiencies vary irregularly, as reflected in the gain figures indicated.

Figure 17 shows the noise temperature of the antenna system versus elevation agle. This figure assumes a Hypalon-coated Dacron radome with a diameter of 120 feet and a wall thickness of 0.055 inch, the terrain existing at the site, spillover radiation characteristics of the feed system, the atmospheric losses, and the internal losses given in Table I. In calculation of noise temperature, the attenuating effect of the feed losses against external noise-temperature sources was included.

Conclusions

On the basis of measured primary characteristics the following main conclusions can be obtained:

(a) It is possible to control the aperture distribution of a primary source, through the use of higher order modes, in such a way that an approximately —2 db antenna efficiency can be maintained in the large portion of the 500-megacycle receiver frequency band of communication satellite systems.

(b) The relative complexity necessary for mode control and operational flexibility does not exclude the possibility of low internal loss figures.

(c) The resultant system has a high gain/noise-temperature ratio with a relatively simple, conventional paraboloid reflector, but accurate

fabrication techniques and sophisticated measuring methods are necessary to produce the feed itself. The penalty of the more complicated feed is more than offset by increased simplicity of the overall antenna system.

ACKNOWLEDGMENTS

The work reported here was performed for the Canadian Department of Transport, whose interest and contractual support made possible the development of the new feed system. As in any large scale team work, it is virtually impossible to acknowledge everyone who contributed either by criticism or by direct work to the success of this work. Nevertheless, the authors wish to express their thanks to all in the Department of Transport and in the Antenna Group of RCA Victor Company, Ltd., whose contribution meant the difference between success and failure. Particular credit should be given to E. Morris, R. Desrochers, H. Schwarz, and K. Flood, who performed many of the individual design tasks.

HIGH-EFFICIENCY, HIGH-ORDER, IDLER-LESS FREQUENCY MULTIPLIERS USING HYPERABRUPT VARACTORS

By

E. Markard and S. Yuan

RCA Communications Systems Division
New York, N. Y.

Summary—*Expressions for the efficiency and power-handling capability of high-order, idler-less frequency multipliers as functions of the nonlinearity coefficient are developed. It is shown that the efficiency of such multipliers can be increased substantially if the varactors possess a high nonlinearity coefficient, γ, i.e., hyperabrupt junction. Since it is a reactive device with a large reverse breakdown voltage, the hyperabrupt varactor can convert a large amount of power at microwave frequencies. Input power in excess of one watt can easily be handled, since hyperabrupt varactors having a reverse breakdown voltage of 75 volts are presently available.*

An experimental times-eight idler-less multiplier using a hyperabrupt varactor (with $\gamma = 0.875$) multiplying from 500 to 4000 megacycles gave an efficiency of 25% including passive circuit losses. The tuning is extremely simple, since the circuit involves only input frequency and output frequency loops. It has also been demonstrated that this multiplier is able to accept wide ranges of drive power without retuning.

Introduction

THE efficiency and power-handling capability of varactor frequency multipliers are highly dependent upon the nonlinearity coefficient of the capacitance (or elastance) variation. For a graded or an abrupt-junction diode, the efficiency drops off very rapidly as the order of multiplication is increased if no idlers are provided. It is desirable to avoid the use of idlers, since they add to the complexity of the multiplier circuit and can make tuning quite difficult. In order to accomplish high-order efficient multiplication without the use of idlers, varactors with high nonlinearities are required. Such varactors are referred to as being hyperabrupt. Until very recently hyperabrupt varactors were available only in very small quantities as engineering samples. Now, however, they are becoming available as standard products.

At the present time, it appears that when varactor junctions are made hyperabrupt, it is done at the expense of cutoff frequency.[1]

[1] J. J. Chang, J. H. Foster and R. M. Ryder, "Semiconductor Junction Varactors with High Voltage-Sensitivity," I.E.E.E. Trans. on Electron Devices, Vol. ED-10, p. 281, July 1963.

However, as γ increases, there is a net increase in the conversion resistance in spite of the effect of the degraded cutoff frequency. Hence, although for low-order multipliers (doublers and triplers) hyperabrupt varactors have no particular advantage over abrupt varactors, they do offer definite advantages when the case of high-order multiplication without idlers is considered.

In this analysis, an expression for the efficiency of a high-order multiplier without idlers as a function of the nonlinearity coefficient is developed. The analysis is carried out in general terms, except where a specific example is introduced to simplify the mathematics involved. In particular, the efficiency of a times-eight multiplier employing a varactor that has a nonlinearity coefficient $\gamma = 0.875$ is optimized.

Fundamental Voltage–Charge Relationship

The general expression for the elastance–voltage relationship for a varactor diode is

$$S = S_m \left(\frac{V_C + V}{V_C + V_B} \right)^{\gamma} \tag{1}$$

where

S is the elastance (reciprocal capacitance) of the reverse biased diode;

V is the applied reverse voltage, which is opposite in sign to the built-in contact potential, V_C, across the junction over most of the operating range;

V_C is the contact potential, and is in the order of a fraction of a volt;

V_B is the breakdown voltage of the varactor diode;

γ is the nonlinearity coefficient of the varactor diode;

$S_m (= S_{\max})$ is the elastance of the reverse-biased diode at breakdown voltage.

Figure 1 shows a plot of normalized elastance as a function of normalized voltage.

The elastance is also given by the slope of the voltage–charge curve,

$$S = \frac{1}{C} = \frac{dV}{dQ}. \tag{2}$$

Charge as a function of voltage can be derived by combining Equations (1) and (2);

$$dQ = \frac{(V_C + V_B)^\gamma}{S_m} \frac{dV}{(V_C + V)^\gamma}. \tag{3}$$

Integrating Equation (3),

$$Q = \frac{(V_C + V_B)^\gamma}{(1-\gamma)S_m} (V_C + V)^{1-\gamma} + K, \tag{4}$$

where K is the constant of integration; γ, of course, must not be unity.

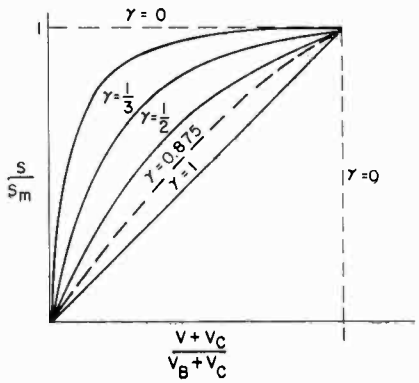

Fig. 1—Normalized elastance as a function of normalized voltage.

When the applied voltage, V, just cancels the contact potential, so that $V_C + V = 0$, K equals the charge on the junction, $-Q_c$. Thus,

$$Q_c + Q = \frac{(V_C + V_B)^\gamma}{(1-\gamma)S_m} (V_C + V)^{1-\gamma}, \tag{5}$$

where

$$Q_c = \frac{V_C{}^{1-\gamma}}{(1-\gamma)S_m} (V_C + V_B)^\gamma. \tag{6}$$

The maximum charge the junction will support, Q_m, occurs at the breakdown voltage, V_B, and, from Equation (5), is

$$Q_c + Q_m = \frac{(V_C + V_B)}{(1-\gamma)S_m}. \tag{7}$$

Substituting Equation (7) into Equation (5),

$$Q_c + Q = (Q_c + Q_m)\left(\frac{V_C + V}{V_C + V_B}\right)^{1-\gamma}. \tag{8}$$

Equation (8) can be rewritten

$$\frac{V_C + V}{V_C + V_B} = \left(\frac{Q_c + Q}{Q_c + Q_m}\right)^{1/(1-\gamma)}. \tag{9}$$

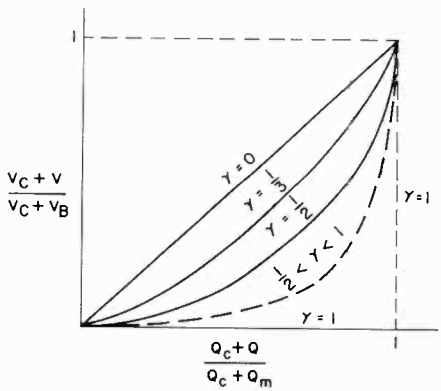

Fig. 2—Normalized voltage as a function of normalized charge.

Figure 2 is a plot of normalized voltage as a function of normalized charge. As γ approaches zero, the voltage–charge curve approaches a straight line, and the diode capacitance becomes constant. As γ increases from zero toward unity, the capacitance deviates more severely from linearity. Since $Q_c + Q_m$ is a function of γ, as expressed by Equation (7), the maximum charge the junction can support increases as γ increases. Therefore, it should be noted that the normalizing factor in Figure 2 is a function of γ. Referring to Equation (7), for an abrupt-junction diode ($\gamma = 1/2$),

$$Q_c + Q_m = \frac{2(V_C + V_B)}{S_m}; \tag{10}$$

and, for a graded-junction diode ($\gamma = 1/3$),

$$Q_c + Q_m = \frac{3}{2} \frac{(V_C + V_B)}{S_m}. \tag{11}$$

The normalized diode voltage, $(V_C + V)/(V_C + V_B)$, can be plotted as a function of charge normalized to $Q_c + Q_m$ for the abrupt junction, as shown in Figure 3.

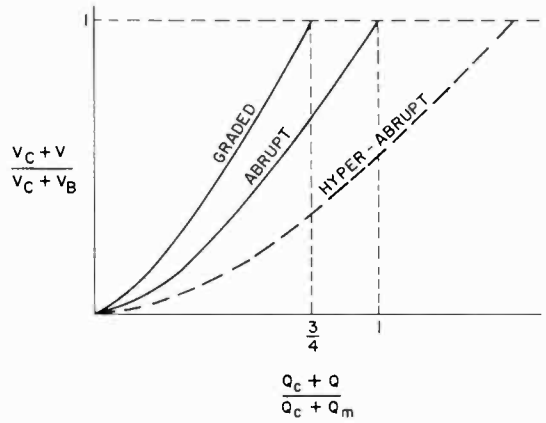

Fig. 3—Normalized voltage as a function of charge normalized to the maximum charge of an abrupt junction.

Since the instantaneous power is the product of voltage and current, and current is the time derivative of the charge, it is obvious that the peak currents and, therefore, the peak power, must be higher for larger γ.

Taylor-Series Representation

The voltage–charge relationship can be represented by a Taylor series expansion about a quiescent point, q_0, with a time-varying component, q, such that

$$Q = q_0 + q. \tag{12}$$

The pertinent Taylor expansion is

$$f(q_0 + q) = f(q_0) + f^{(1)}(q_0)\, q + \frac{f^{(2)}(q_0)}{2!} q^2 + \cdots + \frac{1}{n!} f^{(n)}(q_0)\, q^n, \tag{13}$$

where $f^{(n)}(q_0)$ is the n^{th} derivative evaluated at the bias point, q_0. Rearranging Equation (8),

$$f(q+q_0) = f(Q) = V + V_c = S_m(1-\gamma)\frac{(Q_c+Q)^{1/(1-\gamma)}}{(Q_c+Q_m)^{\gamma/(1-\gamma)}}. \tag{14}$$

Evaluating $f^{(n)}(q_0)$ from Equation (14), and setting $q_0 = \frac{1}{2}(Q_m - Q_c)$, the Taylor series expansion for the generalized nonlinearity becomes

$$V + V_c = \frac{Q_c+Q_m}{2(\Gamma+1)}S_0 + S_0 q + \frac{\Gamma}{(Q_c+Q_m)}S_0 q^2 + \frac{4\Gamma(\Gamma-1)}{6(Q_c+Q_m)^2}S_0 q^3 + \cdots\cdots + \frac{2^{n-1}}{n!}\frac{\Gamma!}{(\Gamma-n+1)!(Q_c+Q_m)^{n-1}}S_0 q^n, \tag{15}$$

where $$\Gamma = \frac{\gamma}{1-\gamma}, \tag{16}$$

and $$S_0 = f^{(1)}(q_0) = \frac{S_m}{2\Gamma}. \tag{17}$$

The corresponding series for the elastance, S, is obtained by differentiating Equation (15):

$$S = S_0 + 2\Gamma S_0\frac{q}{(Q_c+Q_m)} + 2\Gamma(\Gamma-1)S_0\left(\frac{q}{Q_c+Q_m}\right)^2 + \cdots + \frac{2^{(n-1)}}{(n-1)!}\left[\frac{\Gamma!}{(\Gamma-n+1)!}\right]S_0\left(\frac{q}{Q_c+Q_m}\right)^{n-1}. \tag{18}$$

CURRENT-PUMPED,* TWO-FREQUENCY DIRECT N-TIMES MULTIPLIER

Current pumping means that the diode elastance is made to vary in time by controlling the current through and, hence, the charge on, the junction. Current, or the integral of current, charge, then is the independent variable, while the voltage produced across the diode terminals by the current is the dependent variable.

In a current-pumped two-frequency direct N-times multiplier, only

* The current pumping method of operation was brought to our attention by M. E. Malchow of RCA.

currents at the input frequency, ω, and the output frequency, $N\omega$, are allowed to flow. Currents at all other frequencies are assumed to be open circuited by filters. Therefore, the current flowing through the diode is

$$i(t) = i_1(t) + i_N(t) = \frac{1}{2}\left[i_1 e^{j\omega t} + i_1^* e^{-j\omega t} + i_N e^{jN\omega t} + i_N^* e^{-jN\omega t}\right] = I_1 \cos(\omega t + \theta) + I_N \cos(N\omega t + \phi). \tag{19}$$

For convenience we define

$$m_N = \frac{|i_N|}{N\omega(Q_c + Q_m)}, \quad (N = \text{any integer}) \tag{20}$$

$$M_N = m_N e^{j\phi}, \tag{21}$$

$$M_N^* = m_N e^{-j\phi}. \tag{22}$$

In general, $V_c \ll V$, and by including the effects of the spreading resistance, R_s, the diode terminal voltage becomes, from Equation (15),

$$V_T(t) = \frac{Q_c + Q_m}{2(1+\Gamma)} S_0 + R_s i(t) + S_0\left[\int i(t)\,dt\right] + \frac{\Gamma}{(Q_c + Q_m)} S_0\left[\int i(t)\,dt\right]^2 + \cdots + \frac{2^{n-1}}{n!} \frac{\Gamma!}{(\Gamma - n + 1)!\,(Q_c + Q_m)^{n-1}} S_0\left[\int i(t)\,dt\right]^n. \tag{23}$$

All equations derived up to this point are exact and general. In order to make the mathematical development tenable, a specific example will be given to illustrate the procedure for calculating the multiplier efficiency.

Calculation of N-Times Multiplier Efficiency

The general procedure is as follows:

(1) Substitute Equation (19) into Equation (23).

(2) Extract the coefficients of all terms involving the frequencies ω and $N\omega$ for the voltages across the varactor terminals at the respective frequencies.

(3) Add the external circuit and derive the matrix equation that describes the operation of the circuit.

(4) Derive the equation for efficiency as a function of the load resistance and drive level.

(5) Optimize the efficiency as a function of load resistance and drive level.

The above procedure will be demonstrated for an eight times multiplier. The current flowing through the diode is

$$i(t) = I_1 \cos(\omega t + \theta) + I_8 \cos(8\omega t + \phi), \tag{24}$$

and the charge is

$$q = \int i(t)\,dt = \frac{I_1}{\omega} \sin(\omega t + \theta) + \frac{I_8}{8\omega} \sin(8\omega t + \phi). \tag{25}$$

Substituting Equations (24) and (25) into (23), and for convenience letting $U = I_1 \sin(\omega t + \theta) + (I_8/8) \sin(8\omega t + \phi)$

$$V_T(t) = \frac{Q_c + Q_m}{2(1+\Gamma)} S_0 + R_s \left[I_1 \cos(\omega t + \theta) + \frac{I_8}{8} \cos(8\omega t + \phi) \right]$$

$$+ \frac{S_0}{\omega} U + \frac{\Gamma}{\omega(Q_c + Q_m)} \frac{S_0}{\omega} U^2 + \frac{4\Gamma(\Gamma-1)}{6[\omega(Q_c+Q_m)]^2} \frac{S_0}{\omega} U^3 + \cdots\cdots$$

$$+ \frac{2^{n-1}}{n!} \frac{\Gamma!}{(\Gamma - n + 1)![\omega(Q_c+Q_m)]^{n-1}} \frac{S_0}{\omega} U^n. \tag{26}$$

To simplify the analysis further, assume $\gamma = 0.875$. From Equation (15), $\Gamma = 7$. Note that by choosing $\gamma = 0.875$ ($\Gamma = 7$), Equation (26) terminates at $n = 8$, since for $n \geq 9$ the coefficients become zero. Equation (26) becomes

$$V_T(t) = \frac{Q_c + Q_m}{16} + R_s[I_1 \cos(\omega t + \theta) + \frac{I_8}{8} \cos(8\omega t + \phi)] + \frac{S_0}{\omega} U +$$

$$+\frac{7}{\omega(Q_c+Q_m)}\frac{S_0}{\omega}U^2+\frac{28}{[\omega(Q_c+Q_m)]^2}\frac{S_0}{\omega}U^3$$
$$+\frac{70}{[\omega(Q_c+Q_m)]^3}\frac{S_0}{\omega}U^4+\frac{112}{[\omega(Q_c+Q_m)]^4}\frac{S_0}{\omega}U^5$$
$$+\frac{112}{[\omega(Q_c+Q_m)]^5}\frac{S_0}{\omega}U^6+\frac{64}{[\omega(Q_c+Q_m)]^6}\frac{S_0}{\omega}U^7$$
$$+\frac{16}{[\omega(Q_c+Q_m)]^7}\frac{S_0}{\omega}U^8. \tag{27}$$

Equation (27) is the relationship that specifies the terminal voltage across the varactor when the current, $i(t)=I_1\cos(\omega t+\theta)+I_8\cos(8\omega t+\phi)$, flows through it. Figure 4 shows the equivalent circuit representation of the varactor.

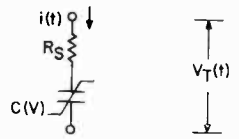

Fig. 4—Equivalent circuit of the varactor diode.

External Circuit Constraints

The terminal voltage as expressed by Equation (27) contains many frequency components. However, when the external circuits are introduced, the only voltage terms of importance in Equation (27) are at d-c, ω, and 8ω. The external circuit must have the required filters to present an open circuit to the undesired frequency components. Once the external circuit constraints are satisfied, operation of the multiplier is determined completely. The actual circuit that meets such requirements for an eight-times multiplier is shown in Figure 5.

Having specified the circuit, one can determine circuit performance by first determining the varactor terminal voltages at the fundamental frequency, ω, and the eighth harmonic, 8ω. These voltages are determined by collecting the coefficients of each frequency from Equation (27). Thus, for the fundamental frequency, ω,

$$v_1(t)=V_1\cos(\omega t+\alpha)=\frac{1}{2}(v_1e^{j\omega t}+v_1{}^*e^{-j\omega t})$$

$$= R_s I_1 \cos(\omega t + \theta) + \frac{S_0}{\omega} I_1 \sin(\omega t + \theta)$$

$$+ I_1 \sin(\omega t + \theta) \left\{ \left[\frac{3}{4} I_1^2 + \frac{3}{2} \left(\frac{I_8}{8} \right)^2 \right] \frac{28}{[\omega(Q_c + Q_m)]^2} \frac{S_0}{\omega} \right.$$

$$+ \left[\frac{5}{8} I_1^4 + \frac{15}{4} I_1^2 \left(\frac{I_8}{8} \right)^2 + \frac{15}{8} \left(\frac{I_8}{8} \right)^4 \right] \frac{112}{[\omega(Q_c + Q_m)]^4} \frac{S_0}{\omega}$$

$$+ \left[\frac{35}{64} I_1^6 + \frac{105}{16} I_1^4 \left(\frac{I_8}{8} \right)^2 + \frac{315}{32} I_1^2 \left(\frac{I_8}{8} \right)^4 \right.$$

$$\left. \left. + \frac{35}{16} \left(\frac{I_8}{8} \right)^6 \right] \frac{64}{[\omega(Q_c + Q_m)]^6} \frac{S_0}{\omega} \right\}$$

$$+ \frac{I_8}{8} \sin(8\omega t + \phi) \left[\frac{I_1^7}{8} \frac{e^{j(7\omega t + 7\theta)} - e^{-j(7\omega t + 7\theta)}}{2j} \right] \frac{16}{[\omega(Q_c + Q_m)]^7} \frac{S_0}{\omega}, \tag{28}$$

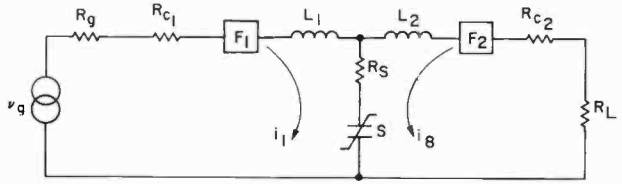

Fig. 5—Circuit configuration of an eight-times multiplier (F_1 and F_2 are bandpass filters that are short circuits at ω and at 8ω, respectively, and that are open circuits at all other frequencies).

where $$v_1 = |v_1| e^{j\alpha} = V_1 e^{j\alpha}. \tag{29}$$

Similarly, the voltage for the eighth harmonic, 8ω, is

$$v_8(t) = V_8 \cos(8\omega t + \beta) = \frac{1}{2} (v_8 e^{j8\omega t} + v_8^* e^{-j8\omega t})$$

$$= R_s I_8 \cos(8\omega t + \phi) + \frac{S_0}{\omega} \frac{I_8}{8} \sin(8\omega t + \phi)$$

$$+ \frac{I_8}{8} \sin(8\omega t + \phi) \left\{ \left[\frac{3}{2} I_1^2 + \frac{3}{4} \left(\frac{I_8}{8} \right)^2 \right] \frac{28}{[\omega(Q_c + Q_m)]^2} \frac{S_0}{\omega} + \right.$$

$$+\left[\frac{15}{8}I_1^4+\frac{15}{4}I_1^2\left(\frac{I_8}{8}\right)^2+\frac{5}{8}\left(\frac{I_8}{8}\right)^4\right]\frac{112}{[\omega(Q_c+Q_m)]^4}\left(\frac{S_0}{\omega}\right)$$

$$+\left[\frac{35}{16}I_1^6+\frac{315}{32}I_1^4\left(\frac{I_8}{8}\right)^2+\frac{105}{16}I_1^2\left(\frac{I_8}{8}\right)^4\right.$$

$$\left.+\frac{35}{64}\left(\frac{I_8}{8}\right)^6\right]\frac{64}{[\omega(Q_c+Q_m)]^6}\frac{S_0}{\omega}\Bigg\}$$

$$+I_1\sin(\omega t+\theta)\left[\frac{I_1^7}{64}\frac{e^{j7\omega t}-e^{-j7\omega t}}{2}\right]\frac{16}{[\omega(Q_c+Q_m)]^7}\frac{S_0}{\omega}, \tag{30}$$

where

$$v_8=|v_8|e^{j\beta}=V_8e^{j\beta}. \tag{31}$$

For a resonance condition, operation of the multiplier is characterized by the following matrix equation:

$$\begin{bmatrix} v_g \\ \\ 0 \end{bmatrix}=\begin{bmatrix} R_g+R_{c1}+R_s & \dfrac{M_1^{*7}}{8}\dfrac{S_0}{\omega} \\ -\dfrac{M_1^7}{8}\dfrac{S_0}{\omega} & R_s+R_{c2}+R_L \end{bmatrix}\begin{bmatrix} i_1 \\ \\ i_8 \end{bmatrix}$$

$$=\begin{bmatrix} R_{t1} & B \\ -C & R_{t2} \end{bmatrix}\begin{bmatrix} i_1 \\ i_8 \end{bmatrix} \tag{32}$$

where

$$R_{t1}=R_g+R_{c1}+R_s, \tag{33}$$

$$R_{t2}=R_s+R_{c2}+R_L, \tag{34}$$

$$B=\frac{M_1^{*7}}{8}\frac{S_0}{\omega}, \tag{35}$$

$$C=\frac{M_1^7}{8}\frac{S_0}{\omega}, \tag{36}$$

$$i_1=|i_1|e^{j\theta}=I_1e^{j\theta}, \tag{37}$$

$$i_8=|i_8|e^{j\theta}=I_8e^{j\theta}, \tag{38}$$

$$M_1^* = \frac{I_1}{\omega(Q_c + Q_m)} e^{-j\theta}, \tag{39}$$

$$M_1 = \frac{I_1}{\omega(Q_c + Q_m)} e^{j\theta}. \tag{40}$$

Solving the matrix equation for i_1 and i_8,

$$i_1 = v_g \frac{R_{t2}}{R_{t1}R_{t2} + BC}, \tag{41}$$

$$i_8 = v_g \frac{C}{R_{t1}R_{t2} + BC}. \tag{42}$$

Dividing Equation (42) by (41) gives the phase-angle relationship;

$$i_8 = i_1 \frac{C}{R_{t2}}, \tag{43}$$

$$|i_8| e^{j\phi} = |i_1| e^{j\theta} \frac{m_1{}^7 e^{j7\theta}}{8} \frac{S_0}{\omega}. \tag{44}$$

Thus, $\phi = 8\theta$, and

$$|i_8| = |i_1| \frac{m_1{}^7}{8} \frac{S_0}{\omega}. \tag{45}$$

The equivalent circuit at the fundamental frequency is shown in Figure 6. The input impedance is

$$\begin{aligned} Z_{in} &= \frac{v_g}{i_1} - R_g = R_{t1} + \frac{BC}{R_{t2}} - R_g \\ &= R_{t1} + R_0 - R_g = R_0 + R_{c1} + R_s \\ &= R_0 + R_1, \end{aligned} \tag{46}$$

where

$$R_0 = \frac{BC}{R_{t2}} = \frac{m_1{}^{14}}{64} \left(\frac{S_0}{\omega}\right)^2 \frac{1}{R_{t2}}, \tag{47}$$

and

$$R_1 = R_{c1} + R_s. \tag{48}$$

R_0 is the equivalent conversion resistance, since it is the resistance reflected into the input loop by the load resistance.

Efficiency Relationship

The power delivered to the load is

$$P_L = \frac{|i_s|^2 R_L}{2}. \tag{49}$$

The power available from the generator is

$$P_{AV} = \frac{|v_g|^2}{8R_g}. \tag{50}$$

Equation (50) assumes an input matched condition, so that

$$R_g = R_{in} = R_0 + R_1. \tag{51}$$

The efficiency, η, is defined as the ratio of the power in the load to the available power from the generator;

$$\begin{aligned}
\eta = \frac{P_L}{P_{AV}} &= \frac{|i_s|^2}{|v_g|^2} 4R_g R_L \\
&= \frac{4R_g R_0}{(R_{t1} + R_0)^2} \frac{R_L}{R_{t2}} \\
&= \frac{4R_g R_0}{(R_g + R_1 + R_0)^2} \frac{R_L}{R_{t2}} \\
&= \frac{4R_g(R_1 + R_0)}{(R_g + R_1 + R_0)^2} \frac{R_0}{R_0 + R_1} \frac{R_L}{R_{t2}}.
\end{aligned} \tag{52}$$

For input matched condition,

$$\eta = \frac{R_0}{R_0 + R_1} \frac{R_L}{R_L + R_2}$$

$$= \frac{1}{1+\frac{R_1}{R_0}} \frac{1}{1+\frac{R_2}{R_L}}, \tag{53}$$

where

$$R_2 = R_s + R_{c2}. \tag{54}$$

Efficiency Optimization

The condition for excitation may be determined by combining Equations (7) and (9);

$$V_c + V = (1-\gamma) S_m \frac{(Q_c+Q)^{1/(1-\gamma)}}{(Q_c+Q_m)^{\gamma/(1-\gamma)}}. \tag{55}$$

When the varactor is fully pumped, S/S_m reaches a maximum value of unity. Therefore, from Equation (2), with $\gamma = 0.875$,

$$\left[\frac{Q_c+Q}{Q_c+Q_m}\right]^{7} = 1, \quad \text{or} \quad \frac{Q_c+Q}{Q_c+Q_m} = 1. \tag{56}$$

Since $Q = q_0 + q$, and $q_0 = (Q_m - Q_c)/2$,

$$1 = \frac{1}{2} + m_1 \sin(\omega t + \theta) + m_8 \sin(8\omega t + \phi). \tag{57}$$

The optimum value of R_L is found by setting $d\eta/dR_L = 0$; then

$$R_L = \sqrt{\frac{R_2}{R_1}(K + R_1 R_2)}, \tag{58}$$

where

$$K = \frac{{m_1}^{14}}{64}\left(\frac{S_0}{\omega}\right)^2. \tag{59}$$

Here, m_1 was considered to be independent of R_L. While, strictly speaking, this may not be true, it can be shown to be a very good approximation for the idler-less, high-order multiplier.

Average Fundamental Input Power to an Idler-less, High-Order Frequency Multiplier

Considering the equivalent circuit at the fundamental frequency,

Figure 6, the generator voltage, $v_g(t)$, is related to the input current by the expression

$$v_g(t) = i_1(t)\ [R_g + R_{c1} + R_s + R_0]. \tag{60}$$

For a matched condition,

$$v_g(t) = 2i_1(t)\ [R_1 + R_0]. \tag{61}$$

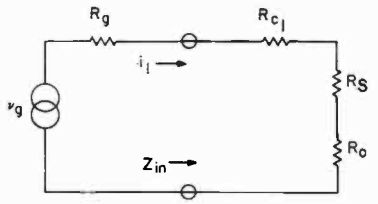

Fig. 6—Equivalent circuit at the fundamental frequency: R_0 = equivalent conversion resistance.

The instantaneous power input to the multiplier is given by

$$p_1(t) = \frac{1}{2} i_1(t) v_g(t), \tag{62}$$

or

$$p_1(t) = i_1^2(t)\ [R_1 + R_0]. \tag{63}$$

Since

$$i_1(t) = I_1 \cos(\omega t + \theta), \tag{64}$$

and using Equations (20) and (47), Equation (63) becomes

$$p_1(t) = \left\{ m_1^2 \omega^2 (Q_c + Q_m)^2 R_1 + \frac{m_1^{16}}{64} S_0^2 \frac{(Q_c + Q_m)^2}{R_2 + R_L} \right\} \cos^2(\omega t + \theta). \tag{65}$$

The average power is then

$$\langle P_1 \rangle = \frac{\omega}{2\pi} \int_{t=0}^{t=2\pi/\omega} p_1(t)\, dt, \tag{66}$$

or

$$\langle P_1 \rangle = \left\{ \frac{m_1^2}{2\pi} \omega^3 (Q_c + Q_m)^2 R_1 + \frac{m_1^{16}\omega}{128\pi} S_0^2 \frac{(Q_c + Q_m)^2}{R_2 + R_L} \right\} \int_0^{2\pi/\omega} \cos^2(\omega t + \theta)\, dt$$

$$= \frac{1}{2} \left\{ m_1^2 \omega^2 (Q_c + Q_m)^2 R_1 + \frac{m_1^{16}}{64} S_0^2 \frac{(Q_c + Q_m)^2}{R_2 + R_L} \right\} \qquad (67)$$

Using Equations (7), (16), (58), and (59)

$$\langle P_1 \rangle = \frac{1}{2} m_1^2 \omega^2 \frac{(V_C + V_B)^2}{S_m^2} [\Gamma + 1]^2 \left[R_1 + \frac{K}{R_2 + \sqrt{\frac{R_2}{R_1}(K + R_1 R_2)}} \right] \qquad (68)$$

"Regeneralization" of the Multiplier Equations

The effect of the nonlinearity coefficient, γ, on the efficiency and power-handling capability of the multiplier can be shown explicitly by reintroducing γ into the equations just derived. This will be done empirically, and the results will apply only to the eight times, idler-less multiplier using a varactor of arbitrary γ.

The variable R_L is a function of K (Equation (58)) and

$$R_0 = \frac{K}{R_2 + R_L}. \qquad (69)$$

However, K as defined by Equation (59) is for $\gamma = 0.875$. Consideration of Equations (26), (27), (28), (30), and (32) reveals that the factor 1/64 results from the coefficient of the eighth-order term in the general Taylor expansion, Equation (26). Hence,

$$\tilde{K} = \left[\frac{\Gamma(\Gamma - 1)(\Gamma - 2) \cdots (\Gamma - 6)}{8!} \right]^2 m_1^{14} \left(\frac{S_0}{\omega} \right)^2, \qquad (70)$$

where the tilde denotes a "regeneralized" term.

It should be noted here that if $\Gamma > 7$ ($\gamma > 0.875$), the Taylor series will not terminate in the eighth-order term, and there will be some contributions to the eighth harmonic from the additional terms. If these contributions should be too large to be neglected, then the equa-

tions for efficiency and power must be derived by taking these terms into account. However, for γ close to 0.875, these contributions are very small and, therefore, can be neglected.

Using the regeneralized $\tilde{K}$, one can rewrite the multiplier equations:

$$\tilde{R}_0 = \frac{\tilde{K}}{R_2 + \tilde{R}_L} = \left[\frac{\Gamma(\Gamma-1)(\Gamma-2)\cdots(\Gamma-6)}{8!} \right]^2 m_1{}^{14} \left(\frac{S_0}{\omega} \right)^2 \frac{1}{R_2 + \tilde{R}_L}, \tag{71}$$

and

$$\tilde{R}_L = \sqrt{\frac{R_2}{R_1}(\tilde{K} + R_1 R_2)} \tag{72}$$

or

$$\tilde{R}_0 = \frac{\tilde{K}}{R_2 + \sqrt{\frac{R_2}{R_1}(\tilde{K} + R_1 R_2)}}. \tag{73}$$

The efficiency then becomes

$$\tilde{\eta} = \frac{1}{\left(1 + \frac{R_2}{\tilde{R}_L}\right)} \frac{1}{\left(1 + \frac{R_1}{\tilde{R}_0}\right)}, \tag{74}$$

and the expression for the average fundamental input power becomes

$$<\tilde{P}_1> = \frac{1}{2} m_1{}^2 \omega \frac{(V_C + V_B)^2}{S_m{}^2} [\Gamma + 1]^2 \left\{ R_1 + \frac{\tilde{K}}{R_2 + \sqrt{\frac{R_2}{R_1}(\tilde{K} + R_1 R_2)}} \right\} \tag{75}$$

or

$$<\tilde{P}_1> = \frac{1}{2} m_1{}^2 \omega \frac{(V_C + V_B)^2}{S_m{}^2} [\Gamma + 1]^2 (R_1 + \tilde{R}_0). \tag{76}$$

Since R_1 and R_2 are, in practice, on the order of several ohms, R_1 and $R_2 > 1$, and $\tilde{R}_0$ and $\tilde{R}_L$ increase as $\tilde{K}$ increases. Therefore, the efficiency, $\tilde{\eta}$, and the maximum power input $<\tilde{P}_1>$ increase as $\tilde{K}$ increases. This, in turn, means that these quantities increase as γ increases toward unity. $\tilde{K}$ increases rapidly as $\gamma \to 1$; for example, $\Gamma = 49$ and $\tilde{K} = 6.25 \times 10^{10} m_1{}^{14} (S_0/\omega)^2$ when $\gamma = 0.98$.

Some Design Considerations

Practically speaking, in choosing a varactor for a given high-order multiplier application, several of the varactor parameters will be determined by what is available from diode manufacturers. The predetermined parameters, in general, will be:

(1) The nonlinearity coefficient, γ. The foregoing analysis indicates that the use of a varactor with γ as close to unity as possible gives maximum efficiency and maximum power-handling capability.

(2) The spreading resistance, R_s. R_s is determined by the materials used and the manufacturing process employed. One should choose a varactor with the lowest R_s for a given γ, since R_s is responsible for power loss. But, in general, a choice here will probably not be available.

(3) The cutoff frequency at an arbitrary low reverse voltage, $-V_s$ (generally -6 volts), $f_c\ (-V_s)$. This quantity is related to R_s by the relationship

$$f_c(-V_s) = \frac{1}{2\pi R_s C(-V_s)}, \tag{77}$$

which indicates that f_c should be chosen to be as large as is obtainable for minimum R_s.

(4) The contact potential, V_c. This parameter is determined by the materials used.

Once these parameters are known, the remaining two varactor parameters, namely the junction capacitance and the breakdown voltage, can be calculated:

(1) The junction capacitance at an arbitrary low reverse voltage, $-V_s$ (usually -6 volts), $C(-V_s)$. This parameter can be calculated from Equation (77).

(2) The required breakdown voltage, V_B, is calculated from Equation (76). If the multiplier circuit losses are neglected, the first term of Equation (76) represents the average power lost in the varactor spreading resistance. This represents the power dissipated by the varactor, and $<\tilde{P}_1>$ will be a maximum when the power lost in R_s equals the manufacturer's rated maximum dissipation. Hence,

$$<P_{\text{diss}}> = \frac{1}{2} m_1^2 \omega \frac{(V_C + V_B)^2}{S_m^2} [\Gamma + 1]^2 R_s. \tag{78}$$

All the terms in Equation (78) are known except S_m and V_B, which are

related by Equation (1),

$$S_m = \frac{1}{C(-V_s)}\left(\frac{V_C + V_B}{V_C + V_S}\right)^{(\Gamma+1)/2}. \tag{79}$$

Substituting into Equation (78), and rearranging terms,

$$V_B = \left[\frac{2 <P_{\text{diss}}>}{m_1^2\omega[C(-V_s)]^2(V_c + V_s)^{2\Gamma/(\Gamma+1)}(\Gamma+1)^2 R_s}\right]^{(\Gamma+1)/2} - V_c, \tag{80}$$

where, with reference to Equation (57) for the fully pumped case, $m_1 \doteq 1/2$.

One additional parameter, a circuit parameter, remains to be found —the optimum applied bias voltage. This is found by setting $Q = q_0 = (Q_m - Q_c)/2$ in Equation (5)

$$\frac{Q_c + Q_m}{2} = \frac{(V_c + V_B)^\gamma}{(1-\gamma)S_m}(V_C + V_0)^{1-\gamma}, \tag{81}$$

or

$$V_0 = \left[\frac{Q_c + Q_m}{2}\frac{(1-\gamma)S_m}{(V_c + V_B)^\gamma}\right]^{1/(1-\gamma)} - V_c, \tag{82}$$

where V_0 is the applied d-c bias voltage.

Numerical and Experimental Results

Figures 7 and 8 show the calculated efficiency of an eight-times multiplier as a function of γ for various values of the circuit parameters. The calculations were based on the following values:

$$S_0 = \frac{1}{1.0 \times 10^{-12}} f_d^{-1}$$

$f_c(-6 \text{ volts}) = 100$ gigacycles

$$R_s = \frac{10}{2\pi} = 1.59 \text{ ohms}$$

$$m_1 \leq \frac{1}{2}$$

$R_1 = R_2$

Input frequency = 500 megacycles.

An experimental eight-times idler-less multiplier employing a hyperabrupt varactor, having an input frequency of 500 megacycles, was constructed and tested. The hyperabrupt varactor used has the characteristics shown in Figure 9. An efficiency of 25% was obtained at an input power level of 250 milliwatts. Power output at 4 gigacycles was 62 milliwatts. It can be seen from Figures 7 and 8 that with the

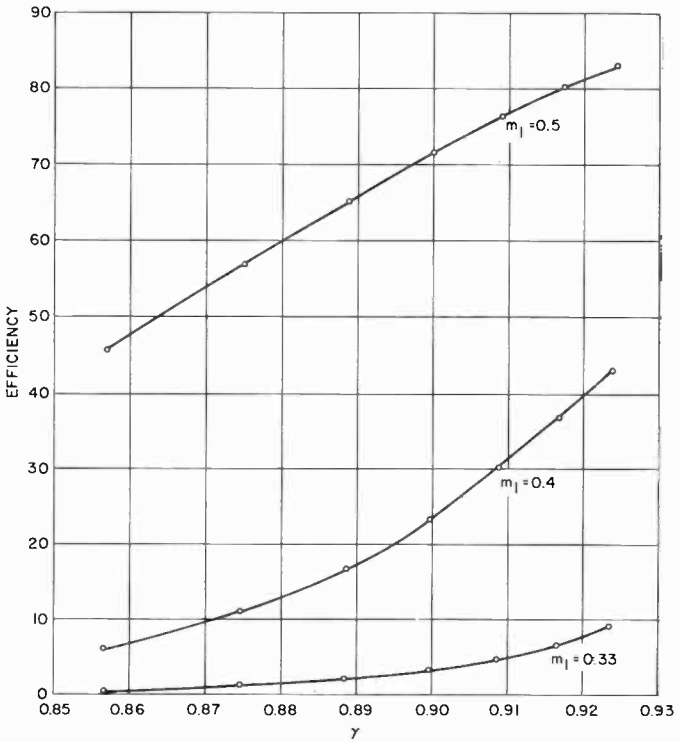

Fig. 7—Efficiency as a function of $\gamma (R_1 = R_2 = 5$ ohms).

proper nonlinearity coefficient and drive level, an efficiency of 55% is possible for an eight-times multiplier without idlers.

Power tests as well as efficiency tests have been performed on the hyperabrupt octupler. The power test was to determine the input power level at which diode burnout occurs. A relatively poor quality diode was chosen for this purpose. Hence, the efficiency obtainable was less than that for the better quality diodes.

For the efficiency test, the relatively good diode used has the following specifications:

$V_b = 25$ volts

$f_c(-6 \text{ volts}) = 105$ gigacycles

$C_j(-6 \text{ volts}) = 0.48$ pf.

For the power test, the above varactor was replaced by one having

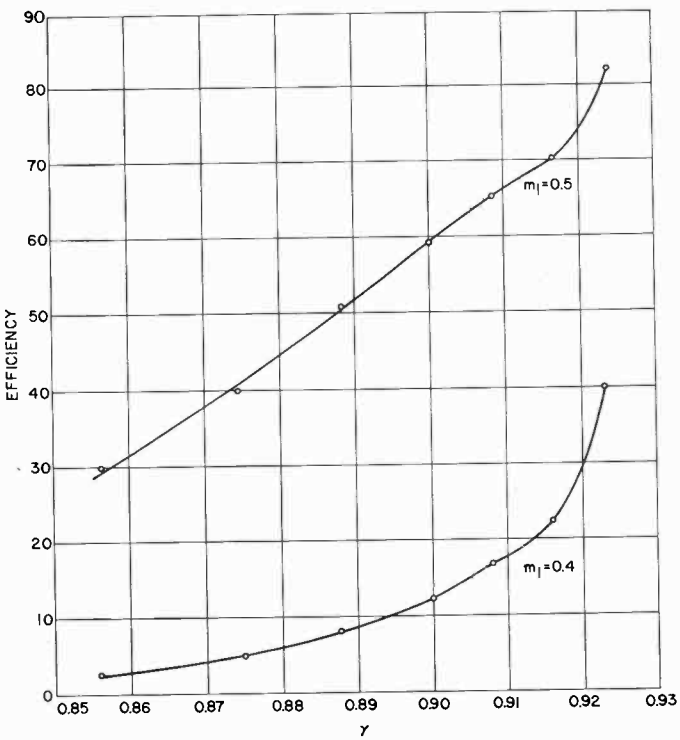

Fig. 8—Efficiency as a function of γ ($R_1 = R_2 = 8$ ohms).

the following specifications:

$V_b = 52$ volts

$f_c(-6 \text{ volts}) = 27$ gigacycles

$C_j(-6 \text{ volts}) = 1.3$ pf.

It was found that after replacing diodes, the multiplier efficiency was maximized without any retuning of the circuit other than a slight change in d-c bias, V_0. As the input power was increased from 250

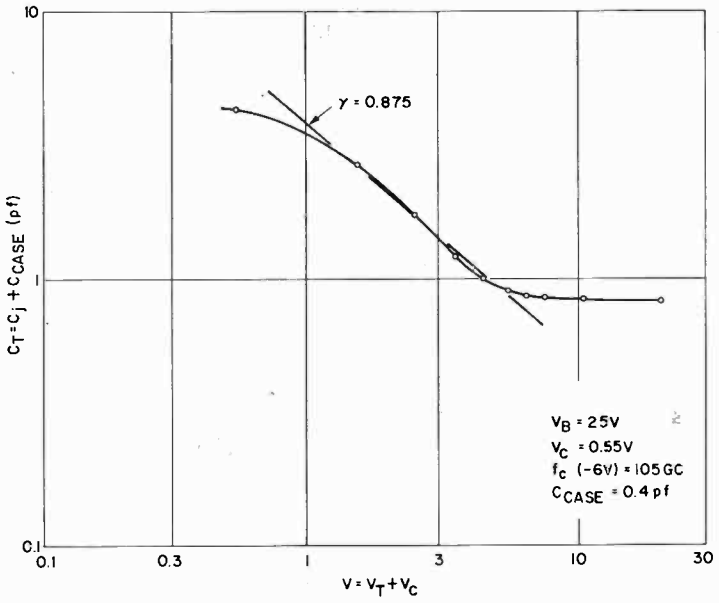

Fig. 9—Characteristics of hyperabrupt varactor used in experimental eight-times idler-less multiplier.

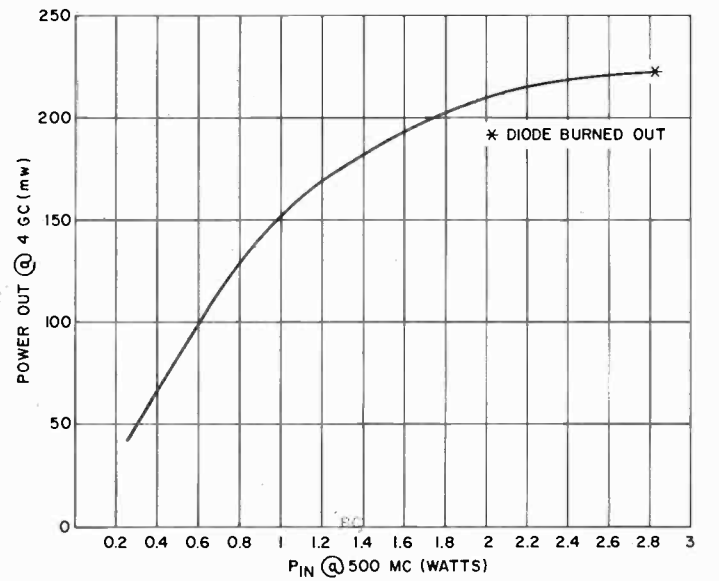

Fig. 10—Output power versus input power curve for experimental eight-times multiplier.

milliwatts, it was also found that to obtain maximum power output at each input power level, only the d-c bias had to be changed. The output power as a function of input power is plotted in Figure 10.

Conclusions

The generation of broadband or tunable microwave power can be achieved by high-order frequency multipliers with hyperabrupt varactors. High efficiency can be obtained without the use of idler circuits, thus simplifying the circuits considerably. Efficiencies as high as 55% can be achieved for a times-eight multiplier with an input frequency of 500 megacycles and an output frequency of 4 gigacycles if the diode nonlinearity, γ, is 0.875 over the entire range of operation and the diode is fully pumped. Experimental results have yielded a 25% efficiency with the diode nonlinearity, γ, of 0.875 over portions of the operating range. The input power-handling capability is in excess of 2.5 watts and the efficiency remains essentially constant over the range of input power of 0.2 to 1.0 watt. The tuning of the device is extremely simple since only the input circuit and the output circuit need be adjusted. Furthermore, the multiplier can be made broadband since there are no idlers to degrade its bandwidth.

The experimental results described in this paper were obtained using reasonably high-Q varactors. One of these units has a cutoff frequency of 105 gigacycles at —6 volts. While this value is below that of commonly available conventional varactors, it does not pose a serious limitation until the output frequency of the hyperabrupt multiplier is extended well into X-band. It is also not unlikely that further advances in hyperabrupt junction fabrication will yield still higher cutoff frequencies (or Q's).

To summarize, the use of a hyperabrupt varactor in frequency multipliers yields the following advantages:

(1) high efficiency for high order multiplication without the use of idlers,

(2) ease of tuning due to the simplicity of the circuit (only an input frequency loop and an output frequency loop are required),

(3) circuit simplicity makes broadbanding easier to achieve,

(4) higher power handling capability as compared to abrupt varactors with the same breakdown voltages,

(5) greater capability for handling wide variations in input power without requiring retuning.

Bibliography

P. Penfield, Jr., and R. P. Rafuse, *Varactor Applications*, The MIT Press, 1962.

T. C. Leonard, "Prediction of Power & Efficiency of Frequency Doublers Using Varactors Exhibiting a General Nonlinearity," *Proc. I.E.E.E.*, Vol. 51, p. 1135, Aug. 1963.

P. Canick and S. Yuan, "Γ-Dependence of Varactor Frequency Doublers," *Proc. IRE*, Correspondence, Vol. 50, p. 1533, June 1962.

J. J. Chang, J. H. Foster and R. M. Ryder, "Semiconductor Junction Varactors with High Voltage-Sensitivity," *I.E.E.E. Trans. on Electron Devices*, Vol. ED-10, No. 4, p. 281, July 1963.

PROJECT RANGER* TELEVISION SYSTEM

By

B. P. Miller

RCA Astro-Electronics Division
Princeton, N. J.

Summary—*The function of the ranger television system was to transmit close-up pictures of the lunar surface to earth. The philosophy, design, and performance of the television system are described. The television system consisted basically of six slow-scan vidicon cameras whose outputs were used to frequency-modulate two sixty-watt transmitters. The two signals, approximately one megacycle apart, were radiated by a high-gain parabolic antenna. The ground receiving station, located at Goldstone, California, used an 85-foot parabolic antenna. Several high-definition photographs of the lunar surface are included to provide a complete description of the performance of the system.*

Introduction

THE Ranger program, which was sponsored by the National Aeronautics and Space Administration (NASA), was the first of a series of projects, the eventual goal of which is to land a man on the moon. The specific purpose of Ranger was to obtain close-up pictures of the lunar surface in order to gain information regarding the surface conditions on the moon. The pictures obtained were to be at least an order of magnitude better in resolution than the best available by earth-based photography. Such information is an essential prerequisite for future projects involving "soft" landings.

The Ranger vehicles were designed to transmit television pictures of the lunar surface in the final few minutes before crashing into the moon. Three such vehicles were successfully flown; they were designated Ranger VII, VIII, and IX. More than 17,000 high-quality photographs of the lunar surface have been obtained from the three vehicles. The picture-taking phase of Ranger has now been completed; processing and interpretation of the information received will continue for some time.

The Spacecraft

The Ranger spacecraft, shown in Figure 2, consists of two major subassemblies—the television system and the spacecraft bus. The bus provides a space-stabilized vehicle for the television system. The total

* The Ranger Program was conducted for the National Aeronautics and Space Administration (NASA) by the Jet Propulsion Laboratory (JPL), California Institute of Technology. The Astro-Electronics Division of RCA was a major subcontractor to JPL, responsible for the design, fabrication and test of the TV System.

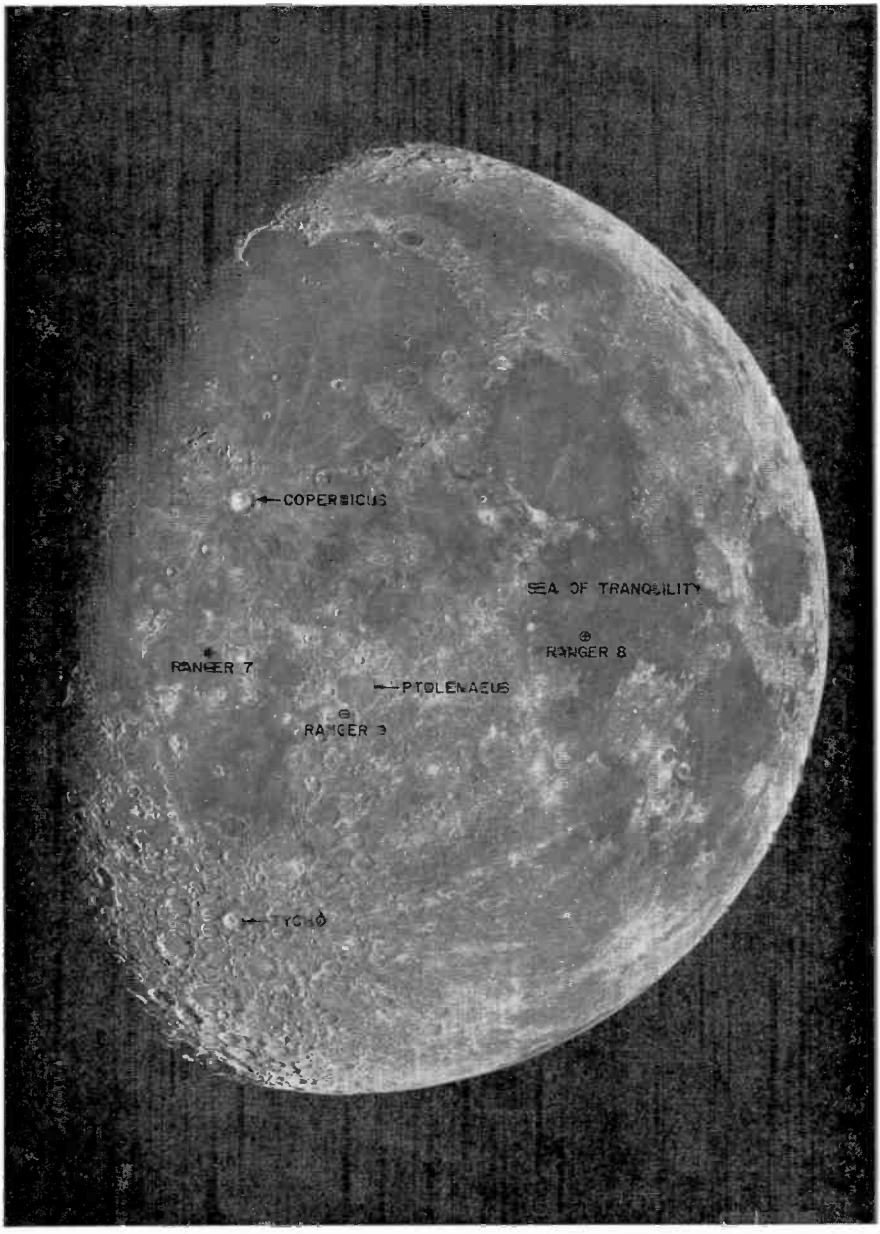

Fig. 1—Telescopic photograph of the moon taken from earth showing the impact points of Rangers VII, VIII, and IX.

spacecraft (bus and television system) weighs about 810 lb.; the weight of the television system is about 380 lb. The bus consists of several systems; these include the radio, data encoder, and command systems; the central computer and sequencer (CC&S) system; the attitude-control system; the power system; and the midcourse propul-

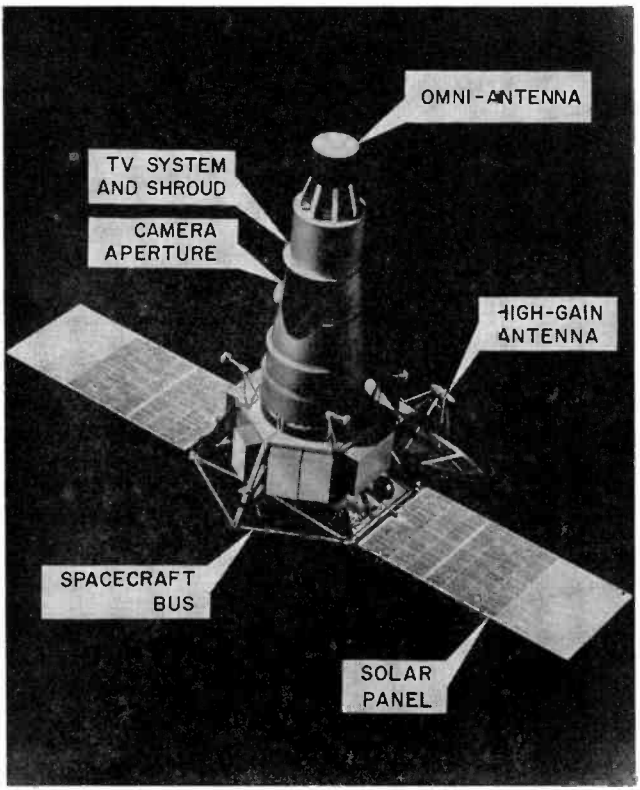

Fig. 2—Ranger spacecraft.

sion system. The power system, which derives its power from two solar panels when the spacecraft is oriented toward the sun and from batteries during other periods, supplies all the power required by the bus portion of the spacecraft. The attitude-control system provides for attitude stabilization during the major portion of the flight, so that the solar panels will be oriented toward the sun at the same time that the high-gain antenna of the radio system is pointed toward the earth. It also provides the capability for maneuvers to initially acquire the sun and the earth, to correct any trajectory errors during flight in

conjunction with the midcourse propulsion system, and to align the cameras of the television system in relation to the lunar surface prior to impacting the moon. The radio system is part of a two-way link between the earth and the spacecraft for transmission of telemetry from the data encoder system to earth, and to receive command information from earth to the spacecraft system. The high-gain antenna of the radio system is also used to transmit the processed signal outputs of the television system transmitters. The CC&S provides all of the on-board timing for the various spacecraft functions.

The Television System

The television system is the means by which the primary data-gathering function of the Ranger mission is performed. This self-contained unit provides the power, control, and communications equipment for collecting, processing, and transmitting the photographic information of the lunar surface. In a normal mission, the picture-taking sequence is initiated by an earth-generated command, with the first picture taken at an altitude of approximately 2000 kilometers from the lunar surface, and continues uninterrupted until lunar impact. The initial pictures cover a wide area of the moon at resolutions comparable to that obtained by earth-based telescopes. Area coverage is exchanged for increasing resolution as the spacecraft approaches impact at a terminal velocity of 2700 meters per second; resolutions of 0.5 meter, or better, are achieved in the final picture sequence.

The television system is separated into two essentially independent channels of operation to ensure a maximum probability of mission success. The channel arrangement is illustrated in Figure 3. Each channel has all of the components required to collect and process the video information and to supply a 60-watt frequency-modulated signal to the common high-gain antenna for transmission back to earth. Channel separation is on the basis of the two modes of camera operation employed—full scan and partial scan. There are two full-scan and four partial-scan cameras. Both types employ ruggedized vidicon pickup tubes with a highly sensitive photoconductive target. The basic difference between the two modes of camera operation is in the size of the area scanned on the vidicon target, and thus the time required to read out the stored image. Because of the high sensitivity of these vidicons and the image retention characteristic needed for slow-scan readout, special provision is made to erase the residual picture after frame readout and prior to a subsequent exposure so as to prevent a double image. To provide for maximum utilization of the communications equipment, multiple cameras, operating during each other's erase

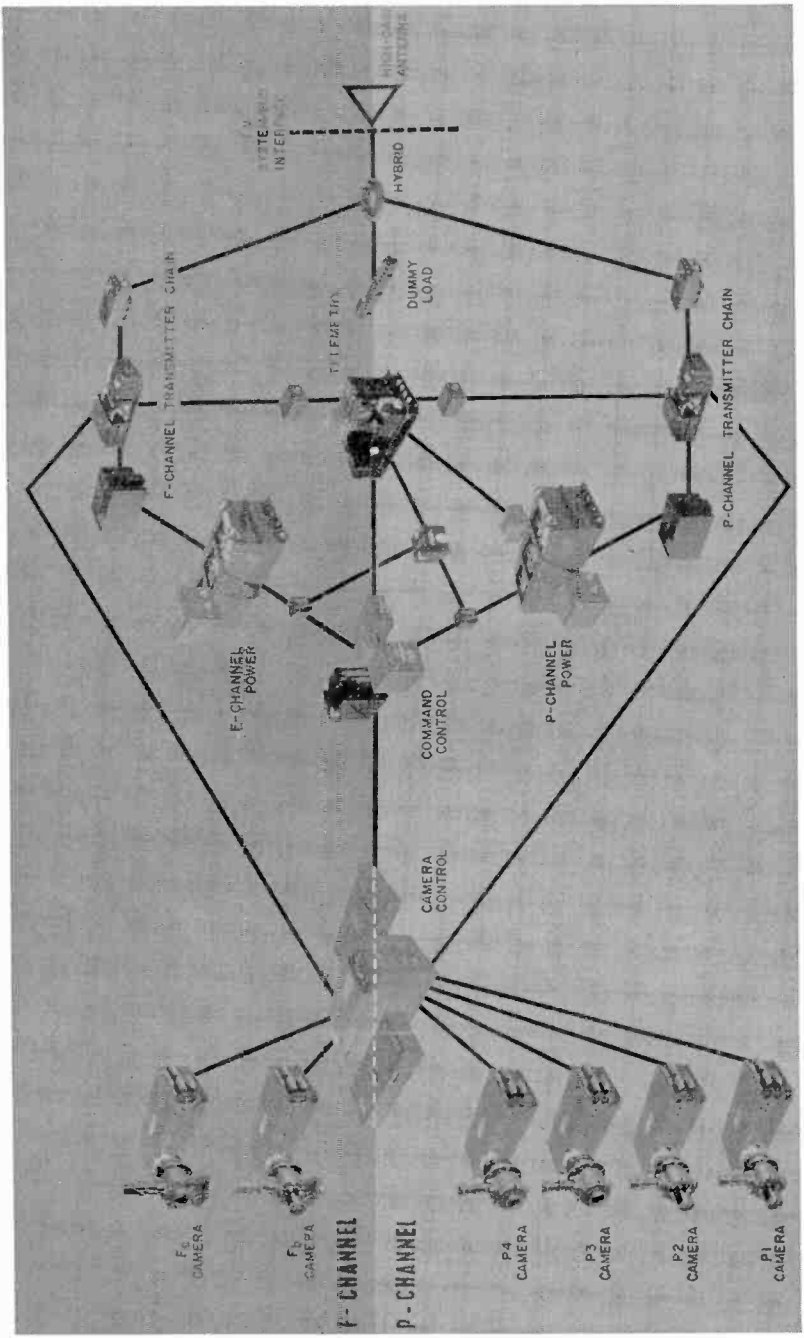

Fig. 3—Channel separation of the Ranger television system.

cycles, are used to fill out what would otherwise be nonproductive portions of the available transmission time.

In order to satisfy the requirements of high resolution, it was desirable that the final sequence of pictures be taken from a minimum altitude above the lunar surface. The minimum altitude for the final pictures is determined by the time required to read out the video data from the camera and by the spacecraft terminal velocity. Minimum altitude, and thus highest resolution with a given optical system and camera design, is therefore obtained by minimizing the camera readout time. However, the minimum readout time is also constrained by the number of scanning lines (or line density) required to provide the desired picture resolution, and the permissible system video bandwidth, which in this case was fixed at a maximum of 200 kc for each channel. In the Ranger television system, high line density and minimum readout time were achieved by the use of a special method of raster formation with a high-resolution, slow-scan vidicon camera tube. Minimum readout time is achieved in the four partial-scan cameras by scanning only the central 282 lines of a nominal 1125 line raster, enabling a 0.2-second frame time with a corresponding altitude of less than 600 meters for the exposure and transmission of the last complete frame. A set of four partial-scan cameras (designated P1, P2, P3, and P4) are exposed and read out sequentially at 0.2-second intervals to ensure continuous coverage until impact with the partial-scan channel, based on a complete picture cycle time (exposure, read, erase, and prepare) of 0.8 second for one camera.

The area of the vidicon target scanned in the partial-scan cameras measures 0.11 by 0.11 inch. The P1 and P2 cameras are equipped with 76-mm f/2.0, narrow-angle lenses to provide fields of view of 2.1 degrees, and the P3 and P4 cameras with 25 mm f/0.95, wide-angle lenses to provide fields of view of 6.3 degrees. The sequence of operation is P1, P3, P2, and P4, so that photographs are alternately taken by a narrow-angle lens and wide-angle lens. The combination of the optics, reduced scan area, and minimum readout time provides the capability to achieve a resolution of 0.5 meter per optical line pair in the final sequence of pictures.

The television system also contains two cameras that utilize the full 1125 line raster with a correspondingly longer readout time to provide coverage of wider areas of the lunar surface at a level of resolution that is sufficient to locate the data observed in the final high-resolution pictures. These cameras, designated F_a and F_b, are exposed and read out sequentially at 2.5-second intervals, and scan a 0.44-inch-square area. The F_a-camera is equipped with a 25-mm f/0.95, wide-

angle lens to provide a 25-degree field of view, while the F_b-camera has a 76-mm f/2.0, narrow-angle lens to provide an 8.4-degree field. One reason for having several cameras with different lens apertures is that prior to the flight of Ranger the lighting conditions on the moon could not be precisely determined from earth. The different lenses employed provide greater exposure latitude, allowing picture taking over a wide range of lighting conditions. The range of lunar lighting conditions covered by the lenses and the dynamic range of the vidicons was set for 30 to 2600 foot-lamberts during the flight of Ranger VII, which roughly corresponds to lighting conditions on earth (on an average day) from noon to dusk. On the basis of the Ranger VII flight data, the upper limit of the camera dynamic range corresponding to the peak video signal was reduced to 1600 foot-lamberts for Rangers VIII and IX. The full-scan cameras provide pictures with slightly different pointing vectors to achieve a partially overlapping pattern. The four partial-scan cameras are arranged with slightly divergent pointing angles to provide a series of photographs whose coverage will result in a nesting pattern around a common optical axis as shown in Figure 4. This figure shows the theoretical pointing angles and coverage for each of the six cameras. Prior to the launch, an accurate determination is made of the actual pointing angles and camera overlap so that the relation of each picture received from the spacecraft during the actual mission will be known. A special camera array alignment procedure was used for this purpose. The television system, with the cameras in flight configuration, was positioned with respect to a stationary target to within 1 minute of arc using an autocollimating theodolite. Pictures were taken of the target with each of the cameras, and the video signal was processed and displayed on a kinescope. The resultant image was then photographed with a 35-mm film camera and the film developed for viewing and analysis. The actual pointing angle for each camera was then obtained by measuring the reticle position and picture edge on the developed film with respect to markings on the target.

Each television camera employs a magnetically focused and deflected vidicon tube having a special photoconductive surface with excellent sensitivity, high retentivity, and good erasure characteristics. The sensitivity of the vidicon used in the Ranger cameras is similar to photographic film with an ASA rating of 5 to 20 (DIN of 8 to 14). Each vidicon is capable of supplying a signal current greater than 10 nanoamperes at an exposure of 0.3 foot-candle second. The peak-to-peak residual signal after erasure is less than 5 percent of the peak-to-peak signal before erasure. The light transfer characteristic (gamma) is shown in Figure 5 for typical Ranger cameras. A sample

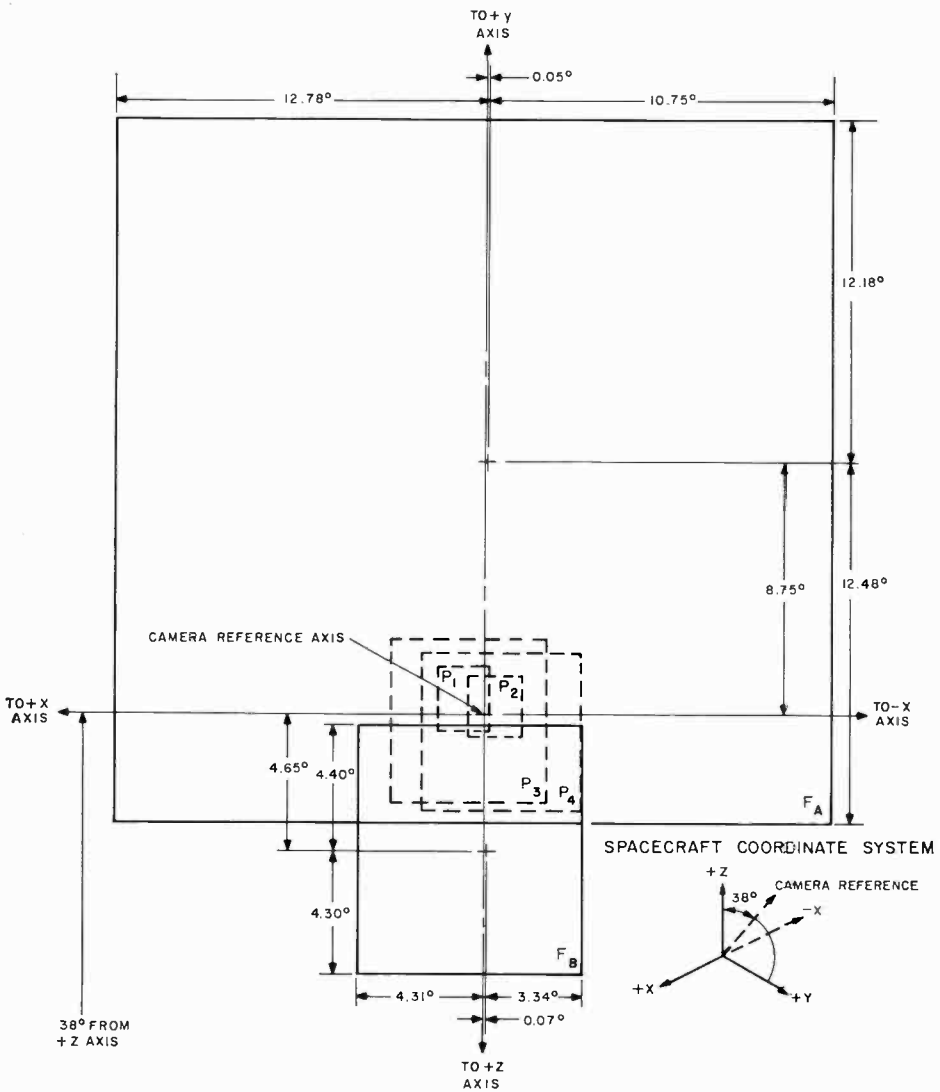

Fig. 4—Picture nesting pattern provided by the Ranger television cameras.

of the horizontal square-wave response curve for both a full-scan and a partial-scan camera is shown in Figure 6. The spectral response of the tube compared to the human eye is shown in Figure 7. In operation, the photoconductive surface is prepared for exposure by uniformly charging the surface with the electron scanning beam. Optical exposure modifies the stored charge in accordance with the photoconductive resistance changes induced by the image. The electron beam then

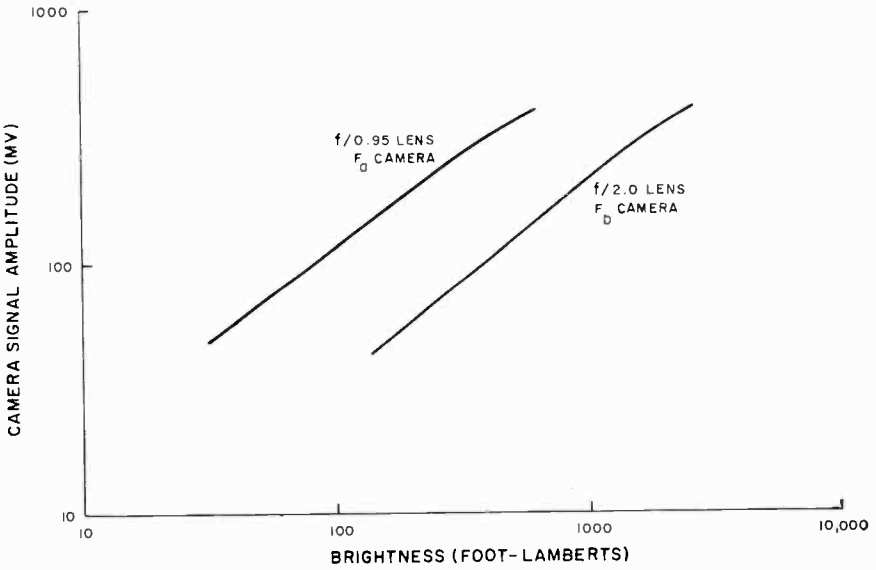

Fig. 5—Sample light transfer characteristics of Ranger cameras.

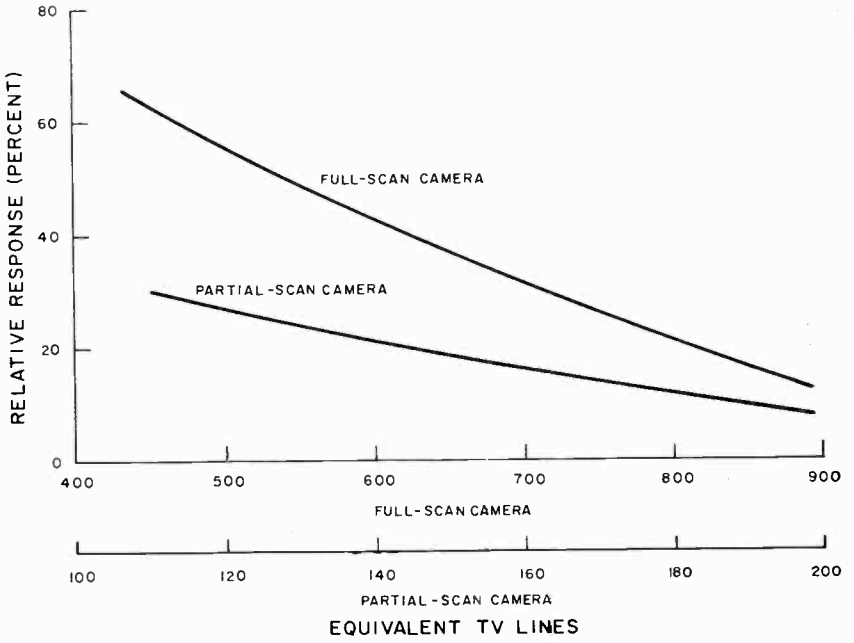

Fig. 6—Sample horizontal square wave response of Ranger cameras.

scans the surface. The video signal is dependent upon the discharge that occurs during exposure. After the picture has been read out, the target surface is erased to eliminate the residual image.

Each camera is provided with a metal focal-plane shutter. This shutter is a solenoid-operated, sliding-aperture type that moves from one side of the lens to the other each time a picture is taken. The moving blade is located as close to the focal plane as possible. The shutter is designed to provide the full-scan cameras with a 4-milli-

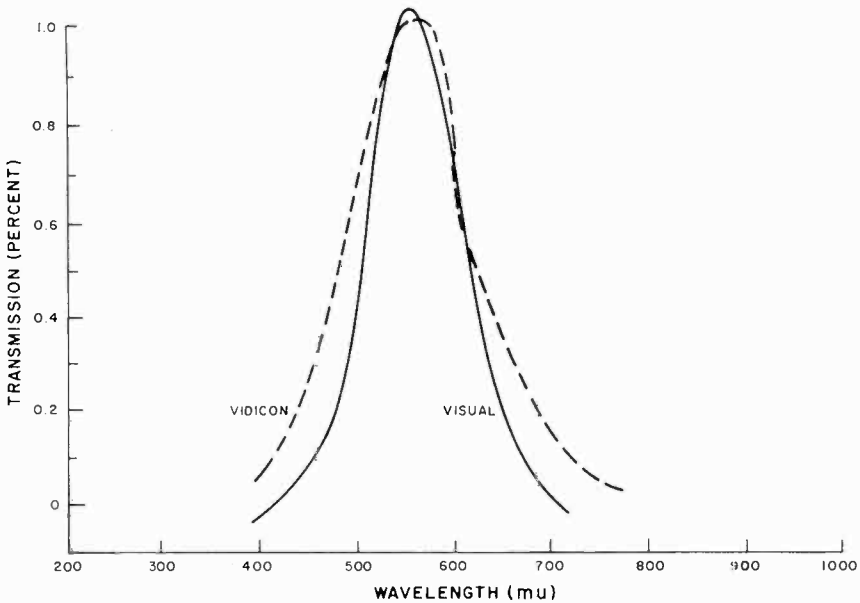

Fig. 7—Spectral response of Ranger vidicon compared to human eye.

second exposure and the P-cameras with an exposure of 2 milliseconds to minimize image motion. The faster sequencing of the P-cameras enables photographs from a much lower altitude than is possible with the F-cameras, so that image motion becomes a critical factor in terminal resolution. The shutter is a unique high-reliability design with a demonstrated capability of 1 million operations—many more than could possibly occur during the testing and flight of a Ranger spacecraft.

The F_a and F_b cameras along with their associated electronic circuits, sequencing circuits, video combiner, a control circuit, a power-distribution circuit and transmitter comprise the F-channel of the Ranger television system. The P-channel contains independent cir-

cuits, identical to the F-channel, to control, process, and transmit the video information obtained by the four partial-scan television cameras. In addition, the P-channel contains the secondary synchronizing and electronic circuits necessary to provide the P1 camera with the capability of a "free-running" mode of operation. This capability would permit the P1 camera to operate in the event of a failure of the P-channel sequencer and thus ensure that the high-resolution pictures would be obtained.

Each camera of the television system has an associated unit that amplifies the video signal from the vidicon and then feeds the signal to a video combiner for processing. The operating voltages, sweep signals, and focus signals for the vidicon and yoke assembly of the associated camera are all generated in this unit. A camera sequencer

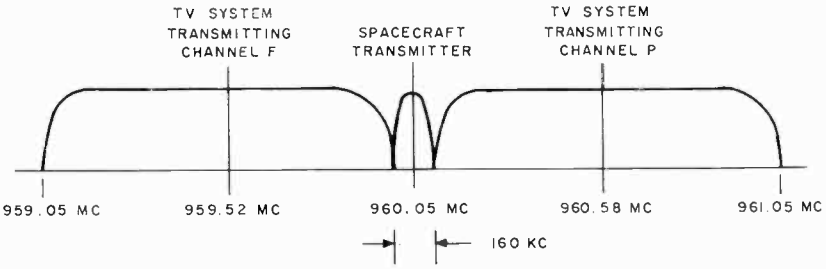

Fig. 8—Ranger spacecraft frequency allocations.

circuit in each channel provides the synchronizing and sequencing signals to the cameras, and also provides gating signals to the video combiner circuit. In the video combiner the video signals from each camera are amplified, processed, and applied as a composite video signal to the transmitter.

The two transmitters employed were designed to operate in the frequency band 960.05 ± 1 megacycle. The nominal center frequency of the F-channel transmitter is 959.52 mc, and that of the P-channel transmitter is 960.58 mc. The transmission spectrum is shown in Figure 8. The two transmitters are identical except for center frequency. The composite video signal that is applied to the transmitter has a 187-kc baseband. The output of the transmitter is a 60-watt frequency-modulated signal. The two 60-watt power amplifier outputs are combined in a four-port hybrid ring to provide two outputs with 30 decibels of isolation. One output is dissipated in a dummy load; the other signal is applied to the 4-foot-diameter high-gain antenna and transmitted to earth.

GROUND EQUIPMENT

The spacecraft-transmitted r-f signal is received by the 85-foot parabolic antenna at the Ranger ground station located at the Deep Space Instrumentation Facility (DSIF), at Goldstone, California. The antenna receiver system, using a maser pre-amplifier, converts the 960.05 mc f-m signal to a 30-mc, dual-channel signal and feeds it to the operational support equipment (OSE) through a 30-mc preamplifier for processing, recording, and display. A picture of the OSE is

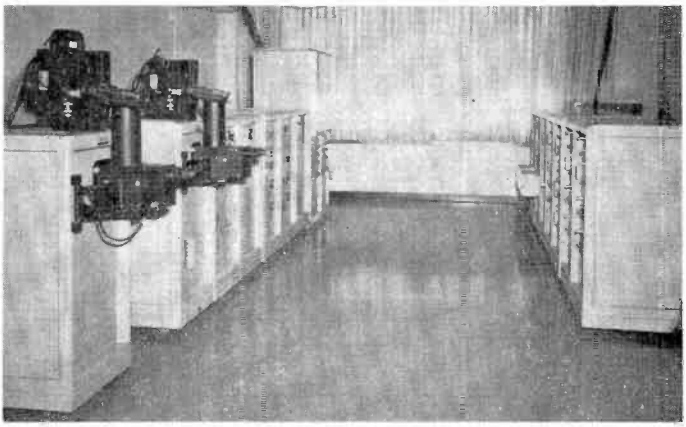

Fig. 9—Operational support equipment at the ground station in Goldstone, California.

shown in Figure 9. A simplified block diagram of the OSE is shown in Figure 10. The signal is again frequency-converted to the 5-mc region in the dual-channel limiter amplifier of the OSE receiver, and separated into two individual video channels for further processing. The channel containing the full-scan video signal is centered at 4.47 mc, and the channel containing the partial-scan video signal at 5.53 mc. These 4.47- and 5.53-mc signals are then applied to detector amplifiers, and "record i-f" amplifiers.

In the detector amplifiers, the signals are amplified, limited, detected, and de-emphasized, and then applied through a low-pass filter to the television recording and display equipment for on-line, or real-time, display and 35-mm film recording of the video. The outputs of the detector amplifiers are also applied to a 225-kc discriminator that rejects all video information from the signal and allows real-time display of the television-system telemetry data through a d-c coupled amplifier, on a strip-chart recorder.

The signals applied to each record i-f amplifier from the limiter

amplifiers are frequency converted to the 0.5-mc region and made available to the television recording and display equipment for the predetection tape recording of the composite video and 225-kc telemetry data.

Television recording and display equipment provides interim storage of predetected i-f data, and reduction, display, and archival storage

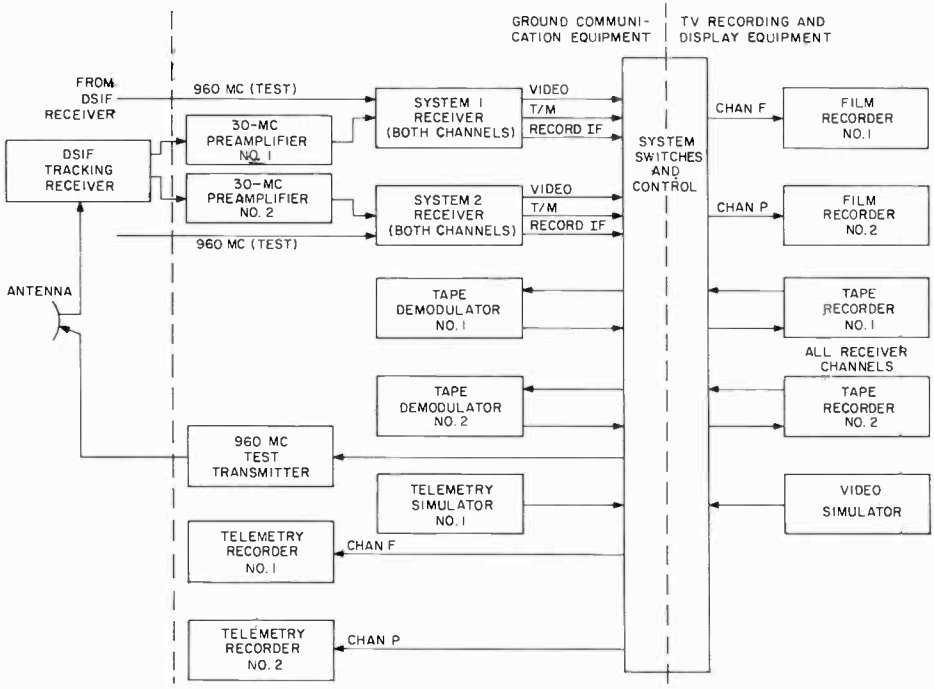

Fig. 10—Goldstone ground receiving equipment (simplified).

of the transmitted video information. Archival storage of the video data is performed automatically by 35-mm film recorders that provide photographic records of the kinescope displays of the F- and P-channel video. In addition, photographs of selected video displays are taken semi-automatically.

In the film-recorder equipment, kinescopes that utilize 5-inch cathode ray tubes (CRT) display a full frame of F_a or F_b video (Channel F), or four frames of camera P1, P2, P3, P4 video (Channel P). The kinescope for P-channel presentation displays the video frames of channel P in sequence and divided equally in area and aspect ratio in the four quadrants of the tube. A 35-mm camera then photographs

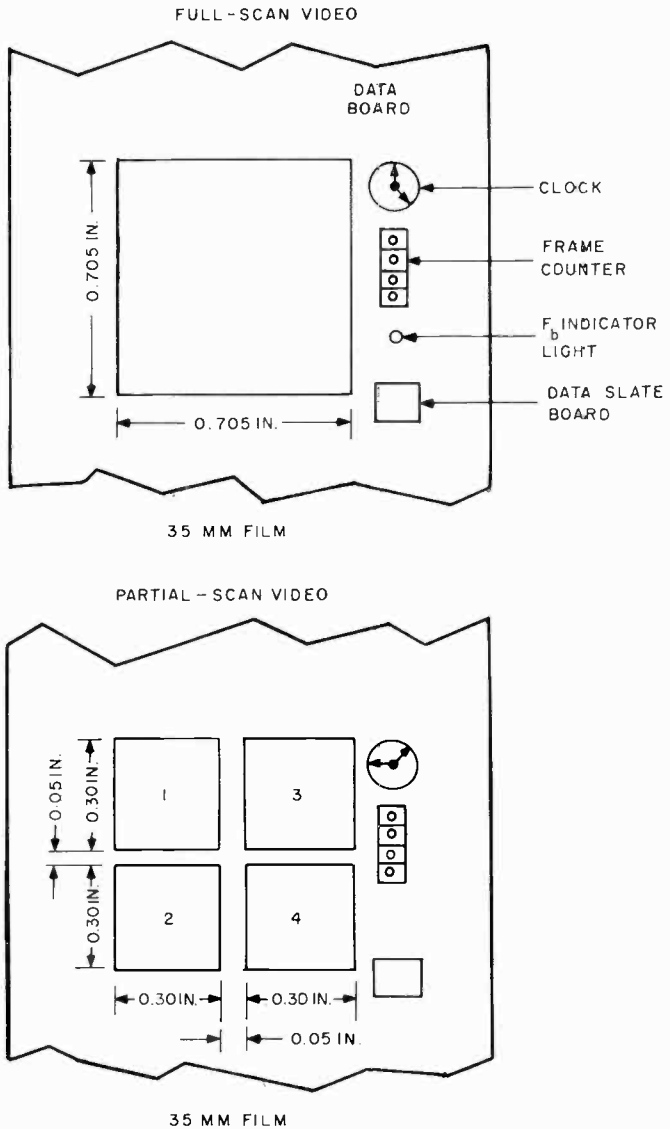

Fig. 11—Film recording format.

the tube face and a data board, which identifies the video display through use of a real-time clock, an indicator light to identify a F_b-camera display, a frame counter, and a slate board for handwritten information. Additionally, a Polaroid camera is used for single-frame, sampling photographs. The film-recording formats are illustrated in Figure 11.

The tape recording-equipment employed for predetection recording of the composite video and 225-kc telemetry signals are seven-channel, wide-band, magnetic-tape devices. The recorders operate at a tape speed of 120 inches per second, and an interconnection technique is used whereby each recorder records both full- and partial-scan video.

Additional redundancy is provided through the use of two completely separate ground stations including antennas, receiving, processing, and display equipment at the JPL Goldstone, California Deep Space Instrumentation Facility. These operational-support chains operate simultaneously during the terminal mode of the mission.

Extensive tests and calibrations of the television recording and display equipment are performed using electrically generated test standards to assure that picture detail and photometric characteristics are faithfully reproduced. Magnetic tape recordings of actual video data from various spacecraft tests are used to confirm the operating parameters of the video display equipment and the film recorders. Resolution capabilities, linearity, cathode-ray-tube display characteristics (optical distortion, sizing, etc.), and the integrity of the display are checked. Further test and calibration of the entire operational support equipment are carried out up to the time of the terminal-mode operation of the spacecraft when the video signals from the spacecraft are transmitted. Additionally, post-flight calibration and check are performed so that proper evaluation of the received data can be made, based on the actual performance of the operational support equipment during the mission.

Performance of the Ranger Television System

Ranger VII

Ranger VII was launched from Cape Kennedy, Florida at 16.50 GMT on July 28, 1964. At approximately 13.06 on July 31, the F channel was placed in warmup by a command from the television system clock. The F channel went into full power operation 80 seconds later and began taking pictures. The P channel was placed in warmup at approximately 13.09 and was placed in full-power operation 80 seconds later by a command stored in the spacecraft. Picture-taking continued for approximately 17 minutes until impact in the Mare Nubium just south-west of the crater Guericke at 13.25.50 GMT. The target area, a lunar maria, appeared from earth to represent an area typical of the smoothest parts of the lunar surface. The topological features of the lunar maria as viewed from earth presented the type of surface considered to be desirable for the "soft" landing of manned

spacecraft. The actual impact area at 10.6° South and 20.6° West was outside of the zone of preferred manned landing areas of plus or minus 5 degrees of the lunar equator, but was in an area that was considered to be representative of the large, relatively smooth mare to be explored. Because the lighting conditions of the moon could not be precisely determined from earth, the gains of the F_b, P1 and P2 cameras were adjusted for a peak scene luminance of 2700 foot Lamberts and the gains of the F_a, P3 and P4 cameras were adjusted for a peak scene luminance of 650 foot Lamberts. Analysis of the video data obtained indicated that the choice of impact area for the Ranger VII spacecraft resulted in maximum use of the optical-to-video conversion capabilities of all six cameras. A total of 4308 pictures of the lunar surface were taken, transmitted, and successfully recovered on earth. The pictures have been published in atlas form,* and distributed on a world-wide basis.

The Ranger VII spacecraft and television system met or surpassed all mission goals and objectives. The level of performance of some portions of the system can be evaluated on the basis of specific information received during the mission. This is particularly true in regard to the cameras and their associated electronic equipment, since the pictures themselves are evidence of the performance of this equipment. It is also true, although to a lesser degree, of the telecommunications and OSE equipment. The performance of the command and control circuitry, however, can only be evaluated in absolute terms; that is, all commands were processed and executed on-time and in good order.

The last partial-scan picture, shown in Figure 16, was a fragment from the P3 camera, which was equipped with a 25-mm, f/0,95 lens. A simple geometrical relationship for the 25-mm optical system and for a spacecraft traveling at 2.64 km/sec shows that the final picture was taken at an altitude of 530 meters above the point of impact on the lunar surface and covered an area of about 42 meters by 28 meters. Craters can be recognized that occupy 1/50 of picture height, a diameter of 0.8 meter. The bright rim and shadowed rim constitute image elements of 0.4 meter; hence, the high-resolution goal was attained.

The requirements of wide-angle coverage and picture nesting were imposed as a basis for correlation of the expected data output from the Ranger camera with the well-defined telescopic photographs presently available. The success with which Ranger VII met these objectives is illustrated by Figure 12. This image was produced by the F_a-Camera,

* Ranger VII Photographs of the Moon: Part 1, Camera A Series, NASA SP-61 (Sept. 1964); Part 2, Camera B series, NASA SP-62 (Feb. 1965); and Part 3, Camera P Series (to be released).

which has a 25-degree field of view, and was taken 480 miles before impact. It covers a wide area where several well known features, such as the crater Lubiniezky and the Riphaeus mountains, can be distinguished by their characteristic images and their geographical rela-

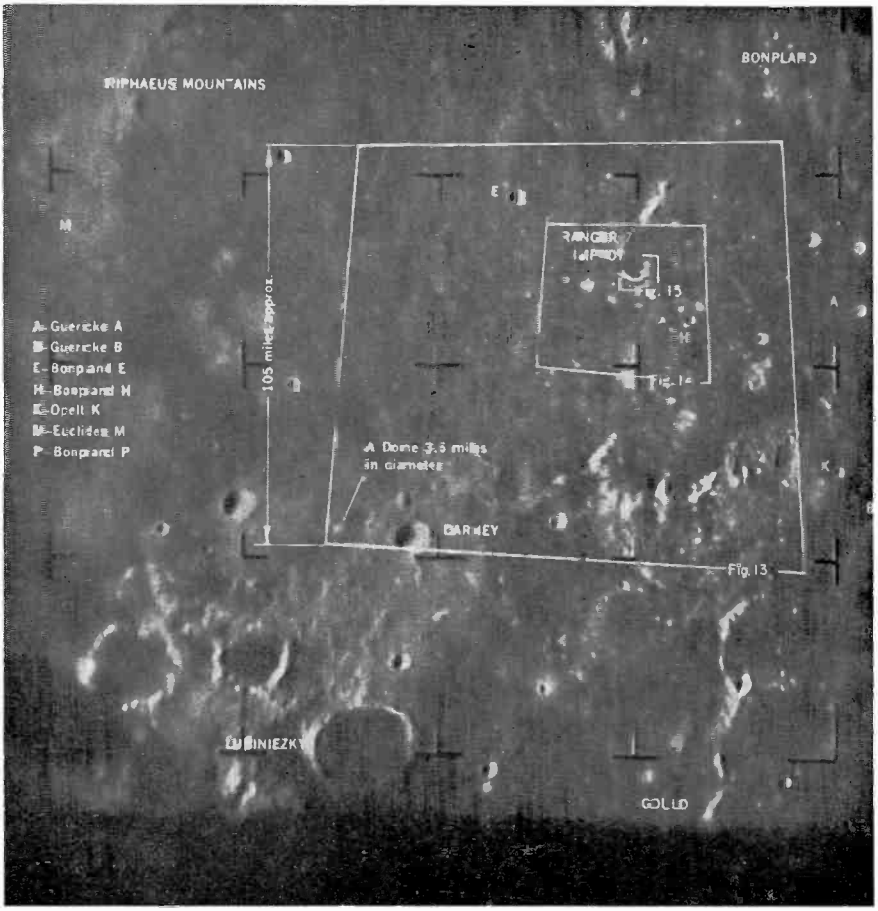

Fig. 12—Picture taken by Ranger VII F_a camera of northwest Mare Nubium showing picture nesting (taken at an altitude of 480 miles).

tionships. Also indicated on this figure are the areas covered by pictures taken later in the picture-taking sequence at a higher level of resolution, including the point of impact as shown in Figures 13, 14 and 15. The realization of the design to satisfy picture nesting is contained in the interplay of camera fields of view, the camera mounting bracket that physically ties the six-camera array into appropriate

overlapping fields of view, the camera exposure sequence, and the design of the impacting trajectory.

Review of the received video data indicated that the choice of lunar impact area resulted in maximum use of the optical-to-video conversion

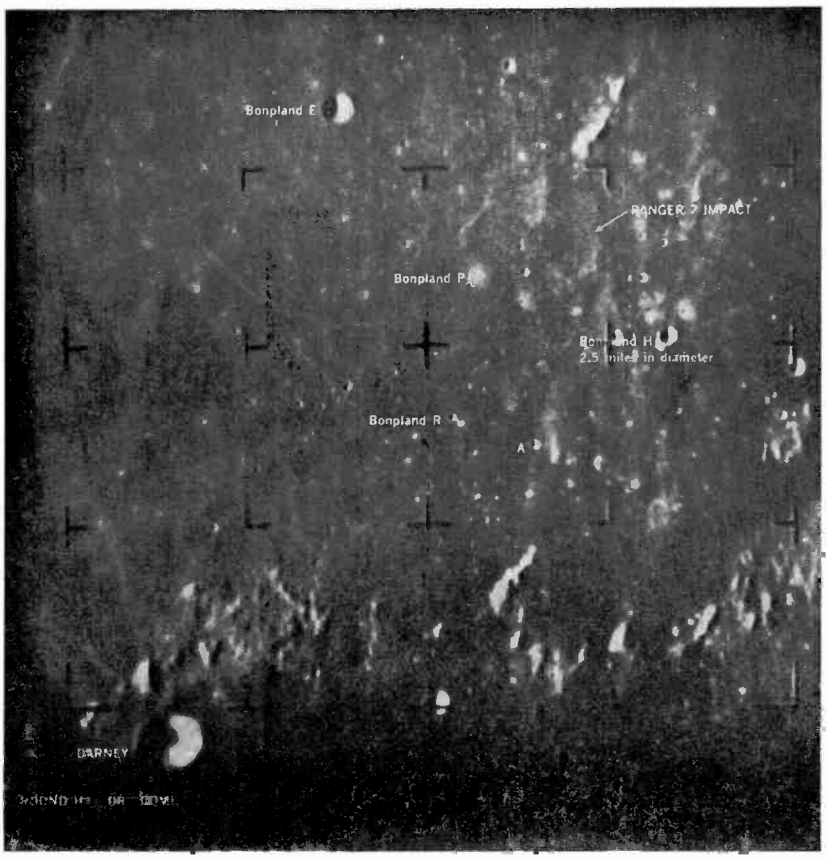

Fig. 13—F_a camera picture taken at 235 miles altitude, 2 minutes 40 seconds before impact.

capabilities of all six cameras. The video data indicated that on the three 25-mm, f/0.95 cameras the peak illuminations were occasionally near the saturation level of the cameras, but the cameras did not actually saturate nor was the signal clipped. Maximum exposure without saturation was then achieved on the F_a, P3, and P4 cameras. The F_b, P1, and P2 cameras had average exposures with signal-to-noise ratios that were 3 to 4 decibels lower than for the F_a, P3, and P4 cameras.

Video-line selections from the final F_a and P3 camera frames show

that the requirement of high signal-to-noise ratio was also satisfied. A received video signal with a signal-to-noise ratio in excess of 30 db (peak-to-peak signal to r-m-s noise) will produce a picture acceptable as having high quality. The average signal-to-noise ratio was 35

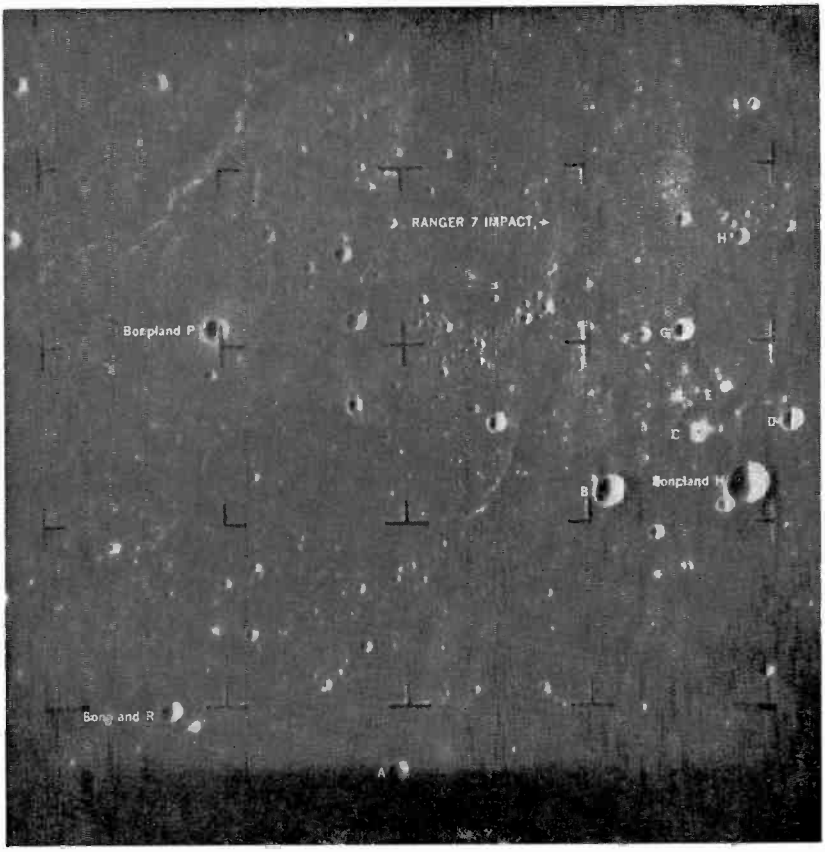

Fig. 14—F_a camera picture taken at 85 miles altitude, last of previously known craters.

decibels for the F_a, P3, and P4 cameras, and 31 decibels for the F_b, P1, and P2 cameras. Each of the six cameras, then, provided a video signal with more-than-adequate signal-to-noise ratios to satisfy that specification and the video criterion for high-quality images.

Ranger VIII

The selected Ranger VII impact area, a region of lunar maria located between Oceanus Procellarum and Mare Nubium was classified

by astronomers as a "red" mare. The success of Ranger VII in classifying the small-scale topography of this typical "red" mare raised questions with respect to its similarity with other maria. The February launch period chosen for Ranger VIII permitted the selection

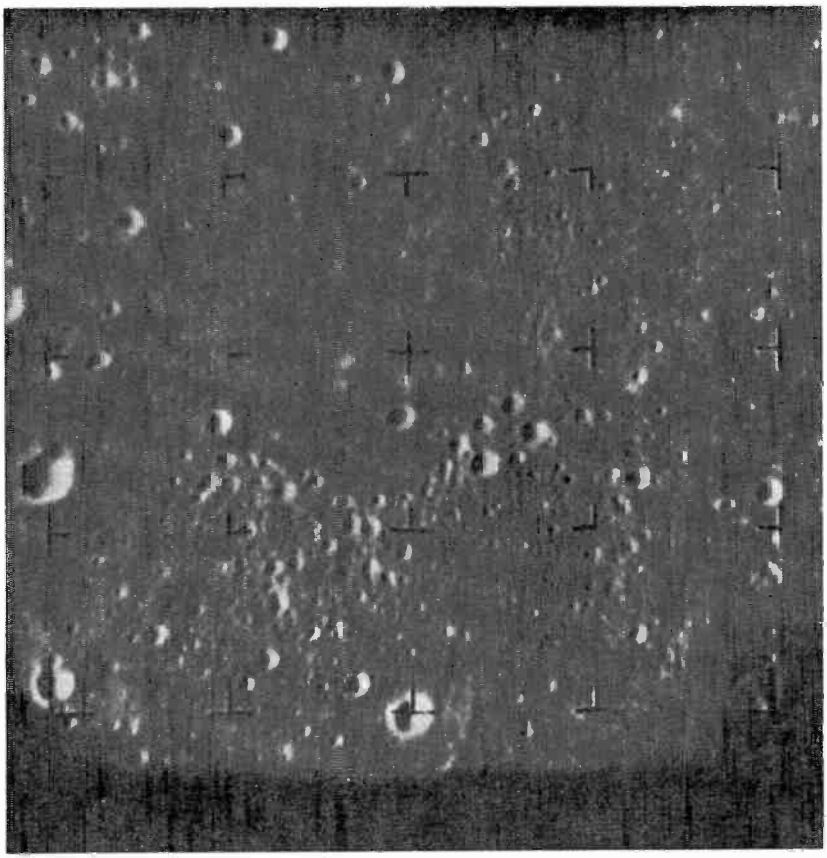

Fig. 15—F_a camera picture taken at an altitude of 34 miles showing "rays" of crater Copernicus.

of a "blue" mare, Mare Tranquillitatis, as the target impact area. In addition, this launch period permitted the selection of a target area within the Apollo landing zone, thus providing photographs of a potential landing site.

The Ranger VIII spacecraft impacted on the lunar surface at 09.57.36 GMT on February 20, 1965. The spacecraft obtained 7140 pictures of the moon that covered an area extending from Mare Nubium, across the lunar highlands, to Mare Tranquillitatis. The final

pictures were taken in Mare Tranquillitatis before Ranger VIII impacted at lunar co-ordinates 2.6° North and 24.8° East.

Based on an increased ability to define the anticipated levels of lunar luminance as a result of information gained from camera performance of the Ranger VII mission, the gains of the P1, P2 and F_b

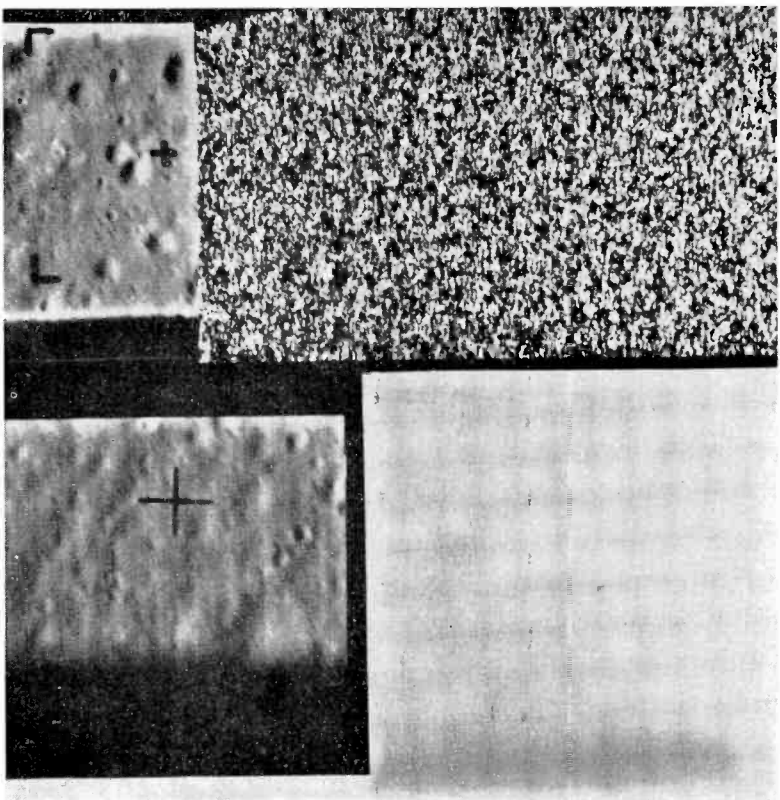

Fig. 16—Final P1 and P3 camera frames taken by Ranger VII.

cameras on Ranger VIII were adjusted for a peak scene luminance of 1600 foot lamberts; the P3, P4 and F_a cameras remained at a saturation level of 650 foot lamberts.

The picture-taking sequence was initiated when the spacecraft was still 1550 miles from the surface of the moon, and all six television cameras continued to transmit pictures for 23 minutes until the spacecraft impacted at almost 6000 miles per hour. The initial pictures transmitted covered an area about 400 miles long and 200 miles wide.

The Ranger spacecraft was designed to provide attitude orientation

through a terminal maneuver to minimize the effects of uncompensated image motion in the final pictures. The close alignment of the camera axis and velocity vector in the Ranger VII flight did not require the performance of a terminal maneuver; however, the Ranger VIII trajectory required a terminal maneuver if the maximum resolution capability of the system was to be realized. Analysis of the flight path of the Ranger VIII spacecraft indicated, however, that without a terminal maneuver, a wide swath of overlapping coverage of the lunar highlands and maria would be obtained, providing stereo coverage of the areas photographed. The stereo photographs were deemed to be of more interest than the final high resolution pictures and a terminal maneuver was not performed.

The pictures provided by Ranger VIII showed a great degree of similarity in topography between the "red" mare photographed by Ranger VII and the "blue" Mare Tranquillitatis. The stereo photographs obtained permit a far more accurate height determination for the areas photographed than was previously possible.

Ranger IX

The success of Rangers VII and VIII in photographing the lunar maria and the similarity of the data obtained in these two missions, enabled the use of Ranger IX to photograph a lunar crater region. The crater Alphonsus was selected as the primary target for this launch because of the numerous dark haloed craters and elaborate system of rills on the floor of Alphonsus. The specific selection of a target on the floor of Alphonsus represented a compromise between the central peak where the Russian astronomer Kosyrev obtained a spectrogram of an apparent gaseous discharge and the rills and dark haloed craters along the eastern wall of Alphonsus.

Ranger IX impacted on the moon at 14.08.20 GMT on March 24, 1965. The impact occurred at lunar coordinates 12.9° south and 2.4° west, near the eastern wall of Alphonsus. Ranger IX returned 5814 pictures with excellent contrast and high shadowing. The spacecraft terminal maneuver discussed in connection with Ranger VIII was performed by Ranger IX and the resolutions obtained in these pictures were the best of the three successful Ranger missions. Figure 17 is a picture transmitted 19 minutes before impact at an altitude of 1485 miles. Figures 18 through 21 correspond approximately to the successively smaller areas outlined in black in Figure 17. Figure 22 shows the last three frames transmitted by the P1 camera. The smallest crater visible is 2½ feet across and features as small as 12 inches across are visible.

During the 18-minute picture-taking period before impact, the two full-scan and four partial-scan cameras of the Ranger IX television system continuously obtained pictures of the lunar surface. The first

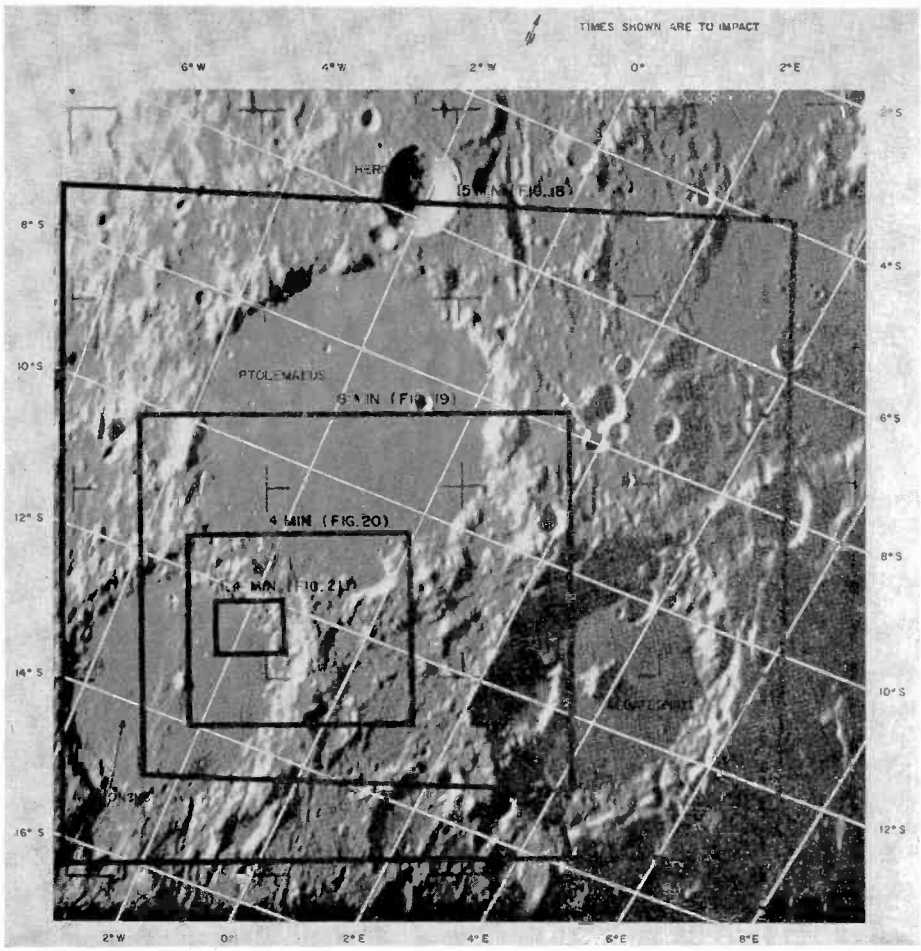

Fig. 17—Photograph taken by Ranger IX F_b camera 19 minutes prior to impact at an altitude of 1485 miles. Nesting pattern corresponds to Figures 18 through 21.

full-scan picture was taken at an altitude of 1500 miles and the last partial-scan picture was transmitted between 0.2 and 0.05 second before impact. The flight of Ranger IX was a "textbook" mission, in which all systems performed normally and from which sharp-detailed video data of the area about and within the 75 mile-diameter crater Alphonsus were obtained.

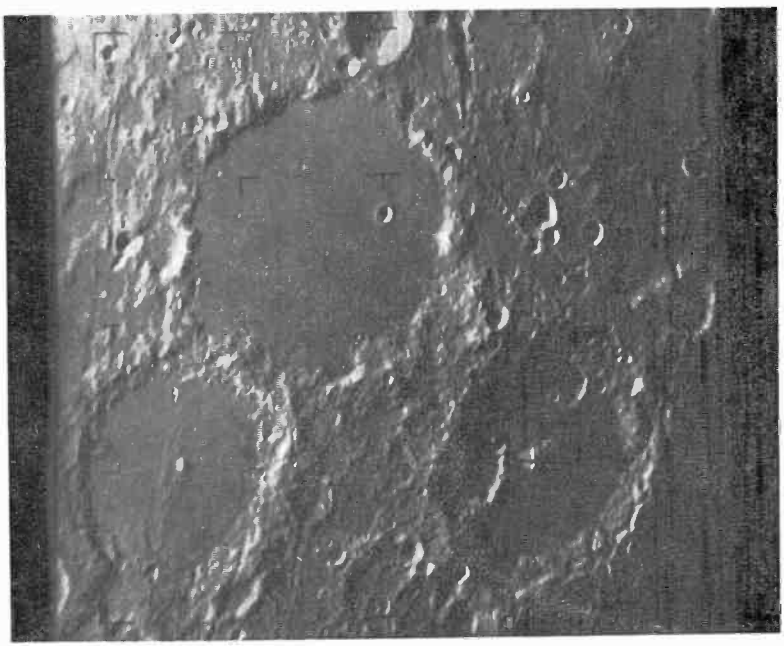

Fig. 18—Photograph taken by Ranger IX F_b camera 15 minutes before impact (altitude 1208 miles).

Fig. 19—Photograph taken by Ranger IX F_b camera 8 minutes before impact (altitude 683 miles).

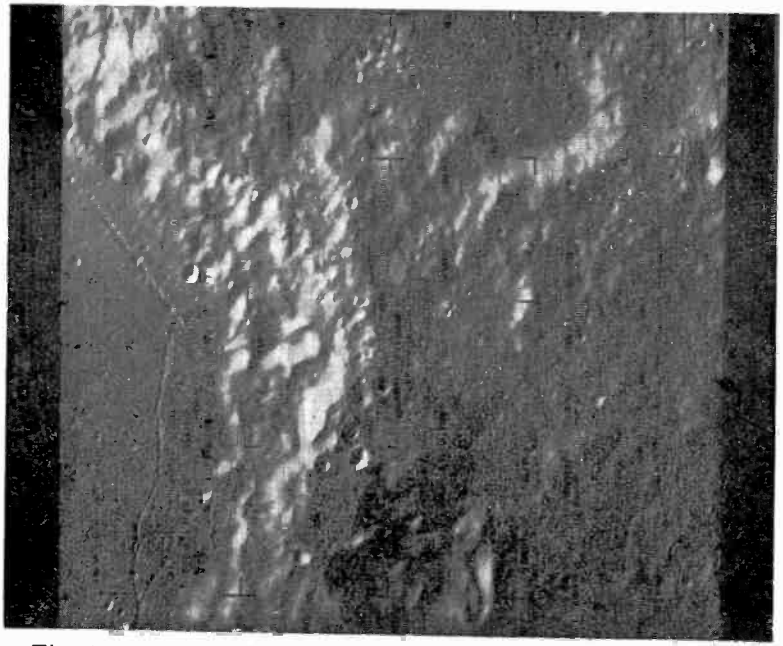

Fig. 20—Photograph taken by Ranger IX F_b camera 4 minutes before impact (altitude 349 miles).

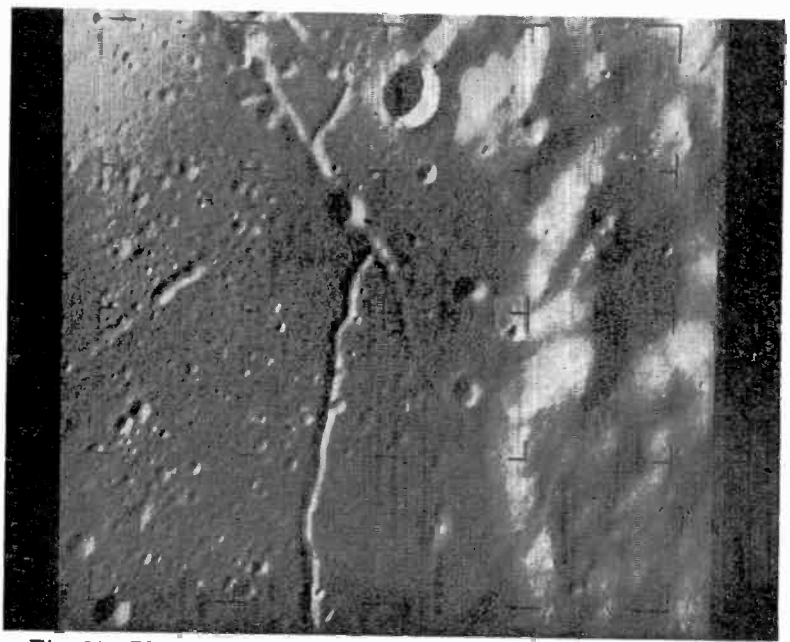

Fig. 21—Photograph taken by Ranger IX F_t camera 1.4 minutes before impact (altitude 130 miles).

CONCLUSIONS

The Ranger program fulfilled its mission objectives of obtaining both wide area coverage and high resolution photographs of the lunar surface. The television system met or surpassed all design objectives in the flight of Rangers VII, VIII, and IX. More than 17,000 high

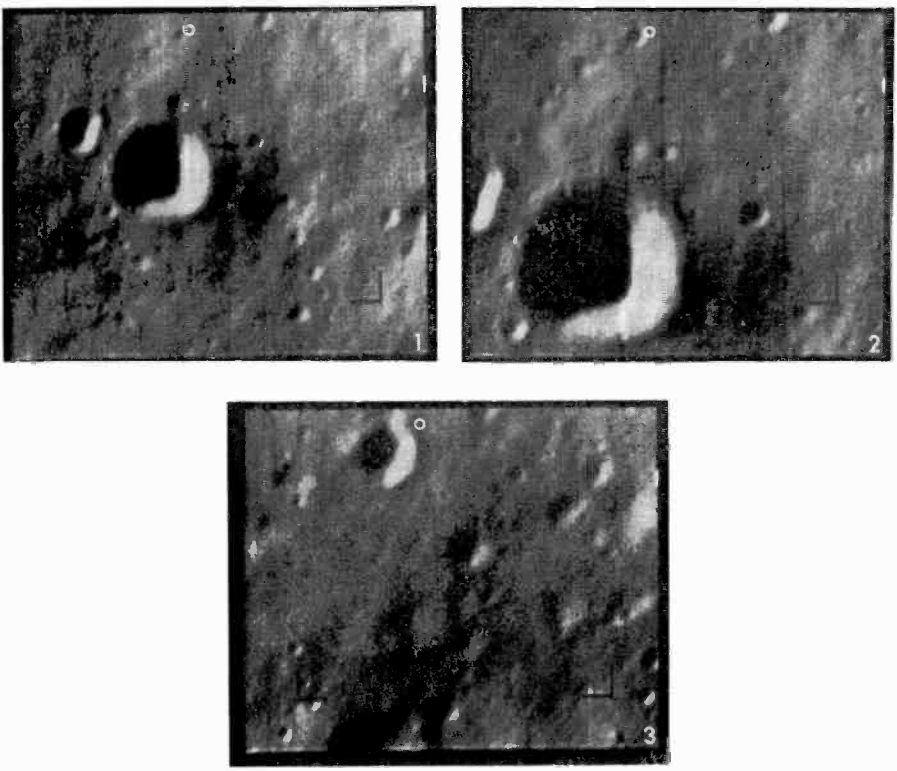

Fig. 22—Last three camera frames from Ranger IX P1 camera. The lower photograph (3) is the last in the sequence. Ranger IX impacted in the circled area near upper margin. The smallest visible crater is 2½ feet across.

quality photographs of three widely separated regions of the lunar surface were obtained. Although the photographs cannot provide direct information on the surface hardness, they do indicate that the detailed topological features do not preclude a "soft" landing by a manned spacecraft. The photographs indicate that craters are dominant features of the lunar topology down to the limit of the resolution achieved, and it may reasonably be extrapolated that even smaller craters exist down to a size where the grain size of the lunar surface material equals the crater size.

RCA Technical Papers†

Second Quarter, 1965

Any request for copies of papers listed herein should be addressed to the publication to which credited.

"Calculations of Speed of Ladder Network for Superconductive Associative Memories," R. W. Ahrons, *Trans. IEEE PTGEC* (Short Notes) (April) 1965

"Chebyshev Approximation and Threshold Functions," K. R. Kaplan and R. O. Winder, *Trans. IEEE PTGEC* (Short Notes) (April) 1965

"Communications: A Challenge to Leadership," D. Sarnoff, *Signal* (April) 1965

"The Effects of Oxide Traps on the MOS Capacitance," F. P. Heiman and Coauthor, *Trans. IEEE PTGED* (April) 1965

"Limitations of the MOS Capacitance Method for the Determination of Semiconductor Surface Properties," K. H. Zaininger and Coauthor, *Trans. IEEE PTGED* (April) 1965

"On the Mechanism of Amplification in Superconducting Films," A. S. Clorfeine, *Proc. IEEE* (Correspondence) (April) 1965

"Metal-Semiconductor Barrier Height Measurement by the Differential Capacitance Method Without an Ohmic Reference Contact—One-Carrier System," A. M. Goodman, *Jour. Appl. Phys.* (April) 1965

"Multiple-Diode Theorems," R. L. Ernst, *Proc. IEEE* (Correspondence) (April) 1965

"The Probable Reliability of a Measurement," W. D. Moon, *Electronic Industries* (April) 1965

"Properties of Threshold Functions," R. O. Winder, *Trans. IEEE PTGEC* (Short Notes) (April) 1965

"The Spiral Top-Loaded Antenna," B. E. Keiser, *Proc. IEEE* (Correspondence) (April) 1965

"Suction versus Pressure Forced Air Cooling," G. Rezek, *Trans. IEEE PTGPEP* (April) 1965

"Supersonic Domain Wall Motion in Triglycine Sulfate," B. Binggeli and E. Fatuzzo, *Jour. Appl. Phys.* (April) 1965

"Temperature Evaluation in Microelectronic Structures Using Analog Networks," G. Rezek, *Trans. IEEE PTGPEP* (April) 1965

"Using a Decision-Table Structure as the Input Language Format for Programming Automatic Test Equipment Systems," B. Scheff, *Trans. IEEE PTGEC* (Short Notes) (April) 1965

"Microwave Phonon-Assisted Tunneling in Superconducting Diodes," B. Abeles and Y. Goldstein, *Phys. Rev. Letters* (12 April) .. 1965

"Klystron Life-Span," G. K. Hahn, Jr., *Electronics* (Readers Comment) (April 19) 1965

"Dynamics of Oxidation-Reduction Processes in Rare-Earth-Doped CaF_2," Z. J. Kiss and D. L. Staebler, *Phys. Rev. Letters* (26 April) 1965

† Report all corrections to *RCA Review*, RCA Laboratories, Princeton, New Jersey, 08540.

"Analysis of GaAs Tunnel Diode Oscillators," F. Sterzer, *Trans. IEEE PTGED* (May) 1965
"Beam Noise Reduction in High Magnetic Fields," B. Vural, *Proc. I.E.E.E.* (Correspondence) (May) 1965
"Comments on 'Excess Current in Gallium-Arsenide Tunnel Diodes'," R. D. Gold, *Proc. I.E.E.E.* (Correspondence) (May) 1965
"Effects of γ Irradiation on the Divalent Holmium Concentration in CaF_2," E. S. Sabisky, *Jour. Appl. Phys.* (Communications) (May) 1965
"Electronic Heat Controls for Appliances and Domestic Heating," G. D. Hanchett, *Trans. IEEE PTGIGA* (May/June) 1965
"Formation of Dislocations Around Precipitates in Single Crystals of (Zn,Cd)S:Er," M. S. Abrahams and A. Dreeben, *Jour. Appl. Phys.* (May) 1965
"Long-Wire Antennas," E. A. Laport, *Electronic Industries* (May) 1965
"Microwave Impedance of Semiconductor Posts in Waveguides. Part I," R. D. Larrabee, *Jour. Appl. Phys.* (May) 1965
"Optical Beam Deflection by Pulsed Temperature Gradients in Bulk GaAs," S. G. Liu and W. L. Walters, *Proc. I.E.E.E.* (Correspondence) (May) 1965
"Threshold Dependency on Reabsorption Loss in Injection Lasers," M. F. Lamorte, H. Junker, and T. Gonda, *IEEE Jour. Quantum Electronics* (Correspondence) (May) 1965
"A Two-Position Probe Method of Microwave Impedance Measurements for the Determination of the Electrical Properties of Indium Antimonide. Part II," R. D. Larrabee, D. W. Woodard, and W. A. Hicinbothem, Jr., *Jour. Appl. Phys.* (May) 1965
"Retrieving Data from Gemini," R. G. Erdmann, *Electronics* (May 3) 1965
"Blurred Color," C. J. Hirsch, *Electronics* (Readers Comment) (May 17) 1965
"Effect of Traps on Acoustoelectric Current Saturation in CdS," A. R. Moore and R. W. Smith, *Phys. Rev.* (17 May) 1965
"Electron and Phonon Scattering in GaAs at High Temperatures," A. Amith, I. Kudman, and E. F. Steigmeier, *Phys. Rev.* (17 May) 1965
"Television's Toughest Challenge," M. H. Mesner, *Electronics* (May 17) 1965
"Tunneling in Lead Salt p-n Junctions," R. M. Williams and Coauthor, *Phys. Rev. Letters* (17 May) 1965
"Computing Irredundant Normal Forms from Abbreviated Presence Functions," D. M. Y. Chang and Coauthor, *Trans. IEEE PTGEC* (June) 1965
"Design of Solid-State Radar Transmitter Units for the Lunar Excursion Module," E. Bliss and M. Fromer, *Trans. IEEE PTGPMP* (June) 1965
"Enumeration of Seven-Argument Threshold Functions," R. O. Winder, *Trans. IEEE PTGEC* (June) 1965
"Fixed Resistor-Card Memory," M. H. Lewin, H. R. Beelitz, and J. Guarracini, *Trans. IEEE PTGEC* (June) 1965
"Generalized Functions and Laplace-Transform Initial Conditions," R. B. Schilling and P. Schnitzler, *Proc. IEEE* (Correspondence) (June) 1965
"Generation of Microwave Power by Parametric Frequency Multiplication in a Single Transistor," M. Caulton, H. Sobol, and R. L. Ernst, *RCA Review* (June) 1965
"Grid-Controlled Power Tubes in Particle-Accelerator Applications," M. V. Hoover, *Trans. IEEE PTGNS* (June) 1965
"Linear Signal Stretching in a Time-Variant System," H. Weinstein, *Trans. IEEE PTGCT* (June) 1965
"Low-Energy-Electron Scattering from Photoconductors Applied to a Camera Tube," A. D. Cope and W. Bruce, *RCA Review* (June) 1965
"Multiple-Input Large-Signal Mixer Analysis," P. Torrione and S. Yuan, *RCA Review* (June) 1965

AUTHORS

N. K. CHITRE received the B.Sc. and M.Sc. degrees in Physics from the Banaras Hindu University in 1953 and 1955, respectively, and the M. Tech. degree in Electronics from the Indian Institute of Technology, Kharagpur, in 1956. After a year with Van der Heem, N.V. The Hague, he studied at the Imperial College, London, where he received his diploma (D.I.C.) and, in 1962, the Ph.D. degree of the University of London. In March 1963, Dr. Chitre joined the RCA Victor Co. Ltd., Montreal, where he has worked on microwave communications systems, both overland and satellite, and designed various microwave multiplexing networks, filters, and ferrite components. Dr. Chitre is a Member of the I.E.E.

R. FERYSZKA received the masters degree in Electrical Engineering from the Polytechnic of Lwow, Poland in 1936. From 1936 to 1939 he was employed as a design engineer on radio receivers at Elektrit, Wilno, Poland. From 1949 to 1956 Mr. Feryszka was manager of Design Engineering and later assistant to the Chief Engineer at "KASPRZAK" Electronic Plant in Warsaw. In 1956 he transferred to the Tele Radio Institute in Warsaw, where he carried out environmental investigations on electronic components. In 1960 Mr. Feryszka joined RCA Electronic Components and Devices as an applications engineer on the micromodule program. In 1963 he joined the advanced development group at Somerville, where he was responsible for the development of high-power tunnel-diode inverters. He is presently working on the development of UHF MOS transistors for television applications. Mr. Feryszka is a member of the Institute of Electrical and Electronics Engineers.

PETER FOLDES received the B.S. degree in electrical engineering from the Technical University of Budapest in Budapest in 1950. From 1950 to 1956 he was a research engineer at the Hungarian Telecommunication Research Institute and from 1953 to 1956, on a part-time basis, was also a lecturer on antennas at the Technical University of Budapest. In 1957 he joined RCA Victor Co., Ltd., Montreal, Canada. He has worked mostly in the field of antenna, propagation, and system engineering studies. Since 1958 he has been responsible for the theoretical aspects of the microwave subsystem in a wide-band microwave communication system. Mr. Foldes is a member of the American Institute of Electrical Engineers.

P. GARDNER received the diploma in Technology in Applied Physics from Brunel College of Technology in London, England, in 1960. From 1960 to 1961 he worked at Transitron Electronic Corporation. Mr. Gardner joined the RCA Semiconductor and Materials Division in 1961. There, he has worked on high-speed germanium tunnel diodes and microcurrent and high-current germanium tunnel diodes. In 1963, he joined the Advanced Devices Development Activity where he has been engaged in the development of high-current Ge and GaAs tunnel diodes and MOS transistors.

STEVEN G. KOMLOS received the B.S. degree in electronics engineering from the Technical University of Budapest in 1952. From 1952 to 1956 he worked as a lecturer at the Technical University of Budapest, and from 1954 to 1956 he was also consulting engineer for the Hungarian Television Co. In 1957, he joined RCA Victor Company, Ltd., Montreal, where he carried out development work in TV Broadcasting. At present, he is engaged in antenna development work.

EDGAR W. MARKARD received the BEE Degree from City College of New York in June 1961. He joined RCA and after a short training period was assigned to the advanced microwave techniques group of RCA Communications System Division, New York, where he worked on S band, broadband parametric amplifiers. At the completion of that program, he worked on the development of varactor frequency multipliers, and was responsible for the development of a high-power microwave varactor multiplier chain which yielded two watts at C-band. Hhe was then assigned to the cryoelectric program which has as its objective the development of a parametric amplifier based on the superconducting properties of thin films. He is also working on high power tunable and broadband varactor frequency multipliers, and has participated in the development of the theory of high nonlinearity (hyper-abrupt) varactor devices.

Mr. Markard is a member of the Institute of Electrical and Electronics Engineers, Eta Kappa Nu, and the American Institute of Aeronautics and Astronautics.

BERNARD P. MILLER received a B.S. in Aeronautical Engineering from Pennsylvania State University in 1950, and did post-graduate work, also in Aeronautical Engineering, at the U.S. Air Force Institute of Technology in 1953 and 1954 and at Princeton University from 1957 to 1959. From 1950 to 1953, as a captain in the USAF, he was assigned to the Aircraft Laboratory, Wright Air Development Division. In 1954, he taught at the U.S. Naval Academy, Annapolis, as an instructor of Fluid Dynamics and Thermodynamics. In 1956 he was appointed Head of the Thermodynamics group of the Academy's Department of Marine Engineering. He joined the RCA Special Systems and Development Department in Princeton in 1957, and transferred to the Astro-Electronics Division in 1958. There, on Project JANUS, he performed trajectory and orbital analyses and ascertained propulsion-system requirements. From 1959 through 1961, he was Project Engineer on a series of studies examining military applications of space systems. In 1961, Mr. Miller participated in the series of studies that eventually led to the present RCA Ranger Project. With the organization of the RCA Ranger Project, he was appointed Group Leader, Mechanical Systems, and in 1963 was made Ranger Project Manager. Mr. Miller received a NASA Public Service Award in October 1964 for work on the six-camera television system used aboard Ranger 7. Mr. Miller is a member of the Institute of Aerospace Sciences and is a registered Professional Aeronautical Engineer.

JOHN A. OLMSTEAD received the B.S. degree in electrical engineering from the University of Buffalo in 1952 and the M.S. degree in electrical engineering in 1957 from Newark College of Engineering. He has also taken graduate courses in mathematics and physics at the University of Buffalo. In 1952 he joined the Radio Corporation of America as a specialized trainee. From 1952 to 1954 he worked on gaseous discharge devices at RCA Laboratories, Princeton. In 1954 he joined Electronic Components and Devices, Harrison, N. J., where he worked on the design and development of gas-filled and other specialized industrial tubes. Between 1950 and 1960 he alternated between assignments at RCA and the University of Buffalo where he was an Assistant Professor of Electrical Engineering. In 1960 he returned to RCA on a full time basis, joining the Semiconductor and Materials Division. He has worked on GaAs solar cells, p-n junction field-effect devices, high-frequency power bipolar transistors and MOS field-effect transistors. He is responsible for the multi-emitter concept basic to the "overlay" transistor technique. Mr. Olmstead is a member of the Institute of Electrical and Electronics Engineers and Sigma Xi.

R. SCHWERDTFEGER graduated from McGill University in 1963 with a B.E.E. Since this time he has been a member of the RCA Victor Company, Ltd., Montreal, working on the design and development of the multimode feed antenna to be used in Canada's first satellite communication station.

JOSEPH H. SCOTT received the A.B. degree in chemistry from Lincoln University, Pennsylvania. In 1958 he attended graduate school at Howard University, Washington, D.C. and is presently pursuing a degree in Electrical Engineering at Newark College of Engineering. In 1959, he joined RCA, where he has been engaged in research and development of semiconductor devices. He has worked on GaAs solar cells, p-n junction unipolar transistors, high-frequency high-power bipolar transistors and, most recently, MOS transistors. Together with J. A. Olmstead he did the initial work on multi-emitter "overlay" transistors. Mr. Scott is a member of the Electrochemical Society.

T. SZIRTES received his Diploma of Mechanical Engineering at the Technical University of Budapest in 1950. In the same year he joined the Hungarian Research Institute for Development of Engines and Vehicles as a research engineer. In 1956 he emigrated to Canada where he became an instructor at McGill University, Montreal, in the Department of Mechanical Engineering. In 1960 he received his Master of Mechanical Engineering degree at McGill. In early 1961 he joined RCA Victor Company, Ltd., Montreal, as a mechanical engineer designing antennas, feed systems and mechanisms. He has also worked on problems of heat transfer, structures, and applied and celestial mechanics. He is a member of ASME.

S. YUAN (See *RCA Review*, Vol. XXVI, June, 1965, p. 319.)